

High resolution assessment of concentrations in the urban canopy layer

Dissertation

zur Erlangung des Doktorgrades der Naturwissenschaften
an der Fakultät für Mathematik, Informatik und Naturwissenschaften
Fachbereich Geowissenschaften
der Universität Hamburg

vorgelegt von
David Grawe
aus Hamburg, Deutschland

Hamburg, 2019

Als Dissertation angenommen am Fachbereich Geowissenschaften.

Tag des Vollzugs der Promotion: 05.07.2019

Gutachterin und Gutachter: Prof. Dr. K. Heinke Schlünzen
Prof. Dr. B. Leidl

Vorsitzender des
Fachpromotionsausschusses
Geowissenschaften: Prof. Dr. Dirk Gajewski

Dekan der Fakultät MIN: Prof. Dr. Heinrich Graener

Abstract

Urban air quality is currently a prominent topic in Germany and in other countries in Europe. A large fraction of urban areas suffer from air pollution at levels that are considered harmful for human health. Where persistent exceedances occur, local authorities need to collate local air quality action plans which may have wide ranging consequences, including closing selected streets for some very polluting vehicles. In order to justify such measures, the assessment of urban air quality has to be rigorous and properly evaluated. The EU legislation governing air quality in Germany has set-out requirements for the spatial representativeness of assessed pollutant concentrations.

Ambient concentrations of air pollutants regularly reach high levels in the urban canopy layer, particularly near main roads or at places with low ventilation. The urban canopy layer is characterised by very heterogeneous conditions. Emissions of pollutants can be very local and vary in time and space. Local building configurations and meteorological conditions determine the wind field which drives transport and dispersion of pollutants. Since the relevant parameters are very variable, the obtained concentrations can be similarly variable. To assess relevant impacts on human health, the concentrations need to be determined with good temporal and spatial representativeness. In complex conditions, point measurements have limited representativeness unless a high number of measurement points is available. The high resolution numerical model presented in this thesis can be used to determine the representativeness of urban monitoring stations or to provide concentration levels in complex conditions.

This thesis contributes to the quality assurance for urban air quality assess-

ment. It presents components of a complex set of models that can be used to support the assessment of urban air quality. These components are compared with data measured in a physical wind tunnel model based on an state-of-the-art technique. The evaluation of the model results demonstrates how a high-resolution model for concentrations in the urban canopy layer can be tested. The further analysis determines how representative urban measurement sites can be found using a realistic example. In a sensitivity study the influence of processes governing the level of ambient concentrations is quantified.

In the atmosphere, pollutants continue to react and change the atmospheric composition on various time scales, in some cases also forming new secondary pollutants. To represent this, the numerical model needs to solve alongside the meteorological equations also a set of equations for chemical reactions. Such reaction mechanisms exist and a mechanism developed originally for mesoscale applications has been used here.

The evaluation of model results shows a very good agreement of the wind field model with comparison data following a German guideline for the evaluation of wind field models. For the evaluation of pollutant concentrations, model results have been compared with wind tunnel data and with field measurements for a site in Hanover, Germany. The comparison with field data is very good only for some species. For other species differences occur and a possible cause could be identified. A sensitivity study demonstrates the relevance of processes with small scale variability such as the reduction of photolysis rates through local shading. This highlights that the evaluation should not just include the model output, but also the complete configuration including all input data and parameters in order to ensure consistency.

Further than the assessment of concentrations, such an evaluated model can also be used to support the placement of new in-situ measurement sites at sensible location with regard to the representativeness. The spatial analysis of a realistic situation highlights this problem for the urban canopy layer.

Zusammenfassung

Städtische Luftqualität ist ein sehr aktuelles Thema in Deutschland und in anderen Ländern in Europa. Große Stadtgebiete sind Luftverschmutzung ausgesetzt die als für die menschliche Gesundheit schädlich betrachtet wird. Wo Überschreitungen gesundheitsrelevanter Schwellwerte auftreten müssen die Behörden einen Luftreinhalteplan aufstellen. Dieser kann weitreichende Konsequenzen haben, bis hin zu Fahrverboten in einigen Straßen für besonders hoch emittierende Fahrzeuge. Um solche Maßnahmen rechtfertigen zu können muss die Belastung verlässlich und qualitätsgesichert bestimmt werden. In der EU-Gesetzgebung nach der sich der Immissionsschutz in Deutschland richtet sind Vorgaben für die Repräsentativität bei der Bestimmung von Schadstoffkonzentrationen niedergelegt.

Immissionen von Schadstoffen erreichen in der städtischen Grenzschicht oft hohe Werte, insbesondere in der Nähe von Hauptstraßen oder an Orten mit geringer Belüftung. Die städtische Grenzschicht zeichnet sich durch besonders heterogene Bedingungen aus. Schadstoffemissionen können sehr lokal begrenzt auftreten und sind zeitlich und räumlich sehr variabel. Lokale Hinderniskonfigurationen und meteorologische Bedingungen bestimmen das Windfeld welches wiederum Transport und Ausbreitung von Schadstoffen bestimmt. Um den Einfluss auf die menschliche Gesundheit zu bestimmen müssen die Konzentrationen mit guter räumlicher und zeitlicher Auflösung vorliegen. In komplexem Gebiet haben Punktmessungen nur eine sehr begrenzte Repräsentativität, sofern nicht eine Vielzahl von Messpunkten vorhanden ist. Das hochauflösende numerische Modell das in dieser Arbeit verwendet wird kann verwendet werden um die Repräsentativität städtische Messstationen zu bestimmen oder um Konzentrationen in komplexem Gebiet

direkt zu berechnen.

Diese Dissertation trägt zur Qualitätssicherung bei der Bestimmung städtischer Luftqualität bei. Sie stellt Komponenten eines komplexen Modellsystems vor, mit dem die Untersuchung der Luftqualität unterstützt werden kann. Ergebnisse dieser Komponenten werden mittels einer aktuellen Methode mit Messdaten aus einem physikalischen Windkanalmodell verglichen. Die Evaluierung der Modellergebnisse zeigt, wie hochauflösende Modellergebnisse zu Konzentrationen in der städtischen Hindernisschicht überprüft werden können. Die weitere Untersuchung der Ergebnisse zeigt anhand eines realistischen Beispiels wie die Repräsentativität eines Messpunktes bestimmt werden kann. In einer Sensitivitätsstudie wird zudem der Einfluss von Prozessen, die städtische Immissionen bestimmen, quantifiziert.

In der Atmosphäre reagieren emittierte Schadstoffe weiter und ändern ihre Zusammensetzung auf unterschiedlichen Zeitskalen, wobei sich auch sekundäre Schadstoffe bilden können. Um diese Prozesse abbilden zu können muss das numerische Modell neben meteorologischen Gleichungen auch chemische Reaktionen berechnen. Solche Reaktionsmechanismen liegen vor und hier wird ein Reaktionsmechanismus verwendet, der ursprünglich für mesoskalige Modelle entwickelt wurde.

Die Analyse der realitätsnahen Modellrechnung hebt die geringe räumliche Repräsentativität von Konzentrationen in der städtischen Hindernisschicht hervor. Eine Sensitivitätsstudie zeigt die Relevanz kleinskaliger Variabilität wie den Einfluss der differentiellen Abschattung auf Photolyseraten.

Über die Prüfung der Modellergebnisse hinaus hat sich gezeigt, dass nicht nur das Modellergebnis selbst geprüft werden muss, sondern die gesamte Prozesskette einschließlich aller Eingadaten und Parameter muss geprüft werden.

Ein solchermaßen geprüftes Modell kann auch verwendet werden um sinnvolle Orte für neue Messstellen zu identifizieren.

Contents

List of Figures	VII
List of Tables	IX
1 Introduction	1
2 Air quality management	5
2.1 Air pollutants and their health impacts	5
2.2 Ambient concentration levels	9
2.3 Concentration hot spots	12
2.4 Emissions of air pollutants	14
2.5 Future air quality	15
2.6 Selection of pollutants for this thesis	18
3 Assessing air quality	20
3.1 Measuring air quality	20
3.2 Modelling air quality	21
4 Evaluation of simulated wind fields	26
4.1 Introduction	27
4.2 Method	28
4.3 Idealised test cases	34

4.4	Realistic test case	42
4.5	Summary and Discussion	58
5	Assessment of simulated concentrations	60
5.1	Introduction	60
5.2	Model characteristics	62
5.3	Realistic test case	66
5.4	Results	73
5.5	Spatial representativeness	83
5.6	Added value of urban canopy modelling of concentrations . . .	86
6	Analysis of shading effects on concentrations	89
6.1	Introduction	90
6.2	Method	92
6.3	Model validation	95
6.4	Results	95
6.5	Summary and conclusions	106
7	Conclusions	108
	Acknowledgements	113
A	Concentration units	115
B	Chemistry mechanism in MICTM	116
B.1	List of chemical species in MICTM	116
B.2	Emissions	119
B.3	Calculation of photolysis rates (STAR)	120
B.4	First order (photolytic) reactions	122
B.5	Higher order chemical reactions	123

C Split of VOC emissions	130
D Peer reviewed publications	131
References	135
.....	135

List of Figures

2.1 Attainment of EU limit values for NO ₂ in 2016	10
2.2 Attainment of EU limit values for O ₃ in 2016	11
2.3 Sketch of air quality regimes for urban areas	12
2.4 NO _x emissions per sector for Hamburg, Germany	15
2.5 Emission reduction for 1991–2013 relative to base year 1990	16
2.6 Annual emission reduction for 1991–2013	17
2.7 European emission ceiling and reported data for NO _x in Germany	18
2.8 NO _x emissions per sector for 1991–2013	19
4.1 Scatter plot for <i>C1</i>	37
4.2 Scatter plot for <i>C3-C6</i>	38
4.3 Result <i>C1</i>	39
4.4 Result <i>C3</i> (vertical)	39
4.5 Result <i>C3</i> (horizontal)	40
4.6 Result <i>C6</i>	40

4.7	Result <i>C6</i> (vertical)	41
4.8	Obstacle representation in the numerical grid.	45
4.9	Vertical profile of the undisturbed flow	47
4.10	Wind field for cases <i>220-03</i> and <i>220-10</i>	50
4.11	Wind field for cases <i>260-03</i> and <i>260-10</i>	51
4.12	Wind field for cases <i>270-03</i> and <i>270-10</i>	52
4.13	Scatter plots for <i>220-03</i> and <i>220-10</i>	54
4.14	Scatter plots for <i>260-03</i> and <i>260-10</i>	55
4.15	Scatter plots for <i>270-03</i> and <i>270-10</i>	56
4.16	Difference plot for cases <i>220-03</i> and <i>220-10</i>	57
4.17	Difference plot for cases <i>260-03</i> and <i>260-10</i>	58
4.18	Difference plot for cases <i>270-03</i> and <i>270-10</i>	59
5.1	MICTM flow chart	67
5.2	Wind field	69
5.3	Initial and boundary concentrations	71
5.4	Vertical profile of photolysis rates	72
5.5	Emissions in the model domain	73
5.6	Temporal profile of emissions	74
5.7	Concentration of CO	76
5.8	Concentration of NO	76
5.9	Concentration of NO ₂	77
5.10	Concentration of O ₃	77
5.11	Comparison of wind tunnel data and numerical model results for a passive tracer	79
5.12	<i>Hit</i> and <i>Miss</i> pattern for passive tracer	80
5.13	Location of field measurement sites in the model domain . . .	81
5.14	Normalised representativeness of urban measurement sites . .	83

5.15	Representativeness of background wind measurement	84
5.16	Horizontal cross section of NO ₂ background concentration (NO ₂ (ref)) calculated by MECTM in relation to canopy layer concentra- tions calculated by MICTM.	86
5.17	NO/NO _x ratio in and above the canopy layer	87
6.1	Vertical cross section of the model domain	93
6.2	Time series of individual wind speed components and chemical concentrations for the reference run	98
6.3	NO ₂ and O ₃ concentrations for the reference model run	99
6.4	Magnitude of differences for NO ₂ and O ₃ concentrations	101
6.5	Magnitude of differences for NO ₂ and O ₃ concentrations for different values of the photolysis rate on the shaded area	103
6.6	Magnitude of differences for NO ₂ and O ₃ concentrations	105

List of Tables

2.1	Guideline and limit values for human health set by WHO and EU for NO ₂	7
2.2	Guideline and limit values set by WHO and EU for O ₃	8
2.3	Exposure in relation to EU limit and WHO guideline values	11
2.4	Total number of stations and number of stations with ex- ceedances for NO ₂ in Germany	14
4.1	Properties of the idealised test cases	35

4.2	Length of recirculation zone (L) for all idealised test cases. . .	36
4.3	Hit rates for all idealised test cases	36
4.4	Test cases for Göttinger Straße	46
4.5	Hit-rates for all test cases of Göttinger Straße	53
5.1	Comparison of model results with measured data	82
6.1	Overview of chemistry settings for each model run for shading scenarios	96
6.2	Overview of meteorology settings for each model run for shad- ing scenarios	97
6.3	Overview of results for all model runs for different locations .	107

1 Introduction

Air quality is one of several stressors, particularly in urban areas (von Szombathely et al., 2017). Many air pollutants are classified as carcinogenic and a cause for respiratory and vascular diseases. For many areas air pollution remains at levels that are detrimental to human health. It not only reduces the quality of life and well-being but according to estimates of the World Health Organisation (WHO) the average life span is reduced due to air pollution by nine months in Germany and for the European Union by two years (World Health Organisation, 2006). Even higher pollutant concentration levels occur in some places globally (World Air Quality Index, 2018). Within Europe and particularly Germany there is ongoing discussion to determine suitable measures to improve air quality. This discussion has recently intensified since some roads have been closed for selected vehicles in order to improve air quality locally in some of the most polluted streets.

To justify such measures a rigorous assessment of the air quality is necessary and to assess the exposure of citizens. The legal framework for air quality management and control for Germany is derived from European guidelines. They define concentration limits for the protection of human health and other targets and define how these values should be assessed. A standard technique for this assessment is based on operational in-situ measurements at particular sites.

For highly reactive species in the vicinity of emission sources or in otherwise heterogeneous terrain, in-situ measurements can only give incomplete information about the state of air quality. Particularly in urban areas local high emission sources occur (e.g. a busy road with many cars) and unfortunately

1. INTRODUCTION

often coincide with a complex flow field (e.g. a narrow street or an intersection) leading to particularly high and highly variable concentrations. At these locations high gradients of air pollutants occur and imply a low spatial representativeness of in-situ measurements. In such highly variable conditions an approach could be to use a very high number of sampling sites. For high-quality instruments this is not operationally feasible due to the cost. Low cost so-called citizen science sensors are emerging and are distributed throughout some cities. However, their performance is currently not sufficient to obtain comparable and validated data across a range of devices.

Another possibility provided in the EU legal framework for air quality assessment is the use of mathematical models. These models can be used to assess the air quality for a whole domain usually at a certain grid resolution. They also enable the investigation of scenarios, such as the quantification of the impact of emission reductions or other measures to reduce air pollutant levels within *local air quality action plan*.

Mathematical models exist at various levels of complexity. Meso-scale chemistry models (e.g. WRF-Chem (Grell et al., 2005), TAPM (Hurley et al., 2005), CityChem (Karl, 2018), MECTM (Müller et al., 2000)) include chemical reactions but have no explicit treatment of buildings to represent the urban canopy layer. Existing micro-scale models (e.g. MISKAM (Eichhorn and Kniffka, 2010), MITRAS (Salim et al., 2018), CT-ANALYST (Hertwig et al., 2017), ADMS-urban (CERC, 2018)) include an improved characterisation of the urban canopy layer but commonly no chemical reactions. Both properties combined can be found in the micro-scale obstacle resolving model MICTM (Chapter 5) and also in the emerging model PALM4U (Maronga et al., 2019).

This thesis contributes to the assessment of air pollutant concentrations particularly in areas of high variability and low spatial representativeness. Any requirement for the representativeness of the data implicitly includes that the values are also correct within a margin of error. To this aim, components of a numerical model system are evaluated in comparison with wind tunnel data and applied for a street canyon. Flow and dispersion in the urban canopy layer is highly variable due to re-circulation around individual

buildings or blocks of buildings. Measurements are furthermore often made in the vicinity of roads which are relevant pollutant sources. Results of the model are particularly analysed for their spatial representativeness. Several parameters influence the tracer transport, dispersion and chemical reactions in the urban canopy layer. In order to highlight relevant parameters this thesis investigates the impact of shading on concentrations for an idealised domain.

The two choices of flow field model and chemistry mechanism determine the complexity of the models employed here and each implies a trade-off between considered processes and thereby potentially a higher accuracy and required computational effort. In order to allow such a model to be used in practice the computational effort has to be limited and the resolved processes geared towards the aim of the study. Here, the aim is to calculate short-term averaged results (30-60 min) for a variety of different species in a highly complex urban canopy layer.

This requires the use of a prognostic obstacle-resolving model. The model MITRAS (Salim et al., 2018; Schlünzen et al., 2003b) is used to calculate averaged flow fields in this thesis. In order to limit the cost of model calculations, it employs time-averaged equations of motion rather than averaging the results. The impact of this choice for regulatory purposes is expected to be limited because the interest is in averaged concentrations as required by the respective guidelines. The selected reaction mechanism for the micro-scale chemistry model MICTM is the reduced mechanism RADM2 (Stockwell et al., 1990) that was initially developed for mesoscale applications. It is employed here so that boundary and initial data can be provided by its meso-scale sister model MECTM (Trukenmüller et al., 2004; Meyer and Schlünzen, 2011).

To provide relevant background and context for this thesis, Chapter 2 describes air quality and its management and Chapter 3 gives an overview of applicable modelling techniques for air pollution assessment. Chapter 4 describes the selected numerical model for the calculation of the wind field and the evaluation of results. Chapter 5 describes the complex chemistry model, the evaluation of results in comparison to physical model and field

1. INTRODUCTION

measurements. To investigate further the influence of shading on urban concentrations, Chapter 6 uses a simplified model of an idealised urban street canyon. Here, the shading predominantly influences the photolysis rates. Therefore a simplified chemical mechanism is used which considers only the photochemically influenced reactions of NO_x and O_3 .

2 Air quality management

Several trace gases have relevant impacts on human health, on vegetation and sometimes on structures. Concentrations of many air pollutants are particularly high in urban areas where a large population density entails activities that lead to air pollution. Health guidelines relating to air quality are regularly exceeded in urban areas. Since most people in Germany as well as in many other places live in urban areas this leads to a high exposure of the population.

Air quality has been widely improved over the past decades and some species now generally occur at concentration levels that are not considered harmful to human health, such as SO_2 concentrations which have been lowered substantially due to emission reductions. However, several air pollutants reach concentration levels that can have detrimental effects on human health and in some cases on vegetation. At current air quality levels the most relevant species are nitrogen dioxide (NO_2) as well as oxides of nitrogen (NO_x), particulate matter of different size spectra (PM_{10} , $\text{PM}_{2.5}$, PM_{1}) and ozone (O_3).

This chapter provides background on relevant air pollutants, their health effects and current and expected concentration levels.

2.1 Air pollutants and their health impacts

This section presents the health impacts of those pollutants for which ambient concentration levels in Germany are relevant to human health. Most of these pollutants are primary pollutants, i.e. they are emitted into the air, primarily

2. AIR QUALITY MANAGEMENT

from fossil fuel burning. Other species are produced from chemical reactions in the air and are therefore secondary pollutants. The health impacts can be categorised into long-term exposure and short-term exposure. Short-term health effects can be determined from chamber experiments exposing animals or humans. Long-term health impacts are generally gained from epidemiological studies which correlate prevalence of adverse health effects with exposure. Based on both types of studies the World Health Organisation (WHO) has derived Air Quality Guidelines (AQG). The AQG contain advisory limit values for the protection of human health (World Health Organisation, 2006) for short-term and long-term exposure. The European Union and its member states have set limits for ambient concentrations of harmful substances based on the WHO guidelines but also considering the feasibility to attain the values. The European Union distinguishes *limit values* which are a legally binding threshold value, *target values* which are less strict values that have to be met if possible, and *long-term-targets* which are future limit or target values without a fixed date. Limit and target values are in some cases equal to the Air Quality Guidelines, but in most cases they are higher. This implies that even if the member states comply with the legal limits, significant health impacts for the population can be expected.

2.1.1 Nitrogen dioxide

Nitrogen dioxide (NO_2) is a primary pollutant emitted from fossil fuel burning, but major contributions to ambient concentrations are from nitric oxide (NO) which quickly reacts with ozone (O_3) to form NO_2 (Section 6.2.1). NO_2 is also highly correlated with other air pollutants so that the health effects cannot always be separated. It can therefore be used as a proxy for other pollutants when allowed concentration levels are set. Although impacts of short-term concentration levels of $500 \mu\text{g}/\text{m}^3$ have been found to be harmful in laboratory studies, the short-term limit value has been set to a lower concentration to account for the health impact of other correlated substances. Long-term exposure to elevated concentrations of pollutants can be harmful for the lungs. Asthmatic children may exhibit bronchitic symptoms and lung development is hindered in epidemiological studies. The limits set by WHO

Type	Averaging period	WHO [$\mu\text{g}/\text{m}^3$]	EU [$\mu\text{g}/\text{m}^3$]
Short-term	1 hour	200	200*
Long-term	1 year	40	40

Table 2.1: Guideline and limit values for human health set by WHO and EU for NO_2 .

and EU for NO_2 are summarised in Table 2.1.

2.1.2 Oxides of nitrogen

Nitrogen dioxide is often considered together with nitric oxide NO as oxides of nitrogen (NO_x). While the ratio of NO_2 and NO may change quickly depending on ambient ozone concentrations and short wave radiation (Section 6.2.1), NO_x levels change in much slower reactions. Oxides of nitrogen add to the acidification of soil and water and may contribute to changes in species diversity through eutrophication (European Environment Agency, 2015). There are no limit values specifically for NO_x in urban areas.

2.1.3 Ozone

Ozone (O_3) is not directly emitted but quickly formed as a secondary pollutant from the photolysis of NO_2 (Equation 6.1) and in a slower reaction from volatile organic compounds (VOCs). It is quickly destroyed in a reaction with NO (Equation 6.2). These are the most relevant reactions near sources of oxides of nitrogen and the reactions quickly reach an equilibrium called photostationary state. Ozone is also removed from the air by deposition on surfaces.

Acute health effects on the lungs occur at $160 \mu\text{g}/\text{m}^3$ for exercising people and significant health effects are observed at $290 \mu\text{g}/\text{m}^3$ also in resting people. Since there is considerable variation in the reaction of individuals, the 8-hour-guideline recommendation by World Health Organisation (2006) is set to $100 \mu\text{g}/\text{m}^3$ expecting that some sensitive individuals may react below this

*currently 18 exceedances permitted per year

2. AIR QUALITY MANAGEMENT

Type	Averaging period	WHO [$\mu\text{g}/\text{m}^3$]	EU [$\mu\text{g}/\text{m}^3$]
Short-term	8 hour	100	120 [†]
Information	1 hour	—	180
Alert	3 consecutive 1 hour	—	240
Vegetation	AOT40	—	18'000 [‡]

Table 2.2: Guideline and limit values set by WHO and EU for O_3 .

value. Long-term effects on human health are inconclusive, so that no annual recommendation has been set by World Health Organisation (2006).

At current background concentrations, ozone also has effects on vegetation by inhibiting crop, forest and plant growth. Therefore, the EU has set an integral annual limit value, named AOT40. It considers the sum of all concentrations above a level of 40 ppb(=80 $\mu\text{g}/\text{m}^3$) during the daytime (8 a.m.–8 p.m.) in summer (May–July).

In some cases entrainment of stratospheric ozone may lead to natural exceedances. To account for such natural exceedances, the attainment of EU limit and target values is averaged over 3–5 years. The limits set by WHO and EU for O_3 are summarised in Table 2.2.

2.1.4 Volatile organic compounds

The term volatile organic compounds (VOCs) describes various organic species with high vapour pressure (volatility) at ambient temperatures. Their sources can be natural, e.g. from plants which emit VOCs and use them for communication. There are also various anthropogenic sources such as evaporation from fuel or solvent use and from many industrial processes and products. VOCs can themselves be harmful for human health (e.g. carcinogenic) but also contribute in slow reactions to the formation of O_3 . VOCs are often separated into methane (CH_4) and non-methane volatile organic compounds (NMVOCs).

[†]currently 25 exceedances permitted per year; long-term objective: no exceedances

[‡]long-term objective 6'000 $\mu\text{g}/\text{m}^3$

2.1.5 Particulate matter

Particulate matter PM is a collective term for various non-gaseous materials in the air. Their state can be solid or liquid and the composition varies widely depending on the source. Some part is emitted directly, e.g. as fine dust particles which may be either natural or anthropogenic. Natural sources can be dust from dry surfaces or sea salt aerosols. Anthropogenic sources are from industrial processes and from burning of e.g. fossil fuels, but in urban areas relevant sources are from traffic. This includes direct exhaust emissions from vehicles, grit from break pads and from tires of vehicles. There is also a contribution from resuspension of materials that have already deposited on surfaces (Timmers and Achten, 2016).

Particulate matter is categorised by its size spectrum and usually coarse particles with a size below $10\mu m$ (PM_{10}), fine particles with a size below $2.5\mu m$ ($PM_{2.5}$) and ultrafine particles with a size below $.1\mu m$ ($PM_{0.1}$) are distinguished. The health effect varies with the size of the particles. Coarse particles are filtered by the lungs where they remain and accumulate. They are carcinogenic and can lead to inflammation of the lung. Fine particles can also penetrate the lung to reach the vascular system where they can contribute to cardio-vascular diseases. Ultrafine particles can already penetrate the tissue of the upper respiratory tract where they can deposit in brain tissue near the nasal passage (Oberdörster et al., 2004).

2.2 Ambient concentration levels

Exceedances of EU limit values occur regularly in a number of countries. Figures 2.1 and 2.2 show the overall attainment of EU limit values in 2016 for NO_2 and O_3 , respectively. The graphs are based on the annual limit value (NO_2) and on the 26th highest value of the running 8-hour mean (O_3) for each station. The black dot indicates the average of this value for all stations. The box indicates the 25th and 75th percentile. Black vertical lines show the overall range of values. The red line indicates the relevant limit or target value. This presentation of the data means that even if in

2. AIR QUALITY MANAGEMENT

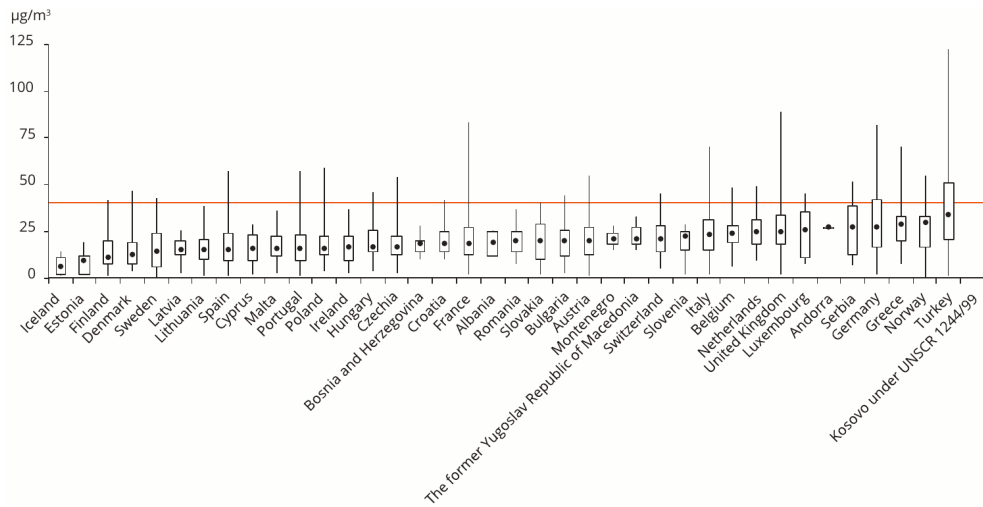


Figure 2.1: Attainment of EU limit values for NO_2 in 2016. See text for details. (reproduced from European Environment Agency (2018))

the average the concentration is below the EU limit value, this could be the case because low concentrations in clean areas compensate pollution at sites where the limit values are exceeded. Every country where any part of the graph exceeds the red line suffers exceedances. Figure 2.1 shows a large variability of concentrations within each country. The overall variability is related to the number of stations in each country so that in general very small countries experience a smaller range of values. The majority of countries experience exceedances at some stations, however, only for Germany and Turkey more than 25% of stations exceeds the limit value. This may not necessarily indicate low air quality throughout the country but may be related to the overall distribution of stations in each country (Chapter 2.3). For O_3 the variability of concentrations within each country is lower, as shown in Figure 2.2. Just over half of the countries experience no exceedances for O_3 . But half of countries with exceedance experience these at at least 25% of the stations.

While many EU countries experience exceedances of limit value for the protection of human health, what is arguably more relevant than the number of stations with exceedances is the exposure of the population. The exposure depends on the distribution of the population in relation to the measurements stations. Table 2.3 shows estimates of the exposure of the population

2. AIR QUALITY MANAGEMENT

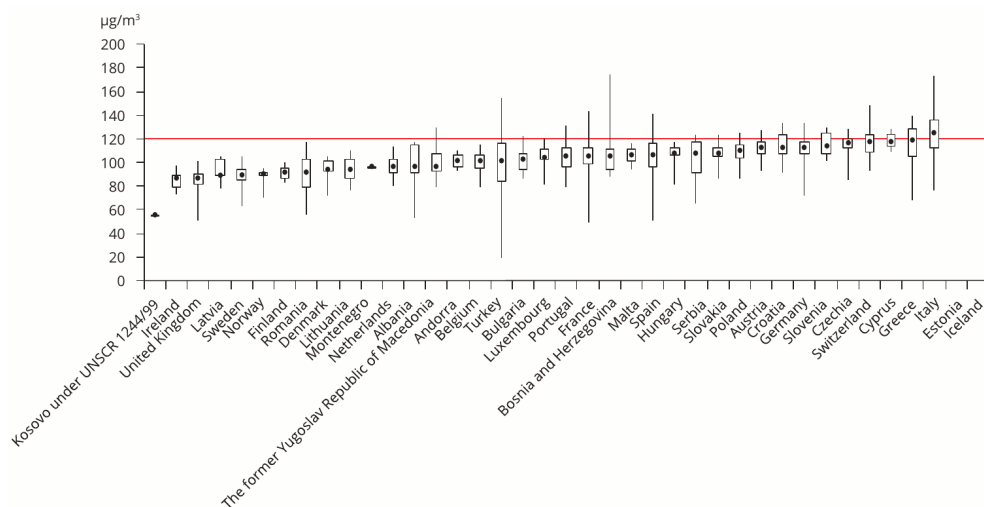


Figure 2.2: Attainment of EU limit values for O₃ in 2016. See text for details. (reproduced from European Environment Agency (2018))

Species	Averaging period	EU		WHO	
		Limit [$\mu\text{g}/\text{m}^3$]	Exceedance [%]	Guidance [$\mu\text{g}/\text{m}^3$]	Exceedance [%]
NO ₂	year	40	8–12	40	8–12
O ₃	8-hour	120	14–15	100	97–98
PM ₁₀	day	50	17–30	20	61–83
PM _{2.5}	year	25	9–14	10	87–93

Table 2.3: Estimated exposure of the EU-28 population in 2011–2013 in relation to EU limit and WHO guideline values. Numbers show the fraction of the population exposed to concentration levels exceeding the limit or guideline value (from European Environment Agency (2015)).

of EU-28 to concentration levels exceeding the current EU limit value for different species. Overall the exceedances affect a significant fraction of the population. Highest exposure of exceedances occurs for coarse particulate matter, but exceedances affect a substantial fraction of the population also for NO₂ and O₃. In order to assess the health impact the exceedance of the generally lower WHO guideline values shown in the same table may be more relevant. The data show that most of the EU population experience exceedances of the guideline value for O₃, PM₁₀, PM_{2.5} and at a lower extent to NO₂.

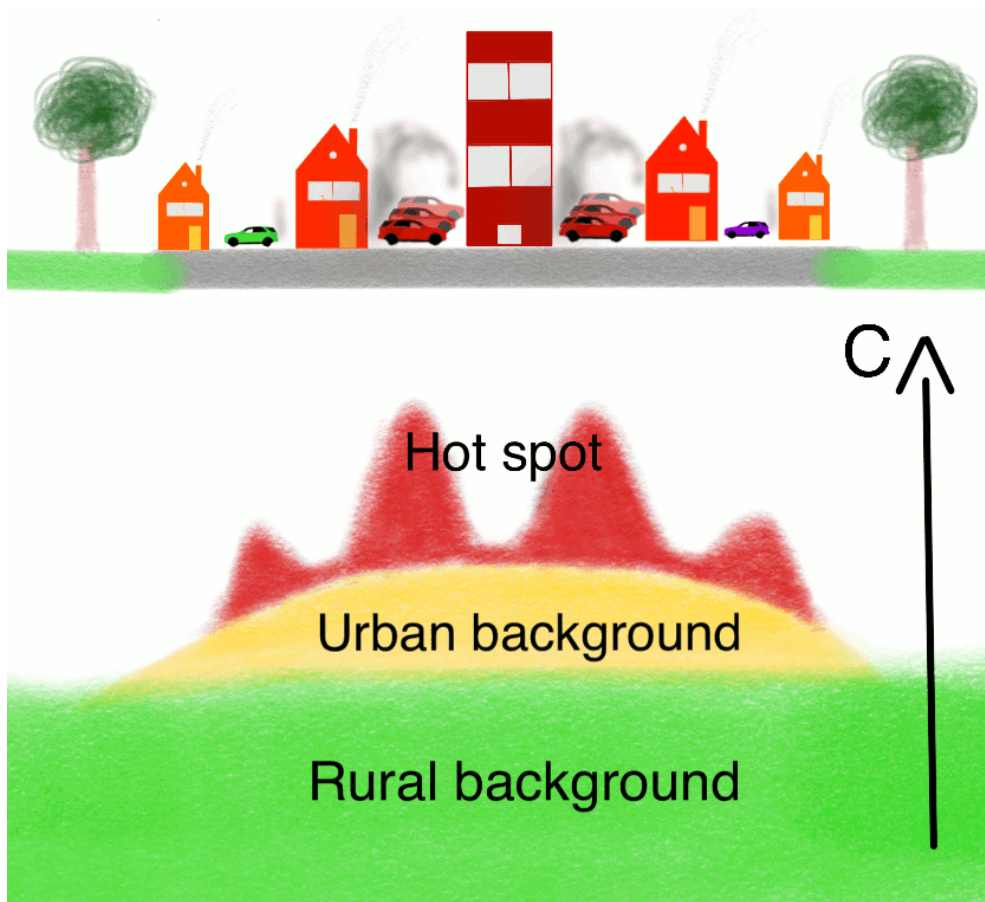


Figure 2.3: Sketch of emission and ventilation regions (top of the figure) and related air quality regimes (bottom of the figure) for pollutants emitted primarily from fuel burning. For detailed description see text. (after Minkos et al. (2018) and Lenschow et al. (2001))

2.3 Concentration hot spots

Anthropogenic emissions are spatially correlated with human activities, such as large sites of fuel burning for energy production. Less centralised fuel burning occurs for industrial production and household consumption which increases for urban areas. Very localised emission of pollutants occurs in urban areas where also the ventilation of is impeded by reduced wind speeds and obstruction of the flow by large building complexes.

Depending on the geometry and density of buildings different ventilation

situations occur as described e.g. by Oke et al. (2017): Individual buildings are seen as isolated roughness elements and ventilation is possible. As the density of buildings increases the individual building wakes interfere still permitting ventilation. If buildings are placed increasingly dense as in an urban street canyon, the ventilation is impeded and tracer emissions may accumulate in the street canyon for some wind directions. The bottom part of the urban boundary layer where this occurs is referred to as the urban canopy layer (Oke et al., 2017). It is often characterised by a combination of high emissions and low ventilation and reaches from the ground up to approximately the height of the buildings.

Different emission and exposure regimes can be characterised relating to urban areas (Figure 2.3): In rural areas (indicated by trees) emissions are of comparatively low magnitude and homogeneous. Some high emissions from e.g. energy production are emitted at higher altitudes and are partially mixed back towards ground level. Only few obstacles impede the flow so that concentrations can be well mixed and a relatively homogeneous rural background concentration can be found for many pollutants (concentration levels shown in green). Towards urban areas fuel burning generally increases at ground level and in the canopy layer due to e.g. traffic, industry and heating of homes (indicated by low rise buildings and cars). At some distance to individual emission sources the pollutants are well mixed in the canopy layer and concentrations show the urban background (higher concentration levels shown in yellow). Within the urban area local emission sources increasingly occur and the ventilation of pollutants from the canopy layer is very variable depending on the configuration of buildings (indicated by high rise buildings and cars). Particularly when high emissions coincide with low ventilation local concentration maxima called *hot spots* can occur (highest and most variable concentrations shown in red).

This pattern is supported by measurements at air quality sites for Germany. Table 2.4 shows the exceedances of the EU limit value for NO₂ at air quality sites in Germany for the most recent years. Since 2015 all recorded exceedances are at traffic stations, i.e. at stations near hot spots. No exceedances for NO₂ have recently occurred at urban background sites or at

2. AIR QUALITY MANAGEMENT

Year	Number of background stations		Number of traffic stations		
	all	with exceedances	all	with exceedances	
2010	179	2	219	163	74%
2011	174	1	229	172	75%
2012	171	1	244	170	70%
2013	176	1	250	168	67%
2014	177	1	238	148	62%
2015	174	0	244	142	58%
2016	173	0	246	145	59%
2017	170	0	250	111	44%

Table 2.4: Number of stations and number of stations with exceedances for the annual mean value for NO₂ in Germany. Data from Umweltbundesamt (2018a).

rural sites and in previous years only one or two. Over the time period shown the number of traffic stations that show exceedances has reduced from 75% to 44%.

High population densities in urban areas often coincide spatially with high local emissions and often with hot spot locations and therefore the exposure of residents to unhealthy concentrations is especially high. Therefore, there is a particular requirement to assess the air quality near hot-spot sites such as street canyons with high traffic counts.

2.4 Emissions of air pollutants

The described gaseous air pollutants are predominantly emitted from burning of fossil fuels. Fossil fuel burning occurs for several activities commonly categorised as industry, household and different traffic sectors. Figure 2.4 shows the relative contribution of different sectors to NO_X emission in Hamburg for data between 2012 and 2014. The main contributions are from different transport sectors, followed by industry and household emissions. Road traffic contributes almost a third of NO_X showing that roads which cover only a small fraction of the city shoulder a major fraction of the emissions. The high contribution of shipping emissions is probably particular for Ham-

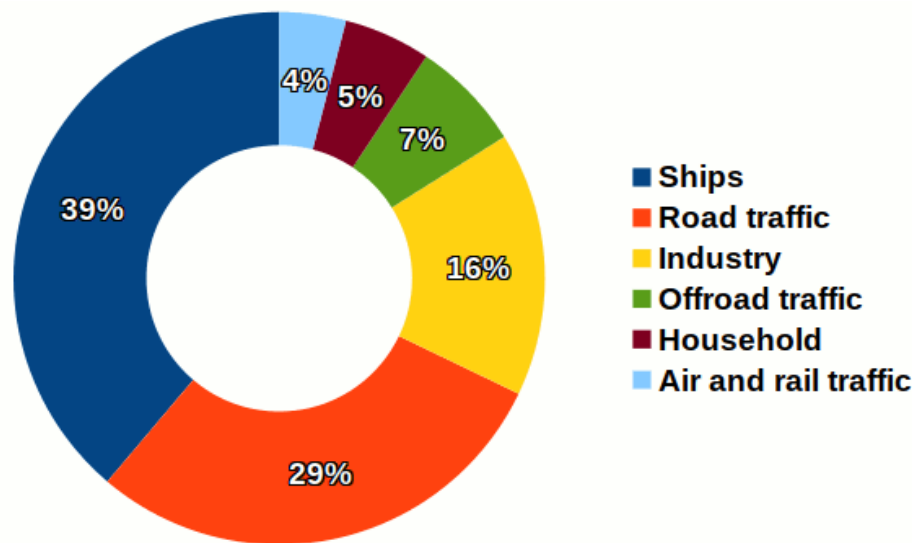


Figure 2.4: NO_x emissions per sector for Hamburg, Germany. Estimates from various sources for different years 2012–2014. Data collated by FHH–BUE (2017, Table 21).

burg (or other harbour cities) and it is also very difficult to estimate because shipping engines and fuel are less regulated than road traffic.

Air quality management has led to extensive reductions of the emissions for most species and across most sectors. Figure 2.5 shows emission reductions of several air pollutants in relation to the base year 1990. For SO₂ the desulphurisation of energy production and also of traffic fuel has led to a reduction to less than 10% of the base year. Reductions of NO_x and NMVOC emissions are lower but also continuous since the base year. Figure 2.6 shows the emission reductions year–on–year. While there are significant reductions in the 1990s, the reductions level out around the year 2010 and year–on–year reductions and in some cases an increase occurs.

2.5 Future air quality

The previous section has presented substantial changes in emissions, concentrations and exposure to air pollutants within the European Union. However, further reductions are required in order to fulfil current requirements.

2. AIR QUALITY MANAGEMENT

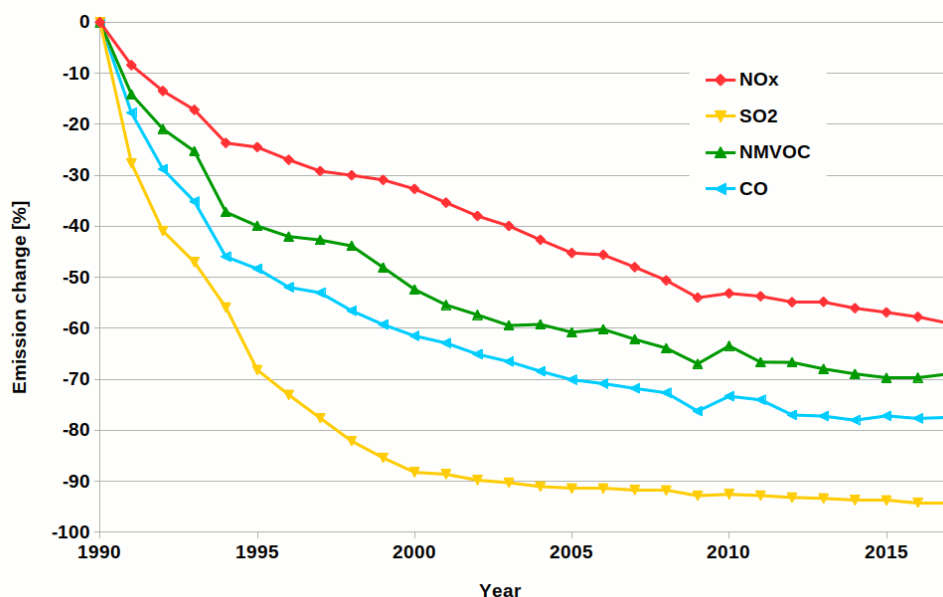


Figure 2.5: Emission reduction for 1991–2013 relative to base year 1990. Data from Umweltbundesamt (2019).

Therefore, the European Union has set emission reduction targets until the year 2030 for substances including NO_x and NMVOC (European Communities, 2001). The first emission reduction target was for 2010 which limited NO_x emissions for Germany to 84% of those of the year 2005. Two more reductions are set for the year 2020 to 61% and for the year 2030 to 35%. Therefore, significant reductions of NO_x emissions and NO_x concentrations may be expected, reducing the health impact of NO_x for the population.

However, as reported by the European Environment Agency (2016), Germany has consistently exceeded the emission ceiling for NO_x and VOCs between 2010 and 2014. For NO_x this is also true for Austria, Belgium, France, Ireland and Luxembourg. Other countries have exceeded the ceiling for only some years. Exceedances of other pollutant occur as well. Only half of the countries have fulfilled their obligations for the period 2010 – 2014. Changes have since been made to the emission inventory calculation according to the Gothenburg protocol (European Environment Agency, 2016). Figure 2.7 shows the NO_x emission ceiling for Germany and reported emissions which fulfil the emission ceiling for Germany considering the Gothenburg Protocol.

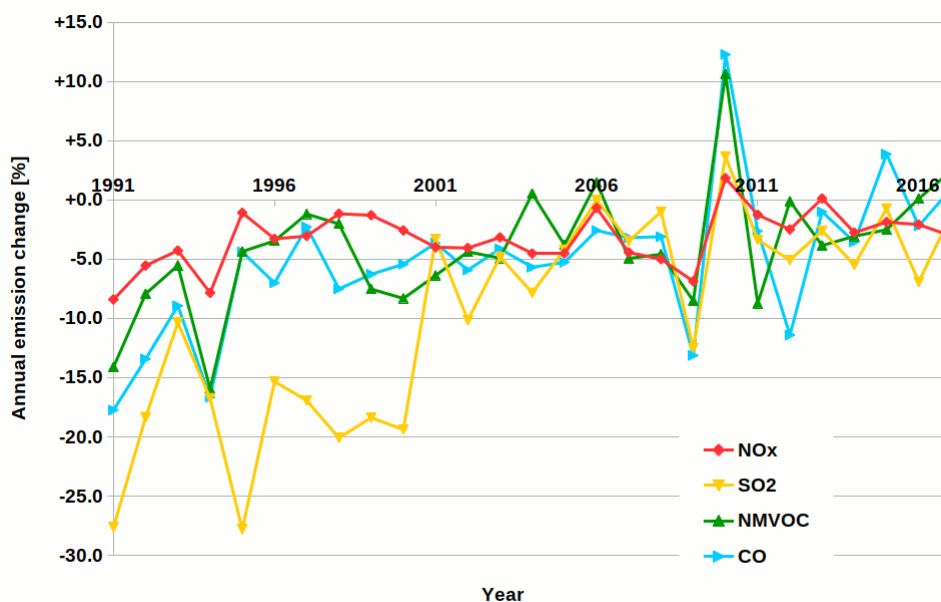


Figure 2.6: Annual emission reduction for 1991–2013. Data from Umweltbundesamt (2019).

The reported exceedances give rise for concern that emissions may remain higher than anticipated under the emission ceiling.

Emission reductions are for NO_x while the concentration of pollutants and the health impact are considered mainly for NO_2 . Estimated reductions of NO_x emissions are not necessarily accompanied by equal reductions in NO_2 concentrations. Depending on the type of engine the emission ratio of NO_2 and NO will be different, varying the primary emission of NO_2 . Also the near-source concentration (e.g. in a narrow street canyon) is affected by the composition of the ambient air, for NO_2 the concentration ratio of NO_2 and NO as well as O_3 are particularly relevant (Equations 6.1 and 6.2), but also concentrations of VOCs are relevant. All these influences are affected by changing traffic composition and by a changing regional climate with different biogenic VOC emissions, air temperatures and solar radiation. Figure 2.8 shows NO_x emissions per sector since the year 1990. The figure shows that since 2010 NO_x emission reductions have declined and traffic contributions do not currently decrease further. Also a shift of the NO_x -composition towards higher fractions of NO_2 has been observed (Carslaw,

2. AIR QUALITY MANAGEMENT

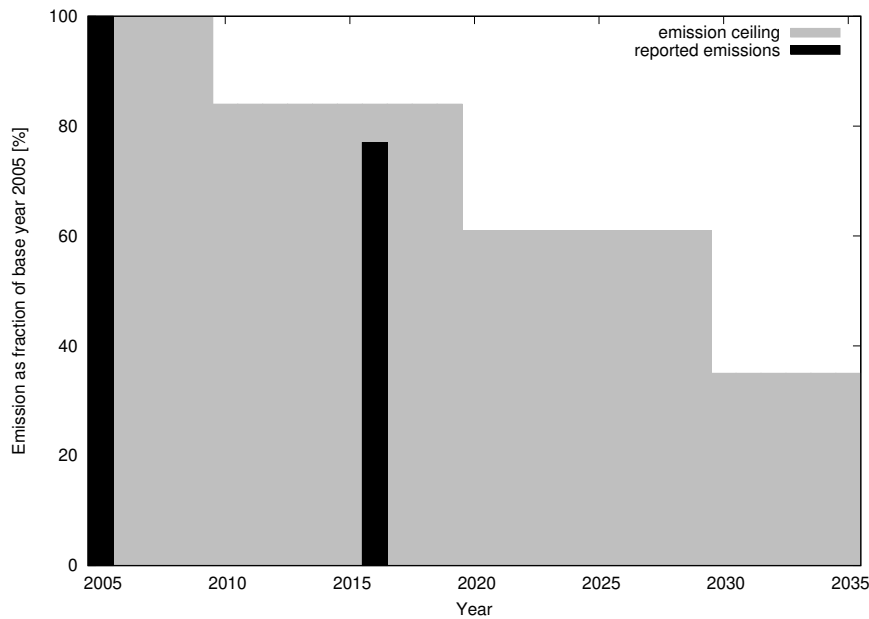


Figure 2.7: European emission ceiling and reported data for NO_x in Germany. Grey shading shows the emission ceiling for Germany. Black shading shows the reported emissions considering the Gothenburg protocol. Data from Umweltbundesamt (2018b) and European Environmental Agency (2019).

2005).

2.6 Selection of pollutants for this thesis

Street canyons with high emission rates and relatively low ventilation are particular hot-spot locations. All reported exceedances of NO_2 limit values in Germany in recent years have occurred at traffic sites. Concentration levels relevant for human health currently occur for nitrogen dioxide, ozone, and particulate matter. Therefore, the gaseous species nitrogen dioxide and ozone are further investigated in this thesis. To complete the photochemical equilibrium nitrous oxide is also included.

For particulate matter further processes are relevant, especially for emission modelling which may be caused by traffic but can also be triggered by current and past wind and precipitation. Particulate matter is therefore not the focus of this work. Within the relatively short residence time of the pollutants

2. AIR QUALITY MANAGEMENT

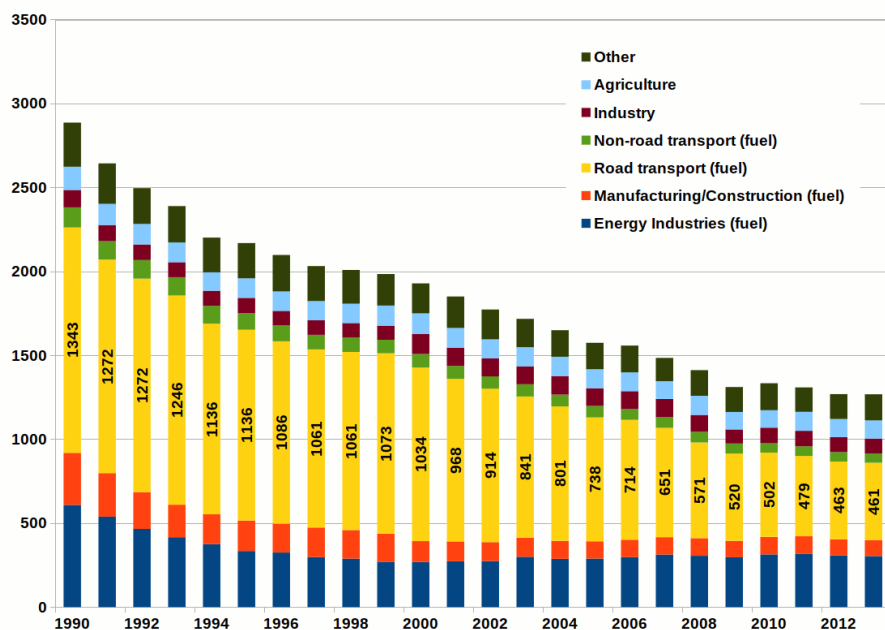


Figure 2.8: NO_x emissions [kt] per sector for 1991–2013. Data from Umweltbundesamt (2019).

within the urban canopy layer, no significant reactions of carbon monoxide (CO) are expected. This is also the case for particulate matter. If therefore passive transport can be assumed within the street canyon for both species, the transport of CO can be used as a proxy for particulate matter (keeping in mind that other influences such as emission, deposition and background concentrations vary) and some conclusions may be transferred to particulate matter.

Even though emission and concentration reductions have been successful for some species in the past, Section 2.5 (Figure 2.7) shows that pollutant concentrations are likely to persist for several decades. Even if current combustion engines are widely replaced with electric engines, some particulate matter emissions from wear and tear of rubber tyres, brake pads and other materials would remain.

3 Assessing air quality

The assessment of ambient concentrations can in general be based on measurements or modelling. In order to provide meaningful data for health assessments and regulatory attainment the concentration data has to be representative of a certain area. This implicitly includes the requirement that it is also correct within certain boundaries. But particularly at urban hot-spot locations, many parameters governing pollutant concentration are highly variable in space and time. The building configuration influences the flow field so that flow patterns with multiple re-circulation zones occur. For street canyons a ventilating vortex may occur in the canyon or more stagnating flow near the bottom for particularly narrow street canyons. Measurement sites placed in an urban street canyon are very close to traffic which is the dominant local emission source so that strong concentration gradients can be expected. Chemical reactions based on varying meteorological parameters such as temperature and short-wave radiation add further variation in space and time. For regulatory purposes at hot-spot locations the required spatial representativeness is 200 m^2 (European Communities, 1996, 1999) or a stretch of 100 m along the street (European Union, 2008), respectively. How this representativeness should be determined is not defined (Diegmann et al., 2014).

3.1 Measuring air quality

For EU guidelines the recommended technique is based on in-situ measurements. They allow to determine a full concentration time series based on

the actual weather and emission conditions. However, the required spatial representativeness cannot necessarily be achieved for operational stations as can be seen from comparison measurements at several sites within one street canyon, (e.g. Reich and Peschke, 2013) where even the annual mean varies substantially. In most cases this variability might not be noticeable in long-term averages such as the annual mean (Vardoulakis et al., 2005), but regulatory limit values based on short-term averages require high-quality hourly data. In order to achieve a high representativeness for short-term values, a high spatial density of measurements could be used. However, this is often not feasible due to high demands for infrastructure and cost.

To address the low spatial representativeness, European Union (2015) sets guidelines for the assessment of air quality from measurements. It stipulates the geometric placement of sampling sites in the vicinity of buildings. The location should be at least 25 m from major junctions and no more than 10 m from the kerbside. The inlet should be at a height of between 1.5 m and 4.0 m and without any obstructions of the airflow in the vicinity (some metres). In complex terrain it is sometimes not possible to follow all guidelines, so that the siting has to be documented including all deviations.

Low-cost sensors for particulate matter concentrations as well as other atmospheric variables are emerging and are often used in citizen science projects (e.g. <http://luftdaten.info>). They aim to overcome the low spatial representativeness of each sensor and its possible errors by deploying a high number of sensors. However, due to possible variation between individual devices, the set-up of each sensor and the lack of data about the precise siting these sensors cannot currently contribute in the regulatory context of this study.

3.2 Modelling air quality

An alternative to measurements are high-resolution models. Physical scale models in a wind tunnel can be used to investigate flow and dispersion (VDI, 2000). In a wind tunnel a scale model is implemented in a realistic boundary layer where similarity laws are fulfilled. Passive tracers are used, so that chemical reactions are not considered. Thermal stratification can be consid-

ered in some wind tunnels, but in practice this is rarely used for realistic situations.

Mathematical models with a wide range of complexity exist. With increasing complexity of the models more local and highly variable influences can be included such as the calculation of the wind field, consideration of thermal stratification, radiation and chemical reactions. However, the computational cost of the model calculation rises. Therefore, each type of model has a particular area of application which weighs the cost and benefit of additional complexity.

If the model resolution is adequate, numerical models may be able to fulfil the requirements for spatial representativeness and obtain data for regulatory purposes. A representative result may be achieved by running a model at a higher resolution and averaging over the required representative area. However, for a meaningful representativeness the model does not only need to be able to procure data at a certain spatial scale, but these data (or the process by which they are derived) need to be evaluated to ensure they are realistic. Such evaluated data can also be used to support the siting of operational measurement sites, the interpretation of measurements and for the investigation of scenarios.

3.2.1 Flow field from parametric models

A computationally efficient way to calculate dispersion of emissions is by use of a simple parametric model, such as the Gaussian model. This includes parameters for different dispersion conditions based on measurements. Within the urban canopy layer with complex flow features such as re-circulation zones in the vicinity of buildings these relations do not generally apply. The quasi-Gaussian model ADMS-Urban (CERC, 2018) therefore includes additional parametrisations to account for building influences. The performance of such models still highly depends on the complexity of the flow pattern.

Diagnostic models initialise with a first-guess wind field and then ensure mass-consistency of the wind field considering the terrain. Parametrisations for the influence of individual buildings on the flow field may be included.

This type of model is mainly used for screening applications (Vardoulakis et al., 2007) or where on-line data is required for large areas.

3.2.2 Flow field from prognostic models

Prognostic models are derived from fundamental physical laws with some simplifications. They solve equations based on the conservation of mass, momentum and energy on a numeric grid. The solutions are time dependent and governed by initial and boundary conditions. These equations could be directly solved in a Direct Numerical Simulation (DNS) model resolving all spatial scales. These are (currently) too computationally expensive to employ for large realistic domains (CERC, 2018).

The large vortices within turbulent flow are much more effective in their impact on transport and dispersion than small vortices. A simplification of the DNS calculation is therefore to separate the turbulent vortices by their size using a filter and calculate the large vortices directly. The impact of small vortices is calculated in a turbulence model. This Large Eddy Simulation (LES) approach requires a relatively high spatial resolution and therefore still has a comparatively high computational cost.

Another approach to reduce the computational effort is to average the momentum equations over time leading to the Reynolds-averaged Navier-Stokes (RANS) equations. The resulting system of equations is not closed so it also requires the introduction of a turbulence parametrisation to account for turbulent mixing. This solution is not time-dependent and leads to a quasi-stationary solution unless the boundary conditions are time dependent.

LES has the potential to provide more accurate and more reliable results than RANS, particularly for non-linear processes and if non-averaged results are sought. This can only be achieved with a higher computational effort and with high requirements on the input data (Blocken, 2018). Both methods, LES and RANS, are commonly used in research. However, in practice the prevalent method to calculate dispersion around complex buildings remains RANS. Therefore, also best practice guidelines with a focus on RANS are more readily available (VDI, 2017b; Franke et al., 2011).

3.2.3 Concentrations from simple relations

Empirical conversion rates may be derived to account for the conversion of NO_x emissions near the source. Simple conversion rates do not account for ambient conditions such as short-wave radiation and temperature and for background concentrations of the relevant species.

Compared to the residence time of pollutants in the domain, some gaseous species have very low reaction rates so that they can be considered as non-reactive. Of the species emitted by road traffic this may be the case for e.g. NO_x ($= \text{NO}_2 + \text{NO}$) or carbon monoxide (CO).

3.2.4 Explicit chemical reactions

Chemical mechanisms are sets of chemical reactions that represent the chemical transformation in a required level of detail. Efforts exist to provide a nearly explicit mechanism for tropospheric gas phase chemistry. The Master Chemical Mechanism (MCM) is such an effort (Jenkin et al., 2003, 1997). This mechanism currently contains some 17000 chemical reactions of 6700 species (MCM, 2018). For applications in a regional or urban scale model with $O(10^6)$ grid points this is computationally too expensive. Therefore, sub-sets of the chemical reactions have been derived for specific applications. Depending on the target species the mechanism can be reduced by *lumping* several species together to react as one and by considering the characteristic time scale of the reactions. For regional applications several such reduced mechanisms have been developed. These include the EMEP mechanism (79 species in 141 reactions) (Simpson et al., 1997), RADM2 (63 species in 158 reactions) (Stockwell et al., 1990) and RACM (77 species in 237 reactions). The performance of these mechanisms varies slightly by application and computational domain. While the EMEP mechanism is intended primarily for the boundary layer, RADM2 and RACM represent the full troposphere. The performance of these three mechanisms varies little for rural areas. Differences can be found for urban areas but without identification of a most suitable mechanism (Gross and Stockwell, 2003).

A more extensive reduction is the focus on very fast chemical reactions. The concentrations of NO_2 , NO and O_3 are very closely linked by fast reactions (Section 6.2.1). If slower reactions with e.g. VOCs are not considered, the reaction mechanism can be reduced to just three reactions. VDI (2017a) includes another reduction of the RACM mechanism to 32 reactions. Application of this mechanism and of a simple NO_x - O_3 -reaction system shows the magnitude of differences compared to the RACM mechanism for calculations over 240 min. The NO_x - O_3 -reaction system shows highest differences to a complex reaction mechanism for concentrations below 20 ppb and above 1000 ppb NO_2 where the differences can exceed 100%. Differences in the interim range reach up to approximately 25% and are consistently over-predictions or under-predictions depending on the time of day. The differences occur in a concentration range that is relevant for urban areas and increase with the concentration of NO_2 . The difference for the mechanism with 32 reactions is generally lower (compared to RACM) and high differences only occur during daytime for concentrations below 10 ppb NO_2 . The residence time for traffic emissions within a typical domain depends on the meteorological conditions. A simple rule of thumb is used here to derive which order of magnitude may be realistic for the residence time for a micro-scale obstacle resolving model. Assuming stagnant conditions with an average wind speed of $< .5 \text{ m} \cdot \text{s}^{-1}$ near the ground an air parcel would travel across a model domain for a city quarter of 1'800 m length within one hour. In reality, complex flow patterns in the canopy layer will increase the residence time and ventilation out of the canopy layer will decrease the residence time. According to this estimate, if stratification limits vertical exchange, it should take in the order of 1 h to exchange the air.

4 Evaluation of simulated wind fields

This chapter has been published as:

Grawe, D., Schlünzen, K. H., Pascheke, F., 2013a. Comparison of results of an obstacle resolving microscale model with wind tunnel data. *Atmospheric Environment* 79, 495–509.

doi: [10.1016/j.atmosenv.2013.06.039](https://doi.org/10.1016/j.atmosenv.2013.06.039)

The chapter includes the full manuscript of the published article except for some editorial changes. Layout and numbering have been adapted to the thesis document. The abstract is not included and references and acknowledgements have been integrated into the separate sections of the thesis document.

The evaluation technique applied and further developed in this chapter was devised in a working group of The Association of German Engineers (VDI) of which David Grawe is a member. Frauke Pascheke has contributed the wind tunnel comparison data and Frauke Pascheke and K. Heinke Schlünzen have contributed some ideas for the analysis.

4.1 Introduction

European air quality legislation requires EU member states to thoroughly assess the air quality in their respective territories (European Communities, 1996, 1999, 2000). These guidelines address 13 different pollutants and define metrics required for their assessment. Depending on the specific location of the assessment, different spatial representativeness of the metrics is required, ranging from at least 1000 km^2 for areas where the protection of the vegetation and ecosystems is subject of the assessment down to an area of no more than 200 m^2 in urban hot spot locations. To assess air quality for such a wide range of resolutions, a multi-scale numerical model system is required and thus M-SYS has been developed (Trukenmüller et al., 2004). M-SYS employs the mesoscale meteorology model METRAS (Schlünzen, 1990) and the mesoscale chemistry model MECTM (Lenz et al., 2000; Müller et al., 2000; Schlünzen and Meyer, 2007), and the respective microscale models MITRAS (Schlünzen et al., 2003a; Lopez et al., 2005) for meteorology and MICTM (Grawe and Schlünzen, 2019) for chemistry, together with the required pre- and post-processors. These models use consistent equations, approximations, and numerical grids to simulate flow and transport and chemical reactions on the scales required by the EU guidelines. In order to investigate meteorological and chemical parameters on a spatial scale of $O(100 \text{ m}^2)$ in urban areas, the microscale model MITRAS is able to account for obstacles, such as buildings, explicitly.

Within M-SYS, results of the microscale meteorology model MITRAS need to be thoroughly evaluated before they can be used by the chemistry model MICTM to predict air quality at hot spot locations. Evaluation procedures have been proposed by VDI (2005) and European COST Action 732 (Britter and Schatzmann, 2007a; Franke et al., 2007; Britter and Schatzmann, 2007b). The procedure by VDI contains several steps for the comparison: As a first step it addresses the equations and approximations used in the model, and the documentation aspects. In the second step idealised test cases are to be calculated to test basic model properties, such as dependency on grid resolution and stationarity of the results. In a third step, model results are

4. EVALUATION OF SIMULATED WIND FIELDS

compared with high quality reference data from wind tunnel measurements. The procedure also contains requirements to be followed for every model application and outlines how to test the results of realistic model applications. This study presents the results of the comparison of MITRAS model results with idealised as well as realistic reference data according to the procedure described in VDI (2005). This procedure has previously been applied for the evaluation of other models, e. g. MISKAM (Eichhorn and Kniffka, 2010) and OpenFOAM (Franke et al., 2012).

An overview of the model MITRAS is given in Section 4.2.1. Section 4.2.2 outlines the method used for the comparison and results are presented in Sections 4.3 and 4.4 for simple and realistic test cases, respectively. Section 4.5 provides summary and outlook.

4.2 Method

4.2.1 Model description

MITRAS is a 3-dimensional, prognostic, microscale, numerical model for the prediction of flow and transport in the vicinity of obstacles, e. g. buildings. It has been developed based on the mesoscale model METRAS and they share many properties and program code. MITRAS calculates the flow field as well as potential temperature and humidity fields and can take into account effects of thermal stratification (Bohnenstengel et al., 2004). A major adjustment for the application within the obstacle layer is the explicit treatment of obstacles within the model domain. These not only affect the flow field, but can also incur shading effects and thermal effects of the building walls (Schlünzen et al., 2003a). Typical domain sizes range between several hundred metres and a few kilometres horizontally, with a domain height of a few hundred metres.

Equations

The model equations are based on the Navier–Stokes–equations, the continuity equation and the conservation equations for further scalar properties, e. g. potential temperature and humidity which are all solved in prognostic equations. The ideal gas law and the equations for the potential temperature are solved diagnostically. MITRAS is a non–hydrostatic model and employs the anelastic approximation and the Boussinesq–approximation. Two options are implemented for the Coriolis force: the Coriolis parameter is either assumed to be constant throughout the model area, or the Coriolis force can be neglected altogether.

Turbulence parameterisation

To limit the computational cost, MITRAS employs the Reynolds–Averaged–Navier–Stokes (RANS) equations. Two separate turbulence parameterisations are implemented in MITRAS to close the set of equations. The Prandtl–Kolmogorow–approach employed for this study parameterises the exchange coefficient using the turbulent kinetic energy (TKE) and a mixing length. This mixing length is derived from the distance to the closest surface, which can be either the bottom of the domain or any obstacle surface. The alternative approach parameterises the exchange coefficient using TKE and the dissipation. Details are given in Lopez et al. (2005).

Numerical grid

The equations are discretised using an Arakawa–C–grid, so that the vector grid points are staggered between the scalar grid points. To account for orographic effects in the model domain, the equations are solved on a non–cartesian, terrain following co–ordinate system. Instead of the cartesian vertical co–ordinate z , a vertical co–ordinate η is defined depending on the local orography height:

$$\eta = z_t \cdot \frac{z - z_s(x, y)}{z_t - z_s(x, y)} \quad (4.1)$$

where z_t denotes the height of the model top and $z_s(x, y)$ the orography height at location (x, y) .

A non-uniform grid can be used in horizontal and vertical directions. An area of high spatial resolution can be defined and a constant (but changeable) factor is used to increase the grid width from one point to the next up to a specified maximum. Typical grid widths have a minimum of 1 m in horizontal direction. The resolution is mainly limited by computing cost and the requirement that the lowest grid level has to be large compared to the local surface roughness. The maximum grid size used in relevant areas of the domain is a few metres.

Numerical stability

MITRAS solves the momentum equations using the Adams–Bashforth scheme in time and centred differences in space. This method has a low numerical diffusivity compared to other numerical schemes, but may lead to short wave energy accumulation as a numerical artefact which might eventually result in numerical instabilities. As a remedy, 3– 5– and 7–point filters are implemented in MITRAS to contain short waves. In urban areas with very complex obstacle configurations, this can lead to problems, as grid points used in the filter may be located within obstacles, while only grid points outside of buildings can be used by the filter. For this study an alternative filtering has therefore been implemented to artificially increase the value of the diffusivity: A theoretical diffusivity can be calculated for the upstream scheme, which has an implicit diffusivity that depends on the local wind speed $|\vec{v}|$, the local grid width Δx and the Courant number Co . According to Schlünzen (1996) the additional diffusivity K_{num} is

$$K_{num} = 0.5 \cdot |\vec{v}| \cdot \Delta x \cdot (1 - Co) \quad (4.2)$$

The Courant number describes the ratio of local windspeed $|\vec{v}|$, local grid width Δx and the current length of the time step Δt : $Co \approx |\vec{v}| \cdot \Delta t \cdot \Delta x^{-1}$. The locally calculated exchange coefficient is increased by the respective value calculated using Equation (4.2). This artificially increased diffusivity was employed throughout the model domain for the complex test cases, while for the idealised test cases the traditional filter could be used.

Treatment of obstacles

To consider the influence of buildings on the flow in the model domain, these are explicitly included in MITRAS. A three-dimensional building mask is used, in which each grid cell is classified as *building* or *no building*. This information is used explicitly in all model equations using a weighing factor $Vol(x, y, z)$. Vol becomes 0 within buildings and 1 outside of buildings. Hence the model equations only need to be multiplied by a the weighing factor. For any variable Ψ this is

$$\tilde{\Psi}(x, y, z) = \Psi(x, y, z) \cdot Vol(x, y, z) \quad (4.3)$$

For the wind field this equation essentially creates zero wind speed within buildings and at all building surfaces.

Model set-up for comparison with wind tunnel results

The calculated wind fields are compared with reference data from wind tunnel measurements. Data sets measured in a wind tunnel usually have certain limitations regarding the physical processes accounted for. These need to be considered in the set-up of numerical model runs. The following limitations are valid for all wind tunnel results used in this study, but not necessarily for wind tunnel results as such. The wind tunnel does not account for Coriolis force effects, thus the Coriolis force is neglected in the simulation. The available wind tunnel results are ensemble averages with neutral stratification, which should be comparable to RANS results. Therefore, no additional

4. EVALUATION OF SIMULATED WIND FIELDS

adjustments have to be made, but stationary solutions have to be calculated and any stability effects need to be neglected.

The wind tunnel measurements imply a constant, average wind field at the inflow boundary of the wind tunnel. To achieve a high comparability of the results, this effect is accounted for in the numerical model by applying fixed values at the inflow boundary for the incoming boundary normal wind component. The boundary parallel wind component is calculated using gradient-zero conditions to avoid the reflection of waves. To characterise the wind tunnel inflow profile a power law function

$$U(z) = U(z_{ref}) \cdot ((z + d_0)/(z_{ref} + d_0))^\alpha \quad (4.4)$$

can be fit to the measurements, where d_0 is the displacement height, α is the profile exponent and z_{ref} is a reference height. Inflow profiles for the numerical model have been prepared in a one dimensional model run over a surface roughness length z_0 without explicit consideration of buildings.

No orographic structure is considered for the test cases.

4.2.2 Evaluation method

Good reference data for the comparison with numerical model data are a substantial prerequisite for model evaluation. This could be data measured in field experiments or in wind tunnels (physical models). In this study, preference has been given to physical model results, because they offer a much finer spatial resolution than feasible in field experiments. Also, wind tunnel results have a higher reproducibility since the boundary conditions (wind velocity in particular) are well defined, whilst in field experiments the boundary conditions vary between experiments or even during one experiment depending on the actual weather conditions. However, it has to be kept in mind that numerical model and wind tunnel model both represent a model of the real atmosphere, each with their individual approximations and shortcomings that might lead to differences in the comparison, thus it may be difficult to decide if these are actual shortcomings of the numerical

model.

The evaluation of the simulated wind fields is based on a point-by-point comparison of numerical model results with wind tunnel data. Point measurements of the individual wind components are carried out on a sampling grid mostly in a regular distribution within a horizontal or vertical plane. In general, the numerical model uses a different grid, so that the numerical model results are not located at the same points. They are then interpolated onto the measurement grid using tri-linear interpolation.

The evaluation of the comparison is carried out in analogy to VDI (2005) using hit-rates. A hit-rate represents the relative fraction of values that do not exceed an allowed deviation from the comparison data. Two different allowed deviations are used at the same time: An absolute deviation W and a relative deviation D , so that the hit-rate q can be defined as

$$q = \frac{N}{n} = \frac{1}{n} \cdot \sum_{i=1}^n N_i \quad (4.5)$$

with

$$N_i = \begin{cases} 1 & \text{if } \left| \frac{P_i - O_i}{O_i} \right| \leq D \vee |P_i - O_i| \leq W \\ 0 & \text{else} \end{cases}$$

and

- N – Number of data points counted as *Hit*
- n – Total number of wind speed values to be compared
- O_i – comparison data at location i
- P_i – model result at location i

The hit-rate is determined separately for each test case and each wind com-

ponent. With a hit-rate of $q \geq 2/3$ for each wind component a test case is successfully passed. The hit rates are calculated for all available data points as well as only for the data close to the obstacles (near field). Actual values for the allowed deviations W and D are defined for each test case individually (VDI, 2005). They account for the quality of the reference data set and the differences induced by the comparison itself, e. g. linear interpolation in areas with non-linear gradients of the compared values or the different approximations of complex obstacles in the numerical model and in the physical model.

4.3 Idealised test cases

For a comparison with idealised test cases, the cases from group C of VDI (2005), which are based on datasets from the CEDVAL database (CEDVAL, 2013) have been used. These tests are performed to evaluate general physical properties of the model. Their configuration has therefore been kept simple, analysing mainly the flow around individual obstacles.

4.3.1 Selected test cases

For cases $C1$ and $C2$, a quasi-2-dimensional domain with one beam across the full width of the domain has been set up. The beam has a square cross section with height and width of 25 m. The approaching flow is perpendicular to the front of the beam. The domain for cases $C3$ and $C4$ contains one isolated cubic obstacle with height, width and length of 25 m. For case $C3$ the approaching flow direction is perpendicular to one front of the cube, for case $C4$ the approaching flow is perpendicular to one edge of the cube. Case $C5$ includes one cuboidal obstacle with dimensions height=25 m, width=30 m, length=20 m and the approaching flow perpendicular to the wider front of the obstacle. 21 obstacles of the same size and shape are used in case $C6$, aligned in a grid of 3 by 7 obstacles (in lateral and longitudinal direction, respectively) in an equidistant array. The direction of the approaching flow in this case is again perpendicular to the larger front of the obstacles.

4. EVALUATION OF SIMULATED WIND FIELDS

Test case	Obstacle Shape	Compared Quantity
<i>C1</i>	Beam	Velocity vector (u,w) and Length of the recirculation zone
<i>C2</i>	Beam	Length of the recirculation zone
<i>C3</i>	Cube	Velocity vector (u,v,w)
<i>C4</i>	Cube	Velocity vector (u,v,w)
<i>C5</i>	Cuboid	Velocity vector (u,v,w)
<i>C6</i>	Group of cuboids	Velocity vector (u,v,w)

Table 4.1: Properties of the idealised test cases. The length of the recirculation zone is measured from the downstream edge of the obstacle and describes the distance to the point downstream of the centre of the obstacle, where the wind component parallel to the approaching flow vanishes (VDI, 2005).

The inflow profiles for the wind tunnel measurements are characterised by a power law function (Equation 4.4) with $d_0 = 0$ for all cases and $\alpha = 0.23$ (*C1*), $\alpha = 0.22$ (*C3*), $\alpha = 0.21$ (*C4*, *C5*, *C6*). Inflow profiles for the numerical model have been prepared with surface roughness lengths prescribed by VDI (2005): $z_0 = 0.10$ (*C1*, *C4*, *C5*, *C6*) and $z_0 = 0.03$ (*C2*).

All domains have been set up using a cartesian grid with a grid spacing of $\Delta x = \Delta y = \Delta z = 2.5$ m at and near the obstacles, and increasing with a factor of 1.2 per grid cell towards the domain boundaries.

The comparison of results has been carried out for *all* available data points as well as for the area *near* the obstacle, where the direct influence of the obstacle is greatest and the prediction of an accurate wind field is generally more challenging. This near field is defined: from $1.0 H$ ($H =$ building height) (cases *C1,C2*: $1.5 H$) upstream up to $2.0 H$ (cases *C1,C2*: $7.5 H$) downstream of the building and from the ground up to $1.5 H$ height. For cases *C3,C4,C5,C6* the near field includes $0.5 H$ on both sides of the building in lateral direction. An overview of the test cases and the quantities to be compared is given in Table 4.1.

4.3.2 Results for idealised test cases

Results for the length of the recirculation zone in cases *C1* and *C2* are within the required range for both cases as shown in Table 4.2. All hit rates for

4. EVALUATION OF SIMULATED WIND FIELDS

Test case	$C1$	$C2$
required length for L	100 – 125 m	$> L_{c1}$
model result for L	≈ 100 m	≈ 125 m
meets requirement	yes	yes

Table 4.2: Length of recirculation zone (L) for all idealised test cases.

Test case			$C1$	$C3$	$C4$	$C5$	$C6$
hit rate	(u)	all	75%	89%	86%	92%	83%
hit rate	(u)	near	45%	81%	n.d.	86%	79%
hit rate	(v)	all	n.d.	96%	78%	91%	86%
hit rate	(v)	near	n.d.	93%	n.d.	85%	86%
hit rate	(w)	all	68%	74%	76%	87%	89%
hit rate	(w)	near	69%	64%	n.d.	79%	85%

Table 4.3: Hit rates for all idealised test cases; for all available reference measurements (all) and for all reference measurements within the near field of the obstacle (near). (n.d.: no comparison data available)

idealised test cases are summarised in Table 4.3. They consistently show hit rates above the threshold value of $q = 2/3$ if all available reference points are considered. If the evaluated area is limited to the near field around the obstacle for a more thorough evaluation, the hit rate for the vertical wind component reaches the threshold value in all cases except $C3$. The horizontal wind component clearly misses the threshold value in case $C1$, but is well simulated in all other cases. For the latter comparison, also the vertical wind component only marginally reaches the threshold value while the length of the recirculation zone is at the lower boundary of the required range.

Scatter plots of numerical model result and wind tunnel data are shown in Figures 4.1 and 4.2 for all idealised test cases.

Case $C1$ Figure 4.1 (left plot) confirms the problematic hit-rate for the near field of the u -component in case $C1$. At some locations the numerical model result shows higher wind speeds where the reference data shows low or near-zero wind speeds. The right plot of the figure shows an underestimation of the highest vertical wind speeds by the numerical model compared to the reference data. For the flow across a beam, low wind horizontal wind speeds

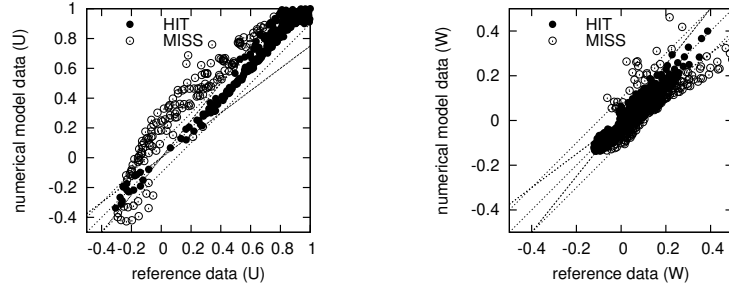


Figure 4.1: Scatter plot of normalised wind speed components for case *C1*. Filled and outlined circles indicate *Hit* and *Miss* at all available data points. Dotted lines show the bisecting line, and the allowed relative deviation D and absolute deviation W .

occur in the downward branch of the recirculation zone (as well as very near the surfaces). If the length of the recirculation vortex differs slightly between two data sets differences with some magnitude can occur easily. Figure 4.3 shows *Hit* and *Miss* for case *C1* for both wind components at all available points. *Hit* and *Miss* are indicated by filled and outlined circles, respectively. Arrows indicate the difference vector between model and wind tunnel result. It can be seen that for most points there is good agreement between the results for both or one of the wind components. In the near field directly behind the obstacle the agreement for the horizontal wind component and above the obstacle for the vertical wind component are not as good. The difference vectors indicate a stronger but shorter recirculation zone in the numerical model result, which confirms the data in Table 4.2, where the recirculation zone is at the lower end of the allowed range.

Case C3 Figure 4.2(a) (right plot) shows a scatter plot of the w -component for which the hit-rate is just below the required threshold. The plot indicates a positive bias of the numerical model compared to the wind tunnel data for a fraction of the data points. Figures 4.4 and 4.5 show *Hit* and *Miss* for case *C3* for both respective wind components at all available points. Most points again show a very good agreement between model and wind tunnel results. Similar to case *C1*, a slight underestimation of the flow above the obstacle can be seen, leading to some *Miss* points in the near field. However, Figure 4.5 shows that the horizontal wind field is overall very well represented.

4. EVALUATION OF SIMULATED WIND FIELDS

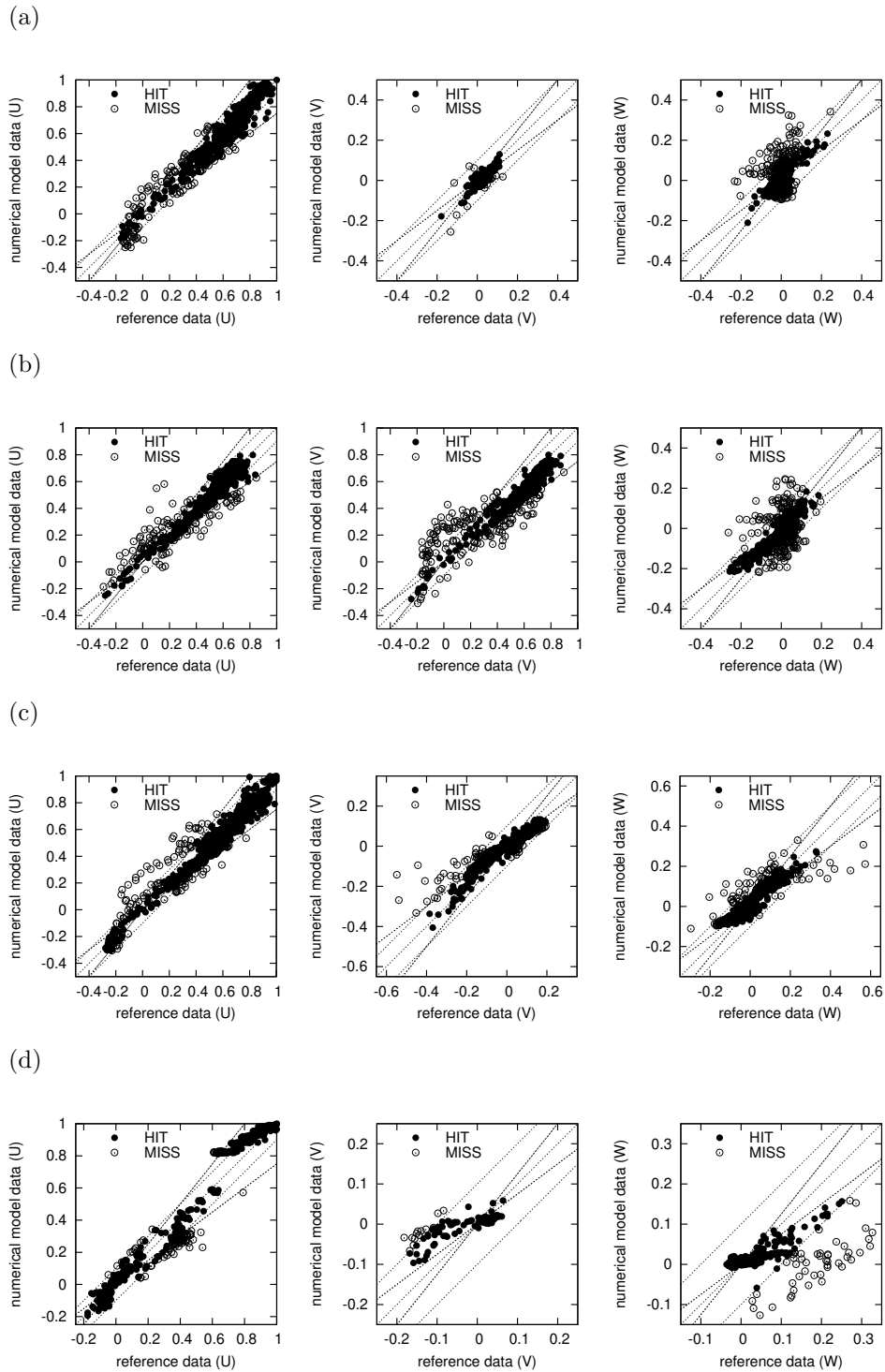


Figure 4.2: Scatter plot of normalised wind speed components for cases (a) $C3$, (b) $C4$, (c) $C5$, (d) $C6$. For explanation see Figure 4.1.

4. EVALUATION OF SIMULATED WIND FIELDS

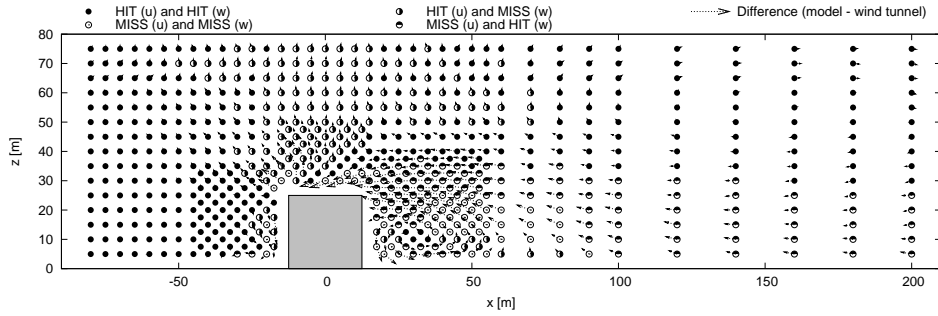


Figure 4.3: Result for case $C1$. Filled and outlined circles indicate *Hit* and *Miss* for both wind components at all available data points. Arrows indicate the difference vector between model result and wind tunnel results $\vec{v}_{diff} = \vec{v}_{model} - \vec{v}_{windtunnel}$.

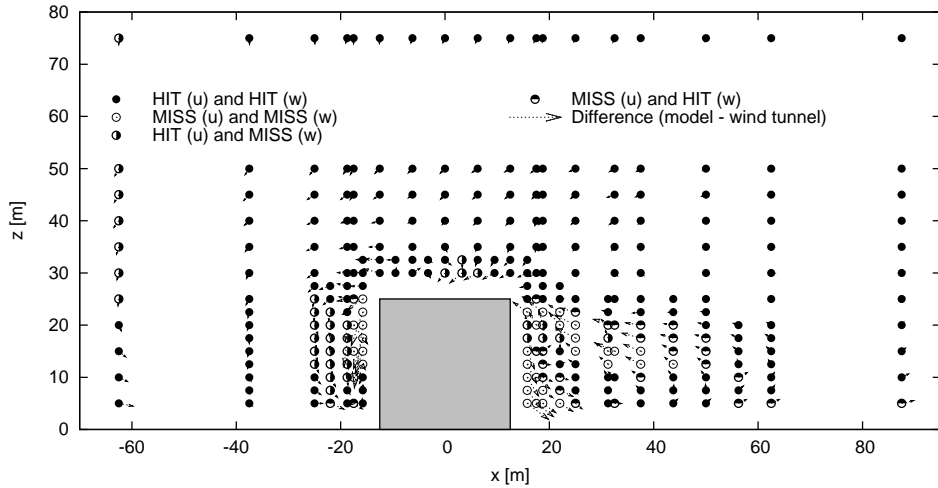


Figure 4.4: Result for case $C3$ (vertical cross section). For explanation see Figure 4.3.

Although hit-rates are comfortably above the threshold for all other cases, their scatter plots reveal some more noticeable features:

Case $C4$ Figure 4.2(b) shows case $C4$ with an approach flow perpendicular to a corner of the cube. For the v -component (middle plot) a positive bias can be found for the numerical model result at some locations where the reference data shows very low wind speeds.

4. EVALUATION OF SIMULATED WIND FIELDS

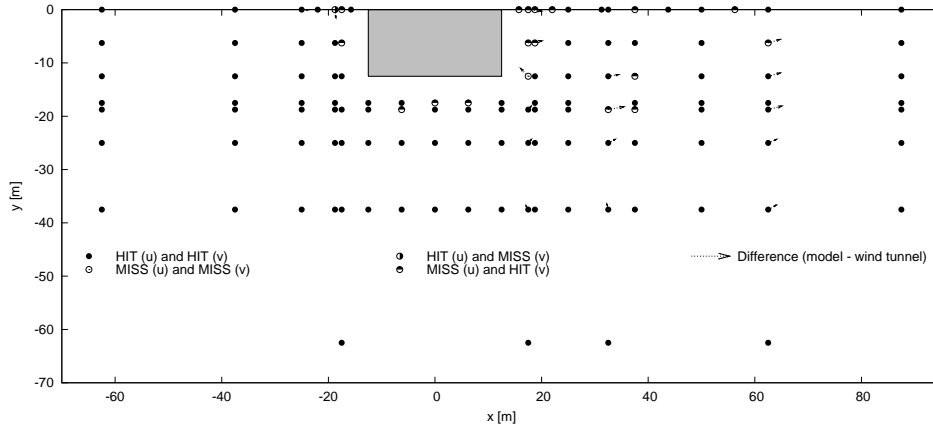


Figure 4.5: Result for case *C3* (horizontal cross section). For explanation see Figure 4.3.

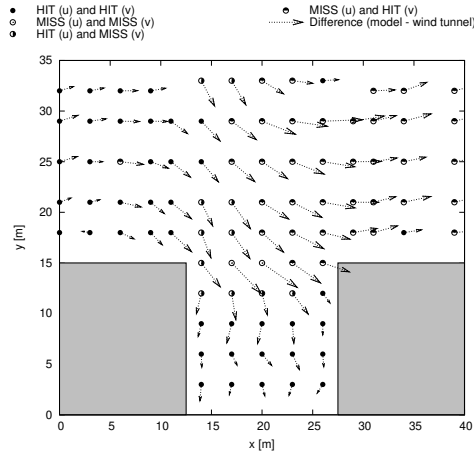


Figure 4.6: Result for case *C6* (horizontal cross section). For explanation see Figure 4.3.

Case *C6* For case *C6*, Figure 4.2(d) (right plot) shows the w -component for the array of cuboids. Here, a negative bias of the numerical model compared to the reference data can be found for some points. Figures 4.6 and 4.7 show the spatial distribution of *Hit* and *Miss* in horizontal and vertical cross sections, respectively. Figure 4.7 shows that the vertical wind speeds agree very well across most of the canyon between the obstacles (Figures 4.6(a)–(c)) while only Figure 4.6(d) shows reduced vertical wind speeds compared to the reference data. Figure 4.6 shows a reduced lateral flow into the canyon between two obstacles in the numerical model result. This is matched by the reduced vertical flow out of the canyon very near the canyon entrance,

4. EVALUATION OF SIMULATED WIND FIELDS

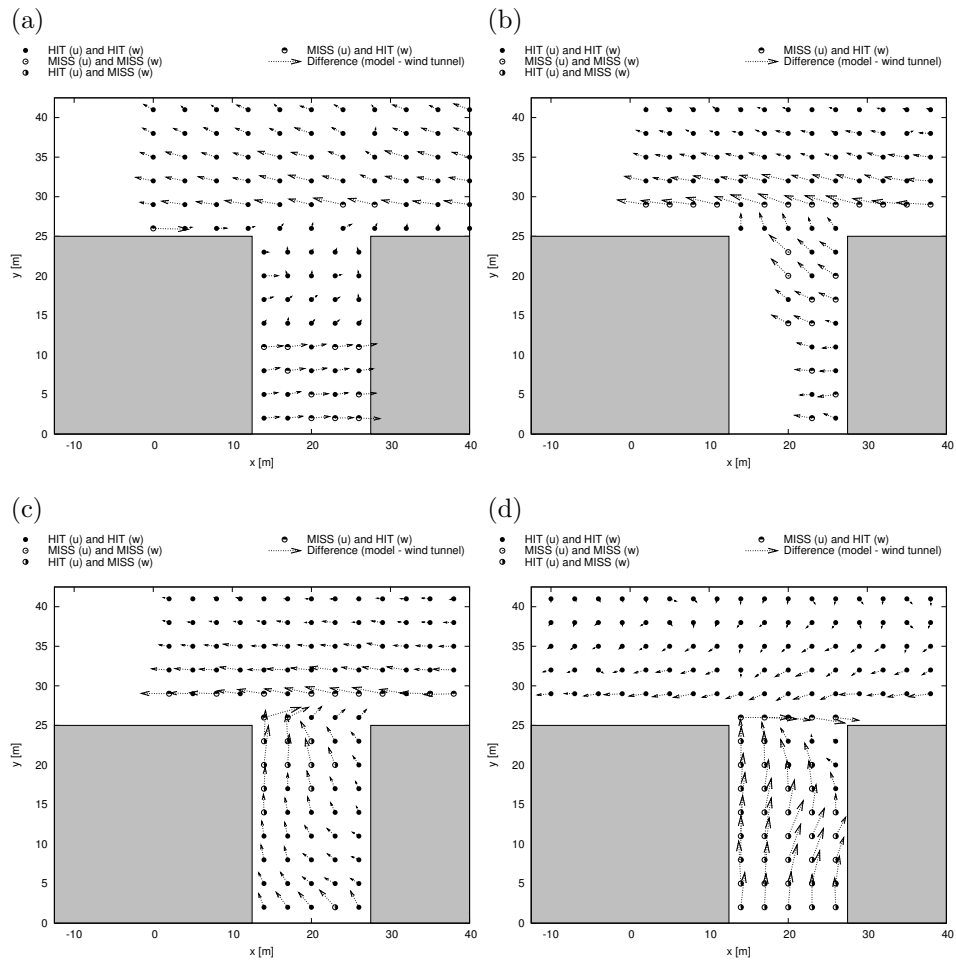


Figure 4.7: Result for case *C6* (vertical cross section) at (a) $y = -25$ m, (b) $y = -15$ m, (c) $y = -10$ m, (d) $y = 0$ m. For explanation see Figure 4.3.

leading to the vertical wind speed outliers observed in Figure 4.1(d). At a further lateral distance between the obstacles (Figures 4.6(a)–(c)) the effect of the reduced inflow fades and the vertical wind speeds agree very well.

4.4 Realistic test case

In addition to the comparison with reference data for idealised test cases, a comparison has been conducted for more realistic cases. The comparison was carried out for an area extending $1 \times 1 \text{ km}^2$ around Göttinger Straße in Hannover. Reference data are available for three directions of the approaching flow, each data set covers two heights above ground.

4.4.1 Study area Göttinger Straße

Göttinger Straße is a highly frequented arterial road with approximately 30'000 vehicles passing through per day (Schatzmann et al., 2005). Within the closely studied section of Göttinger Straße, buildings of approximately 25 m height are located on both sides of the street. With an average street width of 25 m, a street canyon with aspect ratio of canyon height to canyon width approximately 1 is formed. The street canyon axis is oriented towards NNE (17° against North), thus the simulation domain is rotated westward against the north–south–axis to align the main canyon with the computational grid (Figure 4.8). The two canyon sides will be denoted ‘westward’ and ‘eastward’ in the following. On the westward side, the buildings form a contiguous canyon wall of 110 m length, while on the eastward side, three residential side streets intersect the canyon. The study area is dominated by industrial buildings with flat roofs and open spaces to the West and South–West of the street canyon, and by residential blocks of buildings with courtyards and side streets to the East. Northward the street canyon leads into the large roundabout Deisterplatz, an open area with grass and trees. Southward the street canyon widens, so that the street can geometrically no longer be defined as a canyon.

Göttinger Straße has been subject to air quality research for several years. Continuous measurements of wind velocity and several trace gas concentrations are carried out within the street canyon as well as above roof level (Müller et al., 2002; NLÖ and FZK, 2004). Traffic counters are fitted for each traffic lane separately. During the project VALIUM (Schatzmann et al., 2005)

these measurements were supplemented by additional long- and short-term measurements within the street canyon, above roof level and in the surrounding area.

The study area has little orographic structure and no steep slopes. A small rise of the terrain height can be found from east to west in the study area and the highest elevation is the Lindener Berg, which is 25 m higher than the street canyon and located some 500 m north-west. The terrain height rises by an average of 2% and no more than 10% at any location in the domain.

4.4.2 Model domain Göttinger Straße

The set-up for both, numerical and wind tunnel model has been coordinated as much as possible to ensure a good comparability of the results. The building heights were matched between physical and numerical model, although the physical model represents some small scale features, e. g. bays and dormers, and uses different roof shapes, while in the numerical model an average roof height was used. The domain represented in the numerical model covers an area of $1 \times 1 \text{ km}^2$, centered around the street canyon of Göttinger Straße and extends up to a level of 420 m height above ground in the vertical direction. The orography is neglected to be comparable with wind tunnel data.

A non-uniform model grid has been used. The coordinate system has been aligned parallel to the main axis along the street canyon of Göttinger Straße to minimise numerical artefacts in the focus area due to the grid. The horizontal resolution is 1.5 m within an area of $42 \times 42 \text{ m}^2$ in the core of Göttinger Straße. In the surrounding area the grid width increases by a factor of 1.1 up to a maximum of 15 m towards the lateral boundaries of the domain. In vertical direction the grid width is 1.5 m near the ground up to a level of 25 m above ground. This corresponds to the average roof level of buildings within the domain. Aloft the grid width increases by a factor of 1.1 per grid level up to a magnitude of 30 m at the model top. Thus the number of grid cells totals to 150×156 cells and 47 levels $\approx 1.1 \cdot 10^6$ cells. This numerical grid realises a high resolution in the core area of the investigation, while influence from

4. EVALUATION OF SIMULATED WIND FIELDS

more distant locations can be included with a limited increase in numerical effort.

The building geometries within the model domain are derived from the cadastral map *Stadtkarte Hannover** in a scale of 1 : 1000. This high resolution ensures that the digitalisation error for the position of the buildings is lower than the grid resolution at any location of the domain. In principle merely the number of floors for each building was available to estimate the building height. Depending on the type of each building a height of 3.0 m or 3.5 m was assumed per level to obtain the building height. The results were corrected with data from additional sources — two previous wind tunnel models and known heights for individual buildings — for the domain core. The main building on the westward side of the street–canyon includes some gateways and a covered footpath. MITRAS’ option to include elevated obstacles has been employed to represent these features in the numerical grid. In total 400 individual obstacles are included in the domain. The domain size and obstacle representation in the numerical grid are shown in Figure 4.8.

4.4.3 Comparison data set

Measurements taken in the boundary layer wind tunnel *WOTAN* at the University of Hamburg have been used as reference data. The wind tunnel model was set–up in spatial scale of 1 : 250 and comprised of a main disc with 1 km diameter that could be extended to a square of $1 \times 1\text{km}^2$ area for selected wind directions. Building locations were taken from the ‘Stadtkarte Hannover’ in scale 1 : 1000.

For the comparison data set, a measurement grid of 300 points has been defined within the main street canyon and its direct vicinity. For three inflow directions measurements at two heights were taken for the horizontal wind components. Vertical winds were not measured. Inflow directions were set to 220° , 260° and 270° (Table 4.4). Preliminary studies (Pascheke, 2013) have shown that the flow features within the street canyon change significantly

*Landeshauptstadt Hannover, Geoinformation, Kartenvertrieb, Rudolf–Hillebrecht–Platz 1, 30159 Hannover, Germany

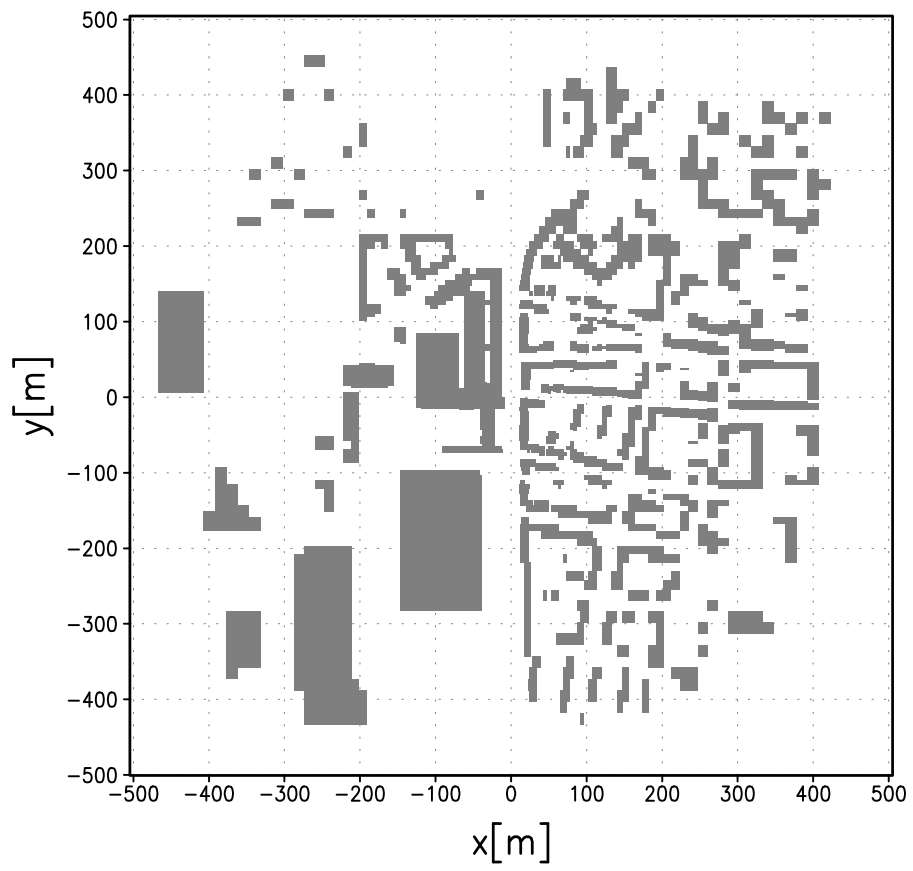


Figure 4.8: Obstacle representation in the numerical grid (plan view).

4. EVALUATION OF SIMULATED WIND FIELDS

Test case	220-10	220-03	260-10	260-03	270-10	270-03
Main wind direction	220°	220°	260°	260°	270°	270°
measurement height	10 m	3 m	10 m	3 m	10 m	3 m
measured variables	u, v					

Table 4.4: Test cases and their attributes of the comparison cases for Göttinger Straße

between the inflow directions 260° and 270°. These directions have therefore been selected to provide a rigorous test of the numerical model performance. 220° has been selected because it represents the prevailing wind direction for this domain and hence an important case for further studies of this domain, e. g. tracer dispersion (Grawe and Schlünzen, 2019).

4.4.4 Transfer of the evaluation method to realistic test cases

For idealised test cases, the set-up of the numerical model can be chosen in such a way that optimal comparability with the reference data set can be ensured. This is not always the case for realistic cases, where the numerical model set-up may be optimised for the application to a real situation rather than optimising the model set-up solely for the comparison with reference data. This includes but is not limited to parameters such as building geometry, orographic structure, inflow wind profile and Coriolis force calculation. For this study, MITRAS has been set-up to best represent the real conditions, while modifications were made to some settings to account for specifics of the wind tunnel if the effect was deemed minor. Specifically, this leads to different wind speeds being used in both models (whereas in the idealised test cases the wind speed prescribed by the comparison data set would be used). In order to calculate hit-rates, extra care needs to be taken to account for the different wind speeds. Following e. g. Panskus (2000), the modelled wind speeds can be compared using a transfer function to calculate non-dimensionalised, normalised data.

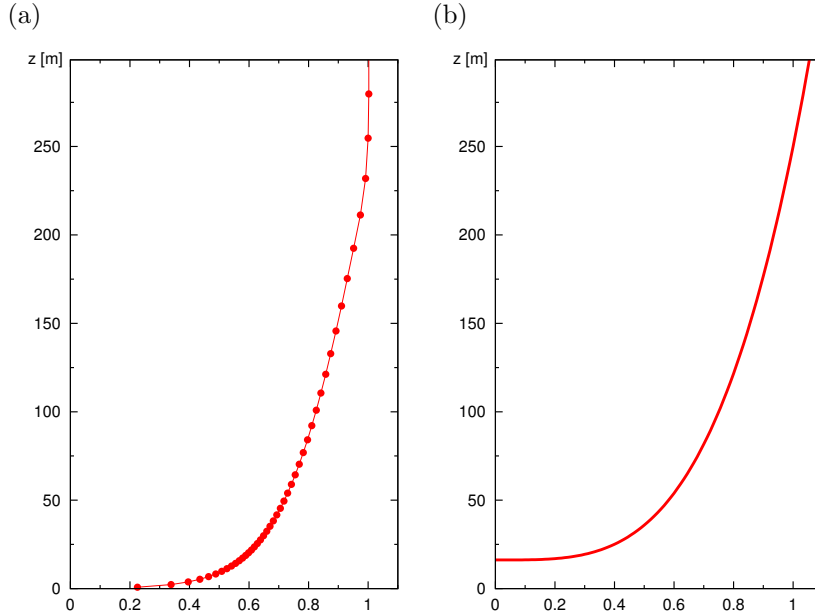


Figure 4.9: Vertical profile of the undisturbed flow at the inflow boundary. (a) For the numerical model the wind speed at the actual grid points is shown; (b) for the wind tunnel data [†] the graph shows a profile corresponding to the parameters $\alpha = 0.29$ and $d_0 = 16$ m which have been derived from the measurements. Both graphs have been normalised so that $|\vec{v}|(z = 250 \text{ m}) = 1.0 \text{ m/s}$.

$$U_{norm} = \frac{U(x, y, z)}{U(ref)} \quad (4.6)$$

where $U(x, y, z)$ is the wind speed at location x, y, z and $U(ref)$ is a reference wind speed, for numerical model result and wind tunnel data, respectively.

The selection of the specific reference wind speed is critical for the comparison, since it affects the magnitude of every compared value. It needs to be unaffected by the local vertical wind profile and especially unaffected by the building configuration. An obvious choice could be the wind profile at an inflow boundary in sufficient distance to the obstacles. Figure 4.9 shows such profiles for Göttinger Straße. For the numerical model, a profile of the boundary values at the inflow boundary can be used, in the wind tunnel, a vertical wind profile has been measured upstream of the build-up area.

4. EVALUATION OF SIMULATED WIND FIELDS

The inflow profile used in the numerical model has been prepared in a one-dimensional numerical model run without explicit consideration of buildings. The roughness length assumed for the model domain needs to account for obstacle and roughness effects that are not explicitly resolved by the model. The area upwind of the domain for the main wind direction (south-west) is dominated by railway grounds, some industrial buildings sparse vegetation and open spaces. Therefore, a surface roughness of $z_0 = 0.1$ m has been assumed; according to Stull (1988) a roughness length of this magnitude is representative of an area with mainly vegetation (hedges and trees) and few buildings. The upwind areas for easterly or northerly wind conditions contain mainly residential buildings for which a slightly higher surface roughness should be assumed. The local roughness length needs to be small compared to the height of the lowest grid level above ground in order to avoid numerical instability. Hence, the vertical grid resolution of 1.5 m creates an upper limit for the roughness length, while all obstacles that would contribute to a higher roughness length need to be explicitly included. This is not possible for the area upwind of the domain, therefore a larger domain size has been chosen to allow a distance of up to 500 m upstream of the analysed area for the flow field to adjust.

The inflow profile used in the wind tunnel model has been prepared using turbulence generators and artificial roughness elements over a distance of approximately 14 m upstream, so that the resulting wind and turbulence profile is representative of an urban area (Pascheke, 2013). Fitting the power law function (Equation 4.4) to the measured data, the profile is described by the profile exponent $\alpha = 0.29$ and the displacement height $d_0 = 16$ m.

As can be seen from Figure 4.9, the two different approaches (although consistent with the test case and with the respective model technique) lead to slightly different shapes of the vertical wind profiles, especially very near the ground due to the displacement height d_0 in the wind tunnel data. Normalisation with these profiles would therefore impose unrealistic differences for a comparison of results very near the ground. For the current test cases, the average magnitude of all compared wind velocities at each vertical plane has therefore been used to normalise the wind data. With this normalisation, the

comparison yields information about the wind direction as well as the relative wind speeds within each respective level, but cannot take into account the overall magnitude of the wind speed at a certain level.

4.4.5 Results for realistic test cases

The complex flow patterns developing in the obstacle layer of an urban area can be seen in horizontal cross sections in Figure 4.10 for 220° against North (237° against the main street axis; that is, from bottom left in the figure) at $z = 3\text{ m}$ and $z = 10\text{ m}$, respectively. The wind direction of the approach flow for these cases is 220° . This is near the main wind direction for the area (NLÖ and FZK, 2004). The cross sections are below the height of the buildings forming the main street canyon (aligned in North–South direction in the middle of the figure). A strong channeling effect can therefore be seen at both heights with a large canyon–parallel wind component. Only in the bottom layer a significant lateral wind component can be seen. This canyon–vortex with superimposed mean wind leads to a helix shaped wind direction and was also described in other domains (e. g. by Tomlin et al. (2009)). Very low wind speeds can be observed at the lower level of the narrow courtyards between the residential buildings (mostly in the right part of the domain) and in some instances also in the upper layer. Both of these effects may lead to the aggregation of pollutants in an urban area and should therefore be reproduced well by the numerical model in order to be applied for air quality studies. There are also some noticeable differences between the flow fields at both vertical levels: E. g. airflow through a diagonal street canyon can be seen in the top left of the sketch. The flow continues in the upper layer onto an open space. However, in the lower level, this flow is almost perpendicular. Figures 4.11 and 4.12 show horizontal cross sections of the flow fields for 260° and 270° (that is, from the left of the figure) at the same heights as in Figure 4.10. The flow is therefore in both cases nearly perpendicular to the main street canyon. In the calculated flow fields occurs an inflow into the main street canyon from both directions, so that a convergence point can be found somewhere along the canyon. Despite the very small difference in the approach flow direction, the stagnation point is shifted by some 60 m

4. EVALUATION OF SIMULATED WIND FIELDS

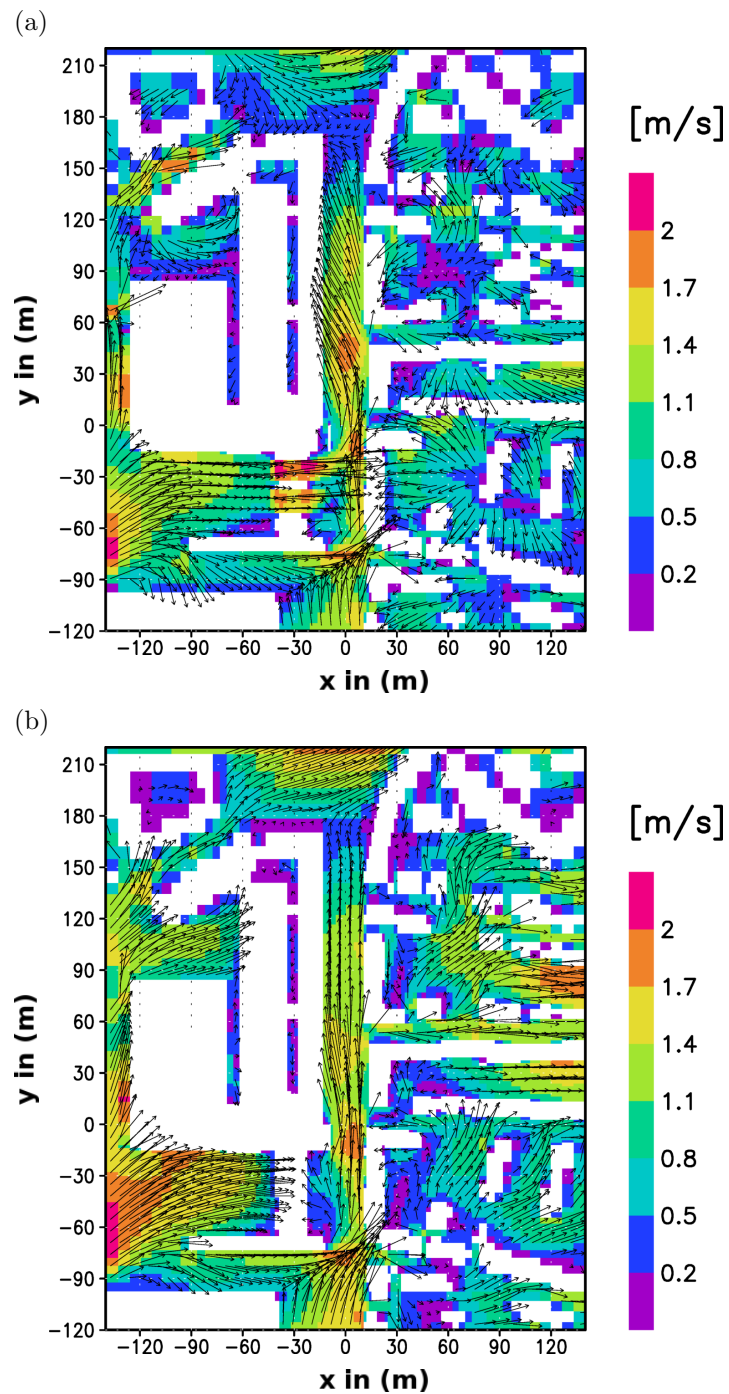


Figure 4.10: Wind field for cases (a) *220-03* and (b) *220-10*. Arrows show the horizontal wind velocity, shading shows the horizontal wind speed. Buildings are shown in white.

4. EVALUATION OF SIMULATED WIND FIELDS

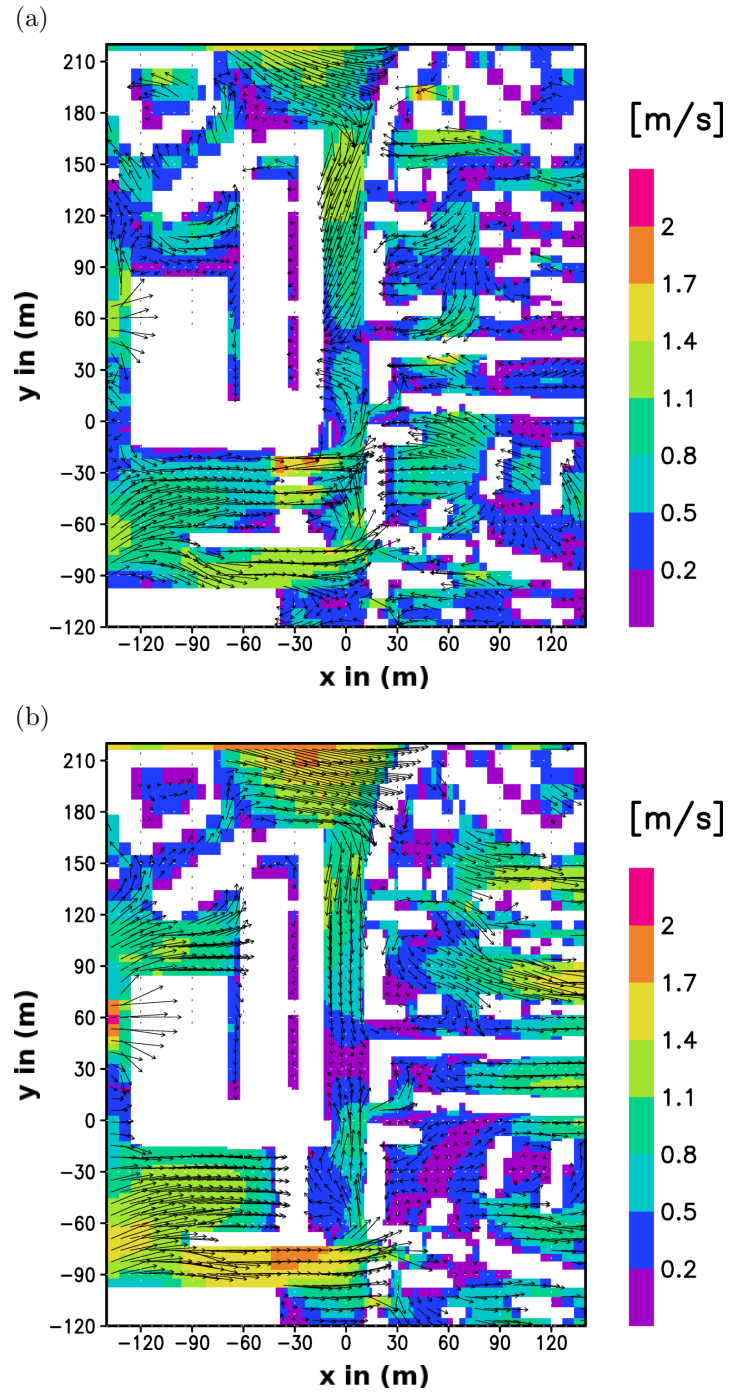


Figure 4.11: Wind field for cases (a) *260-03* and (b) *260-10*. For description see Figure 4.10.

4. EVALUATION OF SIMULATED WIND FIELDS

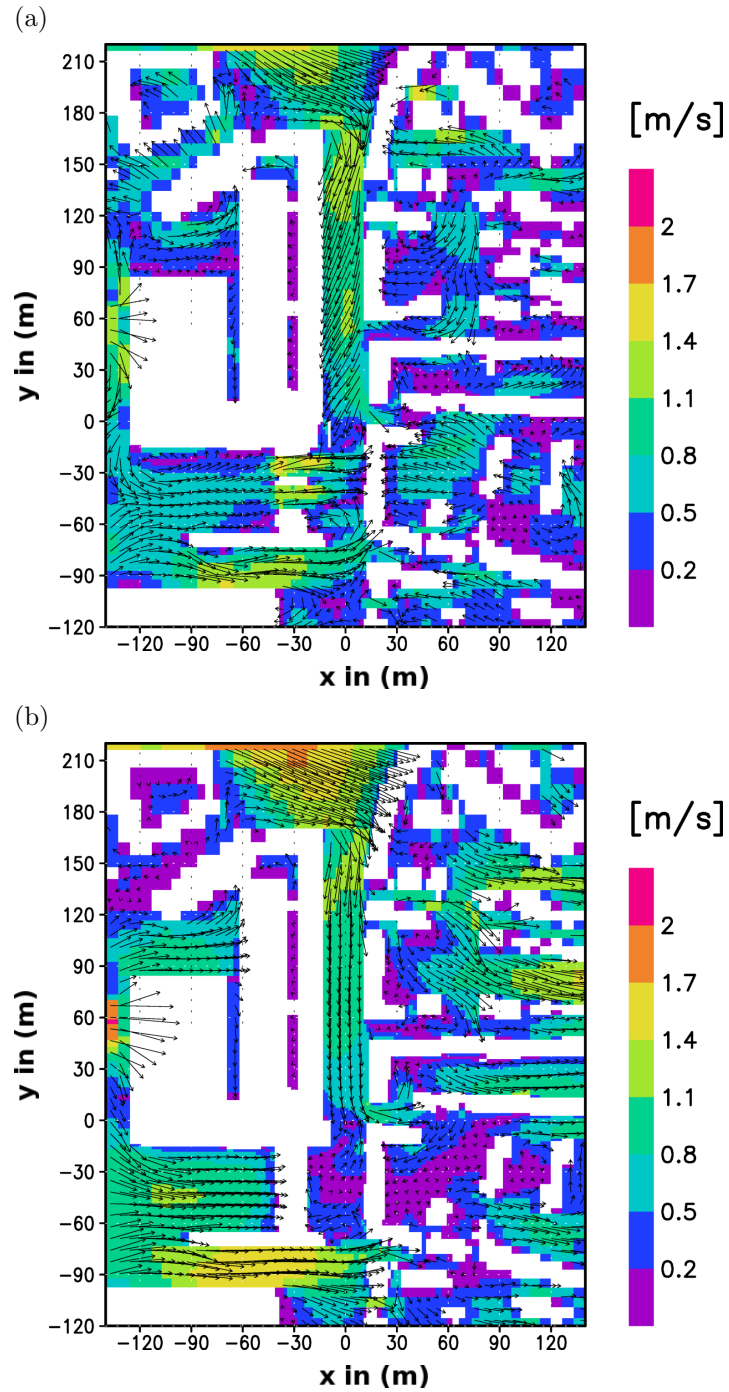


Figure 4.12: Wind field for cases (a) 270-03 and (b) 270-10. For description see Figure 4.10.

4. EVALUATION OF SIMULATED WIND FIELDS

Test case	220-03	220-10	260-03	260-10	270-03	270-10
Hit-rate (u)	61%	62%	70%	72%	78%	84%
Hit-rate (v)	52%	71%	66%	66%	94%	84%
Hit-rate (<i>windspeed</i>)	55%	74%	69%	77%	87%	87%

Table 4.5: Hit-rates for all test cases of Göttinger Straße

at the lower and some 80 m at the upper cross section. At such convergence points, reduced wind speeds may cause high tracer concentrations in an urban area. The position of this point is therefore important from an air quality perspective. The notable difference in the flow field due to a very small difference in the approach flow conditions makes these two cases a vigorous test case for a numerical model before the application for air quality problems.

The hit-rates for all realistic test cases are summarised in Table 4.5. For most cases, the hit-rates reach or exceed the threshold of $2/3$ (Section 4.2.2) for both wind components. For case *220*, the u -components fail to reach the threshold while only for *220-03* the v -component has a very low hit-rate. Also shown are hit-rates similarly calculated for the (horizontal) wind speed. For all cases at $z = 10$ m, the model performance for the wind speed is better than for both individual components. This is not the case for all cases at $z = 3$ m. This may imply that at the lower level the wind speed causes *Miss* values, while at the upper level the wind direction has some effect on the *Miss* values. The performance is consistently best for case *270*.

Figures 4.13, 4.14 and 4.15 show scatter plots for all realistic test cases *220*, *260* and *270*, respectively. In all plots few randomly scattered *Miss* points can be found. However, for the u -components in case *220* (Figure 4.13, left panel) more *Miss* points can be found with a positive bias of the numerical model compared to the wind tunnel data, hence the model overpredicts at most *Miss* locations. In Figure 4.13(a) (right panel), the v -component of the numerical model results shows a marked cluster of a high number of slightly overestimated values which appears to be the main reason for the low hit-rate in this case.

Figures 4.16, 4.17 and 4.18 show the locations of the *Hit* and *Miss* points for all cases. It can be seen in Figure 4.16 that for *220* the highest number of *Miss*

4. EVALUATION OF SIMULATED WIND FIELDS

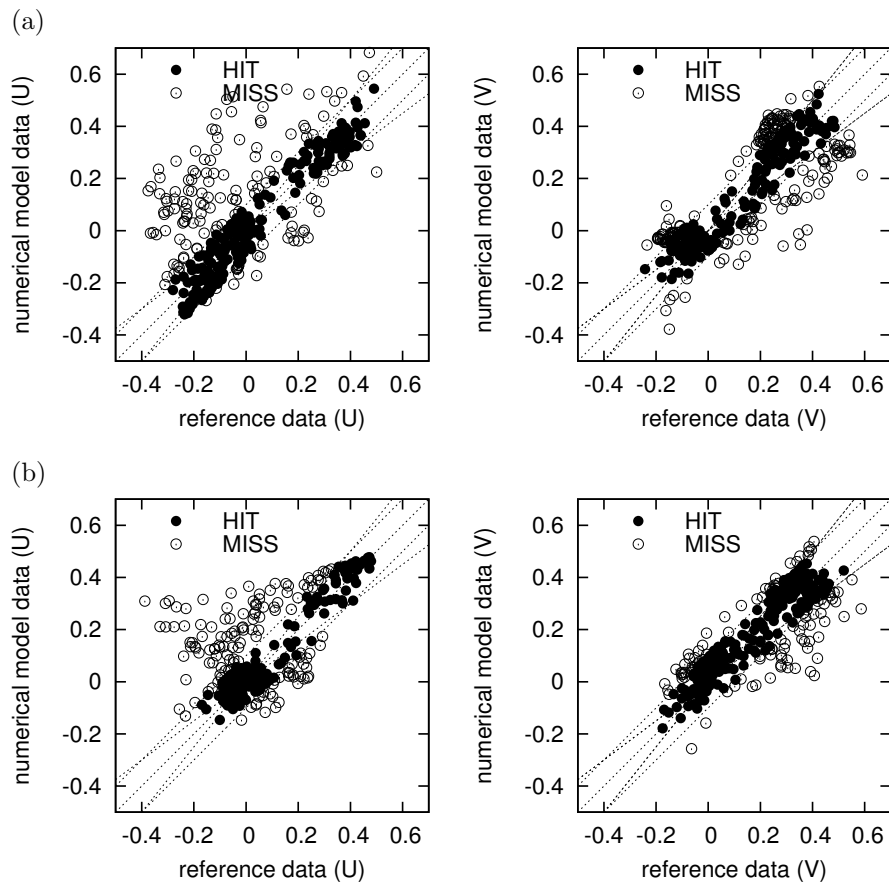


Figure 4.13: Scatter plot of normalised wind speed components for all cases (a) 220-03, (b) 220-10. Filled and outlined circles indicate *Hit* and *Miss* at all available data points. Dotted lines show the bisecting line, and the allowed relative deviation D and absolute deviation W .

4. EVALUATION OF SIMULATED WIND FIELDS

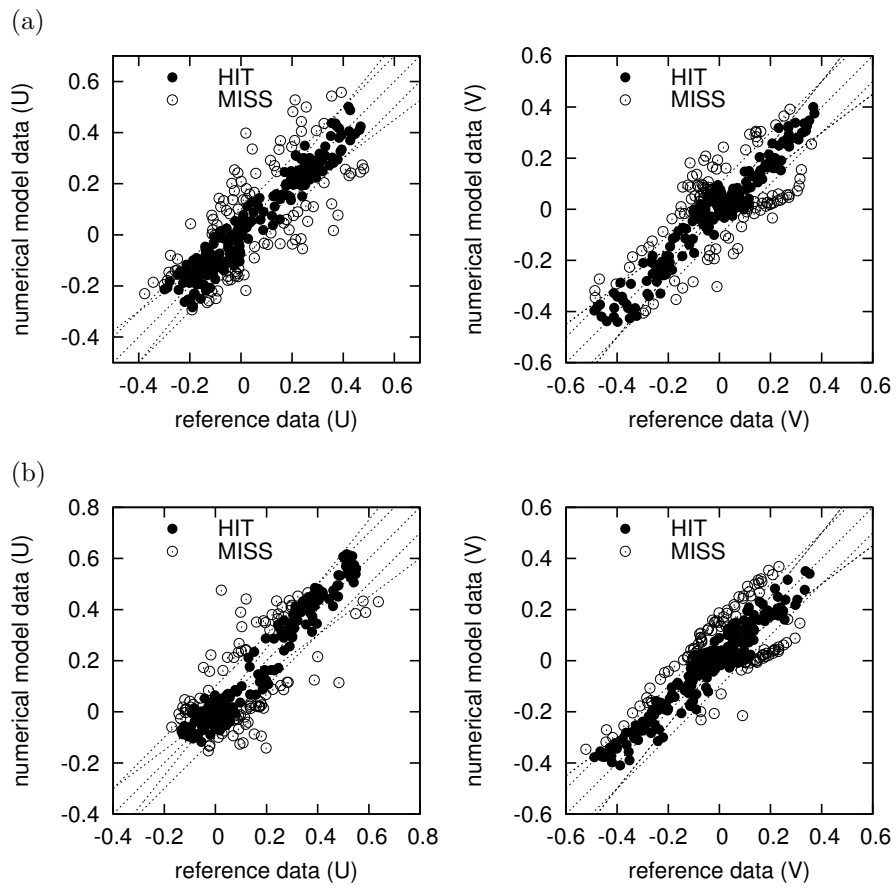


Figure 4.14: Scatter plot of normalised wind speed components for all cases (a) *260-03*, (b) *260-10*. For explanation see Figure 4.13.

4. EVALUATION OF SIMULATED WIND FIELDS

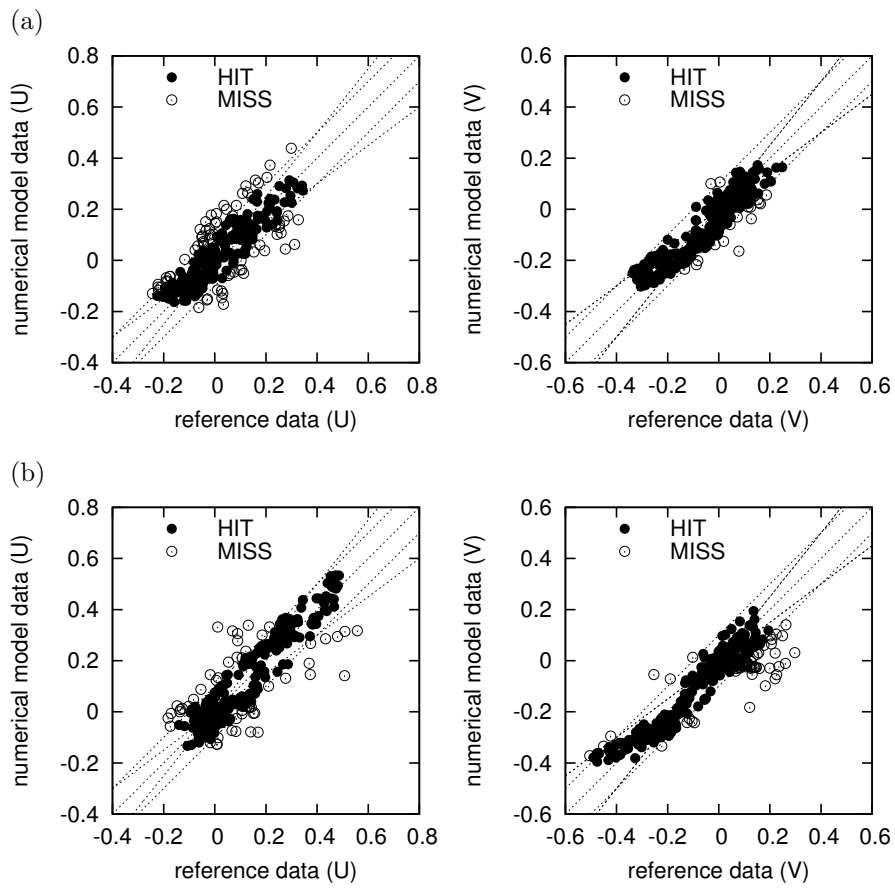


Figure 4.15: Scatter plot of normalised wind speed components for all cases (a) 270-03, (b) 270-10. For explanation see Figure 4.13.

4. EVALUATION OF SIMULATED WIND FIELDS

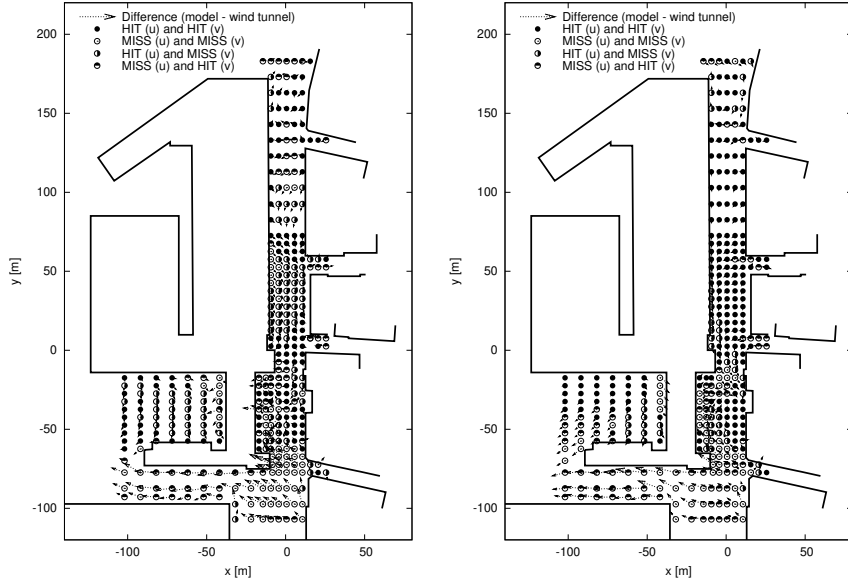


Figure 4.16: Locations of *Hit* and *Miss* for cases *220-03* and *220-10* and difference vector between MITRAS and wind tunnel results. Data points are at 3 m (left panel) and 10 m (right panel) above ground.

values is clustered near the southern end of the domain. For this wind direction, only one flat warehouse building and an otherwise largely open space is upwind of the investigated section of the domain (Section 4.4.4). This open space is incorporated in the numerical model by a roughness length approach representing an area with mainly vegetation and few buildings, while in the wind tunnel model this area is flat. The area is large enough that some flow adjustment can take place and hence the effective inflow profiles near the investigated section of the domain may differ, so that also the compared sampling points at the upwind edge of the domain may be affected. The differences will be diminished at locations where the flow pattern is dominated through large obstacles (e. g. further into the street canyon) as confirmed by the higher number of *Hit* points in this area. Figure 4.17 shows the lowest number of *Hit* points of case *260* in an area of the main street canyon near the convergence point (Figure 4.11). This suggests that the location of the convergence point differs slightly between numerical model and wind tunnel. Figure 4.18, however, suggest that for case *270* the convergence point has

4. EVALUATION OF SIMULATED WIND FIELDS

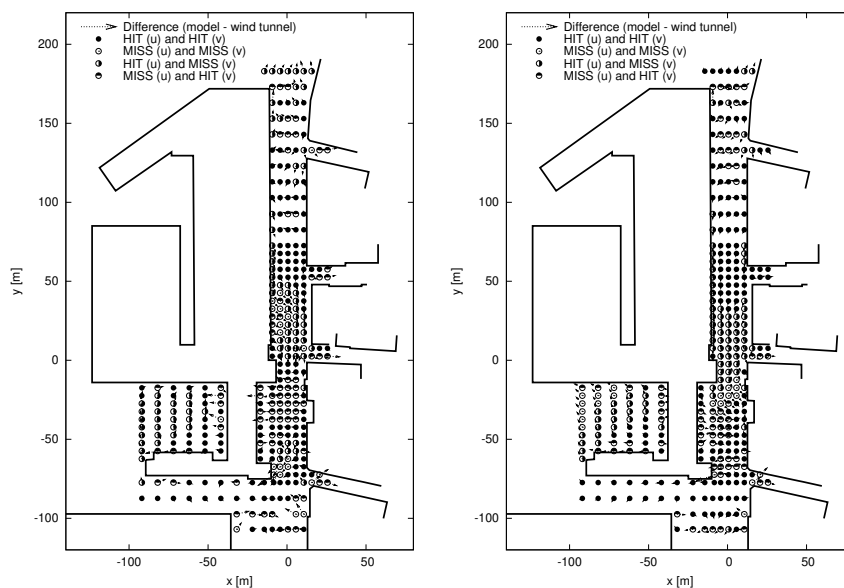


Figure 4.17: Locations of *Hit* and *Miss* for cases *260-03* and *260-10* and difference vector between MITRAS and wind tunnel results. Data points are at 3 m (left panel) and 10 m (right panel) above ground.

been calculated very well.

4.5 Summary and Discussion

An established evaluation method for microscale numerical models has been employed to evaluate results of the obstacle resolving microscale model MITRAS in comparison with wind tunnel data. The comparison of numerical model results with wind tunnel data for idealised and realistic test cases has shown that results from the model MITRAS agree well with the reference data and the hit-rate meets or exceeds the required threshold in the majority of cases.

For idealised cases, the required hit-rate is met or exceeded in all but one of the comparisons. Differences occur mainly limited to the area very near the obstacle, especially near the edges. Where differences occur, the wind tunnel model form consistently stronger and larger vortices. This should be further investigated.

4. EVALUATION OF SIMULATED WIND FIELDS

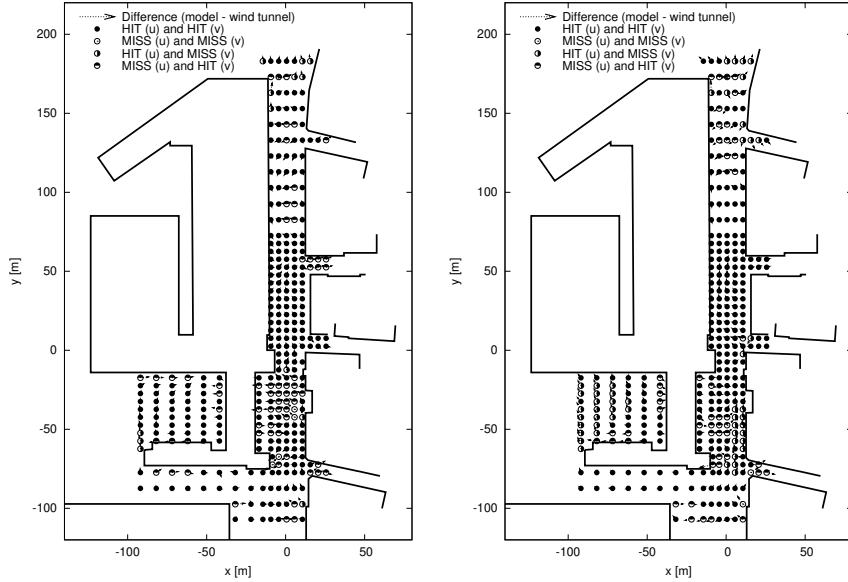


Figure 4.18: Locations of *Hit* and *Miss* for cases *270-03* and *270-10* and difference vector between MITRAS and wind tunnel results. Data points are at 3 m (left panel) and 10 m (right panel) above ground.

Transfer of the evaluation technique to realistic test cases has highlighted that seemingly minor differences between the respective set-up of both models can easily obscure the comparison so that differences between numerical model result and wind tunnel data cannot be easily attributed to shortcomings of the particular model. For each case a balance needs to be found between comparability with the real domain (and meteorological situation) and with the reference data-set. For the present study, the reference wind speed for the normalisation of all wind values proved to be the most critical parameter. This problem will be more prominent with growing complexity of model domains and situations.

5 Assessment of simulated concentrations

This chapter has been prepared for publication as:

Grawe, D., Schlünzen, K. H., 2019. Numerical modeling of pollutant dispersion in a complex urban area, in preparation for Atmospheric Environment

The chapter includes the full manuscript except for some editorial changes. Layout and numbering have been adapted to the thesis document. The abstract is not included and references and acknowledgements have been integrated into the separate sections of the thesis document.

K. Heinke Schlünzen has contributed some ideas for and to the discussion of results.

5.1 Introduction

Air pollutant concentrations in urban areas remain at a harmful level particularly at hot spot locations. At several sites in Germany and across Europe legal concentration levels are exceeded (European Environment Agency,

2018). Air quality management for the protection of human health requires the detailed assessment of concentrations levels. Such an assessment can be made with in-situ measurements, however, particularly high concentrations occur at so-called hot spot locations, which are characterised by high emissions and low ventilation. Such locations are usually within areas with complex building geometries and near emission sources. Measuring in such complex conditions yields data with usually only a low spatial representativeness. In its regulatory framework the EU guidelines (European Union, 2008) permit the use of numerical models to support the assessment of concentrations and require a spatial representativeness of 100 m along the street canyon. To achieve such a representativeness in the urban canopy layer, obstacle resolving numerical models are required.

Emitted primary pollutants such as oxides of nitrogen or carbon monoxide change their concentration in a vast number of chemical reactions. Other pollutants such as ozone or particulate matter can be formed in the atmosphere from precursors. Within the urban canopy layer, particularly in street canyons with recirculation zones and stagnation, the residence time of the air is increased. This increases the number of relevant reactions.

High resolution models may be able to provide data of the required representativeness if their results have been thoroughly evaluated and necessary input data is available.

This paper presents the obstacle resolving numerical model MICTM for the prediction of gaseous concentrations in the urban canopy layer (Section 5.2). It is part of the model system M-SYS where it can be used in combination with its mesoscale sister model MECTM. Both are based on the same set of complex chemical reactions to ensure seamless nesting. Section 5.3 describes the set-up of the model for a realistic test case. Results and comparison with wind tunnel data and field measurements are presented in Section 5.4. Further analysis of the results and suggestions for applications are given in Sections 5.5 and 5.6.

5.2 Model characteristics

MICTM is part of the M–SYS model system for the assessment of air quality at various scales (Trukenmüller et al., 2004). Together with the meteorology counterpart MITRAS (Chapter 4; Salim et al. (2018)), the chemistry model MICTM forms the microscale component of the model system and is capable to explicitly take into account the effect of obstacles on the dispersion. MICTM is a 3–dimensional numerical model for the calculation of transport and chemical reactions for microscale applications. It is based on the mesoscale chemistry and transport model MECTM (Müller et al., 2000), hence both models share core properties and program code. MICTM has already been successfully applied by Schlüter (2006) for the investigation of biogenic emissions from a forest.

For meteorology as well as chemistry, MICTM is nested into the mesoscale models METRAS and MECTM. MICTM uses meteorology data calculated by MITRAS. Both models employ the same Arakawa–C grid, where scalar variables are located at the centre of grid cells and the vector components are shifted to the edges of the cell along the respective axis. Since the same numerical grid is used in both models no interpolation is required between MITRAS and MICTM. This ensures the conservation of mass and momentum conservation.

5.2.1 Equations

MICTM calculates concentrations of gaseous pollutants from Equation 5.1 (Meyer, 2006)

$$\frac{\rho_0 \partial C_i}{\partial t} = \underbrace{-\frac{\partial \rho_0 u_j C_i}{\partial x_j}}_{\text{advection}} + \underbrace{\frac{\partial}{\partial x_j} \left(K_j \frac{\partial \rho_0 C_i}{\partial x_j} \right)}_{\text{diffusion}} + \underbrace{\rho_0 S_i}_{\text{reaction}} - \underbrace{\rho_0 D_i}_{\text{deposition}} + \underbrace{\rho_0 E_i}_{\text{emission}} \quad (5.1)$$

where C_i is the chemical concentration of species i , x_j is the grid axis for dimension j , u_j is the wind component along axis x_j , K_j are the components of the diffusivity tensor (calculated as K_{hor} for $j = 1, 2$ and K_{ver} for $j = 3$)

and ρ_0 is the air density. S_i represents sources and sinks due to chemical reactions, D_i is the dry deposition and E_i represents the emissions. The calculation of these processes in MICTM is described in the following sections.

5.2.2 Advection and diffusion

The meteorological variables for advection and diffusion are provided by the microscale obstacle resolving model MITRAS (Salim et al. (2018); Chapter 4). MITRAS is a 3-dimensional, prognostic, microscale, numerical model for the prediction of flow and transport in the vicinity of obstacles. It is based on the Reynolds-averaged Navier-Stokes (RANS) equations and contains different turbulence parametrisations to calculate exchange coefficients.

The calculation of wind velocity and exchange coefficients is performed in MITRAS which is coupled off-line. MITRAS is initialised with a frictionless wind speed and direction and optionally with vertical profiles of temperature and humidity. If desired these initial conditions can be derived from the meso-scale model METRAS. MITRAS is applied here in a quasi-stationary set-up using a time-slice approach (Schlünzen et al., 2011) to provide wind and turbulence field. This wind field is stored and used by MICTM to calculate the dispersion of emitted species. This approach is valid only as long as the larger scale conditions do not change significantly. When the large scale conditions change the wind field needs to be updated. In cases where this is not sufficient time-dependent runs can also be performed, but with a higher computational effort.

If the flow is fully turbulent and in the absence of thermal stratification, the wind and turbulence characteristics can be scaled to different wind speeds (VDI, 2017b). Therefore, wind fields can be pre-calculated for different wind directions but only one wind speed and for any current conditions the corresponding wind field can be selected and scaled according to

$$u = U/U_0 \cdot u_0 \tag{5.2}$$

$$v = U/U_0 \cdot v_0 \tag{5.3}$$

$$w = U/U_0 \cdot w_0 \tag{5.4}$$

The exchange coefficient needs to be scaled from the ground up to the lowest grid point only:

$$K_{ver} = U/U_0 \cdot K_{0,ver} \quad (5.5)$$

$$K_{hor} = U/U_0 \cdot K_{0,hor} \quad (5.6)$$

$$(5.7)$$

And above the exchange coefficients can be used directly:

$$K_{ver} = K_{0,ver} \quad (5.8)$$

$$K_{hor} = K_{0,hor} \quad (5.9)$$

where u , v and w are the required wind components and K_{ver} and K_{hor} are the parametrised vertical and horizontal exchange coefficients (required in Equation 5.1). Variables with subscript 0 indicate the respective values calculated by MITRAS with reference wind speed U_0 . U is the current reference wind speed and U_0 the reference wind speed of the MITRAS calculation.

5.2.3 Chemical reactions

For the calculation of chemical transformation MICTM employs a modified version of the RADM2 (second generation regional acid deposition model) chemical mechanism (Stockwell et al., 1990; Müller et al., 2000). This mechanism was originally developed for atmospheric chemistry at a regional scale and solves 21 photolytical reactions and 137 higher order reactions for 63 species. It can be used to predict ozone, nitrogen dioxide and several other gaseous species based on emissions of oxides of nitrogen (NO_x) and volatile organic compounds (VOCs). It contains the relevant reactions for the calculation of relevant pollutants within a street canyon. Due to its suitability for regional applications it may also include chemical reactions that are not relevant within the residence time of air particles in an urban microscale domain. A reduced mechanism with only 32 reactions has been proposed by VDI (2017a). However, the mesoscale air quality model MECTM which provides initial and boundary values for MICTM employs RADM2. Using the

same reaction mechanism between both models ensures that at the boundary both models can be matched well using the same species in the same chemical reactions. This consistency helps to avoid triggering unrealistic conversion rates due to a different set of species. The set of equations is solved using a hybrid solver (Young and Boris, 1977).

Photochemical reaction rates are calculated using the program STAR (Ruggaber and Dlugi, 1994). The photolysis reactions are shown in Appendix B.3. In order to calculate photolysis rates for MICTM, the preprocessor STAR (Ruggaber and Dlugi, 1994) requires information about the meteorological situation. While the opacity due to absorption within the whole troposphere is relevant, MITRAS domain commonly only represents a domain within the boundary layer. However, since the larger scale model METRAS is used at the same location, a one-dimensional profile is extracted for the MICTM location to calculate photolysis rates.

5.2.4 Emissions

Anthropogenic emissions of all chemical species can be considered in MICTM as area, line or point sources. Line and area sources, such as traffic emissions are emitted into the lowest atmospheric grid level. Point sources, e. g. known emissions from individual stacks can be placed into arbitrary grid levels to incorporate their actual emission height. Immediate homogeneous mixing of emitted substances and existing substances is assumed in all emission grid cells. For emissions from moving vehicles local turbulence supports a fast mixing of emissions with air in the immediate surrounding, so that for fine grid resolutions this assumption seems realistic in the urban domain. Total traffic emissions depend on traffic rates and driving mode, and respective emission factors for each vehicle type. Data can be parameterised from total emissions and time functions that consider a generic temporal distribution of traffic emissions or from time resolved emissions from actual datasets. Total emissions are allocated to each grid cell as mass per area and time.

An additional pre-processor enables the consideration of biogenic VOC-emissions from vegetation. Emissions are calculated from the surface land-

use and air temperature of each grid cell according to Vogel et al. (1996).

5.2.5 Input data provision for MICTM

Within the model system M-SYS the mesoscale components METRAS and MECTM are used to provide initial and boundary conditions for meteorology and chemistry using a one-way nesting approach. The wind field required by MICTM is calculated offline using the obstacle resolving microscale model MITRAS (Grawe et al., 2013a). The set-up has been optimised for the calculation of hourly concentration values. This is the time resolution required for several metrics by European air quality legislation. It is therefore also the time resolution used for operational air quality measurements taken in Göttinger Straße. In the time-slice approach (Schlünzen et al., 2011) it is assumed that for each hourly interval the temporal variability of the meteorological conditions (especially the flow field) in the model domain is small. MITRAS calculates quasi-stationary results of the flow field for MICTM, and is therefore only required to provide one flow field per hourly simulation. This is kept constant throughout the MICTM simulation. The MICTM set-up and input data requirements are outlined in Figure 5.1. For each of these models a 1d-profile is extracted from the results. The METRAS-profile is used to scale the MITRAS result according to Equations 5.3 – 5.9 and to provide input data for the photolysis rate calculation. The MECTM results is used to extract initial and boundary data. As initial conditions a horizontally homogeneous distribution of the concentrations is assumed at the start of the model simulation.

5.3 Realistic test case

A MICTM model domain has been set-up for a section of Göttinger Straße and the surrounding area in Hanover (Figure 4.8). This domain has been selected because high resolution emission data and several measurements are available. Göttinger Straße is a large arterial road with approximately 30'000 vehicles per day (daily traffic rate, DTR) in two vehicle lanes per direction.

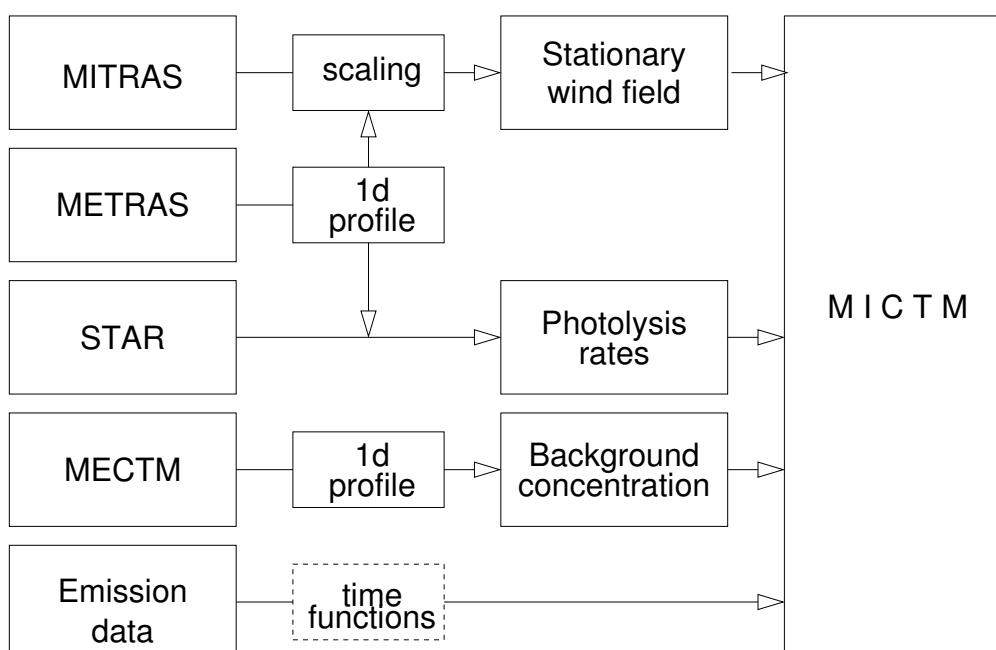


Figure 5.1: Diagram of MICTM set-up and input data requirements. Boxes in the first column represent data sets required for a MICTM run. The second column shows the values to be extracted or processed from each data set. The third column names the variables calculated from this process. They are required as input for MICTM.

There is a high fraction of heavy duty vehicles (NLÖ and FZK, 2004). The street axis is rotated 17 degrees west against the North-South-axis and the prevailing wind direction is South-West (NLÖ and FZK, 2004). The building on the western side of the road is an industrial building which is uninterrupted for approximately 100 m parallel to the street, while on the eastern side only three small residential streets interrupt the buildings. This geometry forms a well pronounced street canyon with an aspect ratio (height over width) of approximately 1. Near the southern edge of the main building on the western side, two gateways pass through the building and the building hangs over the footpath for some 10 m, forming a more complex geometry and flow field in this area. Further away from the street canyon, a largely open area can be found in the south-west of the domain. Mostly residential buildings in side streets with some courtyards can be found east of the main canyon. Towards the North the main street leads into a large open space roundabout. Traffic lights in this roundabout and near the South of the main building along the

street affect the spatial pattern of pollutant emissions.

The numerical grid employed in MICTM is the same as in MITRAS used for this domain (Chapter 4). The grid width has a very fine resolution of 1.5 m near the center of the area of interest which is in the main street canyon. Outside of this area the grid width increases by a factor of 1.2. The maximum horizontal grid width is 15.0 m and the maximum vertical grid width is approximately 30 m. The top of the model domain is at 400 m above ground.

5.3.1 Meteorological conditions

For a realistic test case the 11 April 2003, 7-8 a.m. has been selected. At this time of day high emissions from the morning rush hour can coincide with a low residual nocturnal boundary layer. This stable stratification above the canopy layer is accounted for in the initial data provided by the meso-scale model. At the same time the canopy layer will already be well mixed due to the ventilation induced by the buildings. Neutral stratification is therefore assumed for the microscale model so that the wind and turbulence field could be scaled to the realistic conditions. The measured data above roof for this situation is a wind speed of $2.7 \text{ m} \cdot \text{s}^{-1}$ and a wind direction of 220° . A quasi-stationary wind field for this wind direction has been calculated by MITRAS for a wind speed of $1.0 \text{ m} \cdot \text{s}^{-1}$ above roof. The resulting wind field at two heights above ground is shown in Figure 5.2. The above roof wind direction of 220° can be seen in the bottom left area of the shown section. Upwind of this area is a largely open space. In the main street canyon the flow is channelled along the axis of the canyon at $z = 10.0 \text{ m}$ (0.4 building heights). In the courtyards to the right of the main street canyon the flow follows the main wind direction in average, but some channelling occurs between the buildings. At $z = 1.5 \text{ m}$ the upwind flow direction is similar. However, the building outline differs left of the main street canyon due to an underpass of one building. This increases the across canyon wind speed in this area of the main canyon. Along the main street canyon the flow is also along the street canyon, but with a notable cross-canyon wind component. In the courtyards the flow is more variable than above. However, the general flow direction

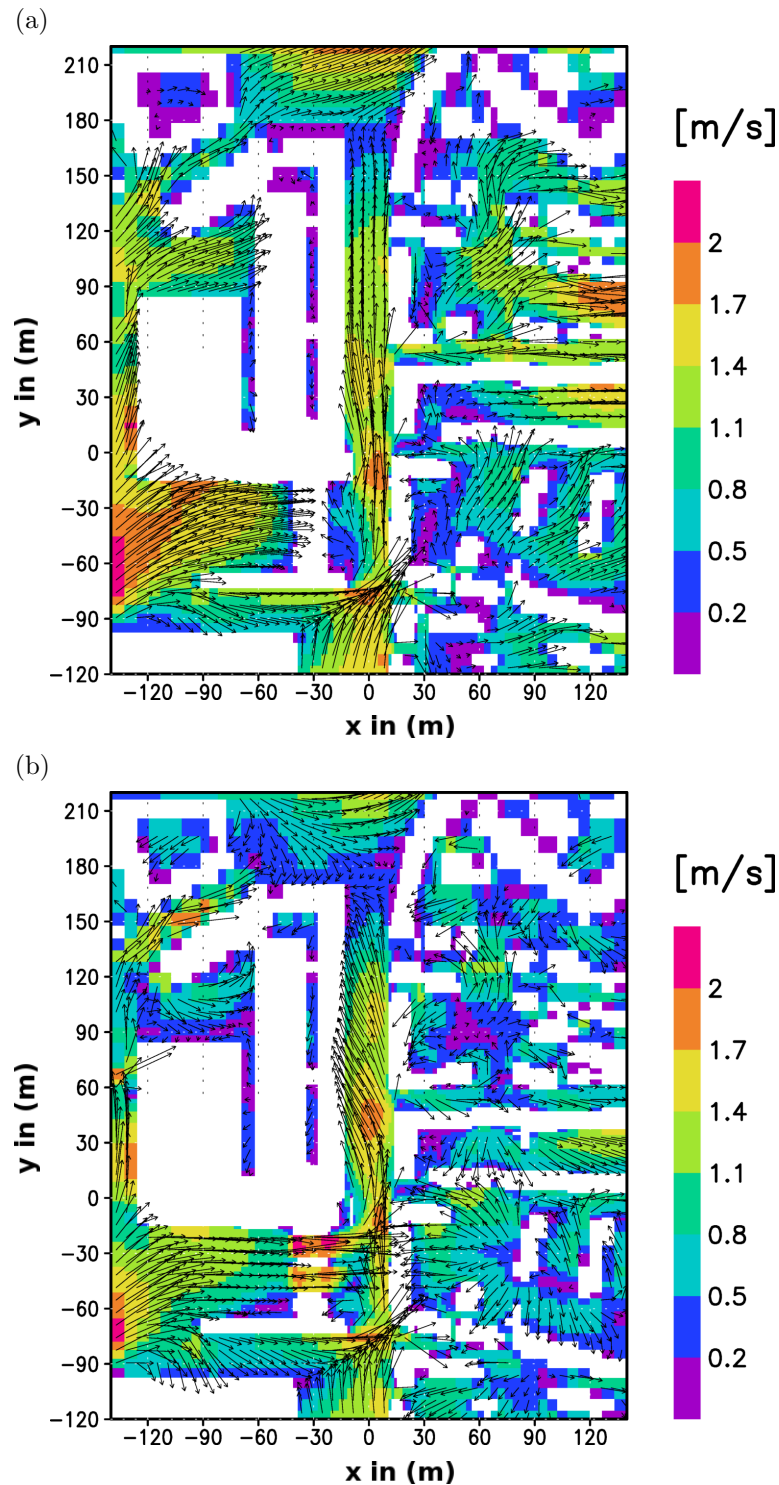


Figure 5.2: Horizontal wind field for 7-8 a.m. on 11 April 2003 calculated by MITRAS. (a) 10 m above ground, (b) 3 m above ground. White areas indicate the outline of buildings in the respective level. (reproduced from Grawe et al. (2013a), here also Figure 4.10)

in this area is in the opposite direction of the above roof wind direction. Despite the south–westerly above roof flow, the main canyon ventilates into some side streets, while for other side streets the flow is towards the main canyon. The general flow pattern implies a flow along the main street canyon which is overlaid by a street canyon vortex with wind across the canyon near the bottom. Near the downwind end of the street canyon the flow is also separated between both levels with flow into the street canyon near the surface at $z = 3$ m and flow out of the canyon above at $z = 10$ m.

5.3.2 Chemical conditions

MICTM has been nested into results of the mesoscale chemistry model MECTM. The numerical grid for both models was aligned so that — horizontally — the MICTM model domain corresponds to one grid cell of the MECTM model domain. Therefore, the MECTM results can be used directly as initial concentrations and as boundary concentrations in the time-slice approach. The model grids differ in the vertical direction, because the microscale model employs a much higher resolution, while the mesoscale grid reaches into higher levels of the atmosphere. Therefore, the results need to be interpolated vertically onto the finer grid.

Figure 5.3 shows the initial and boundary concentrations for selected species calculated by MECTM (Trukenmüller et al., 2004). The data were calculated and used for all species of the RADM2 mechanism. The vertical profile for all species exhibit some vertical variability even in the lowest 350 m of the boundary layer. This supports the approach to use results of a three–dimensional model rather than homogeneous values for initial and background concentrations.

Both, NO and NO₂ (and consequently NO_x) show higher concentrations near the ground, where urban emissions are already taken into account by the mesoscale model. However, the meso–scale model has a horizontal resolution of 1 km so that hot–spot locations are averaged across a large area. These values therefore constitute the background. A further peak of oxides of nitrogen can be found elevated at a height near 240 m. This is a level where

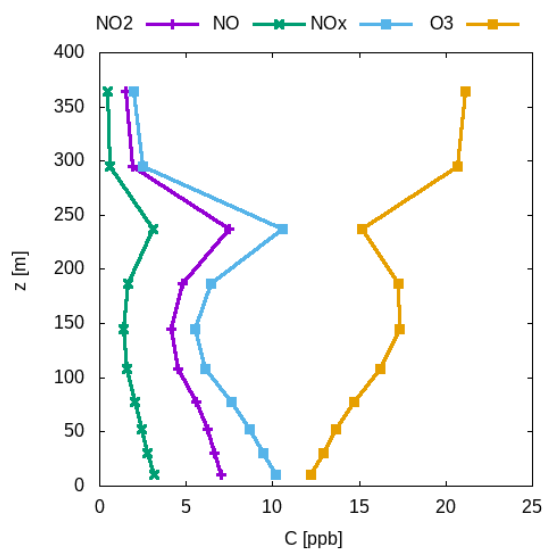


Figure 5.3: Initial and boundary concentrations for NO_2 , NO , NO_x and O_3 calculated by MECTM for 11 April 2003, 7-8 a.m. (Trukenmüller et al., 2004).

industrial stack emissions are considered as point sources. The closely tied reactions between nitrogen oxides and ozone cause reduced O_3 concentrations in levels with high NO emissions.

5.3.3 Photolysis rates

Hourly photolysis rates for the 11 April 2003 were calculated based on the METRAS results for this day and interpolated onto the MITRAS vertical grid. Figure 5.4 shows vertical profiles of photolysis rates used for 7 a.m. for NO_2 , O_3 and NO_3 . All photolysis rates decrease vertically towards the ground within the MICTM domain as more incoming short-wave radiation is absorbed in the atmosphere. The photolysis rates at the bottom of the domain are reduced to between 81% and 91% compared to the values at the model top.

5.3.4 Emissions

High quality emission data for this study were prepared by the IER (Kühlwein and Friedrich, 2004; Kühlwein, 2003). Special emphasis has been put on the

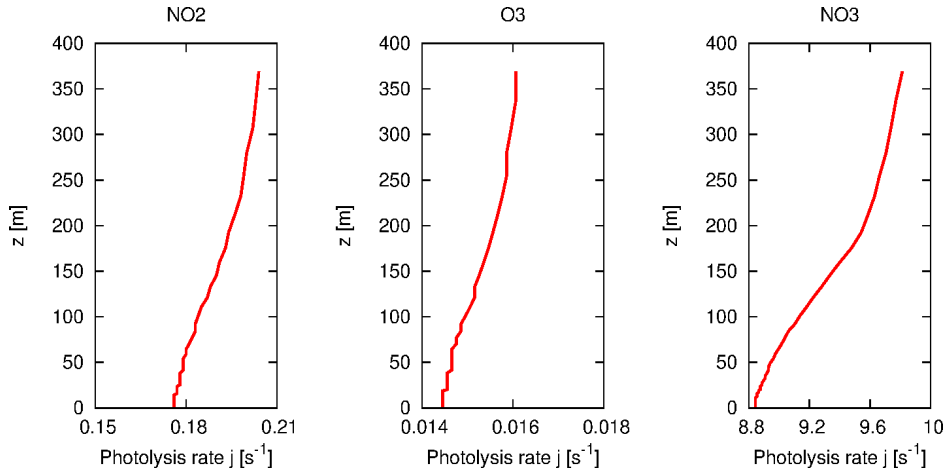


Figure 5.4: Vertical profile of selected photolysis rates.

emission data for the main street canyon Göttinger Straße. During a campaign period the individual vehicles passing through the street were identified through their registration number so that anonymised fleet data could be obtained from the vehicle registration office. Together with a measurement of the speed of each vehicle this approach allows the calculation of more precise emission data for the campaign period compared with generic emission factors for a vehicle mix. This detailed approach could not be used for the complete model domain where generic emission factors and traffic rates have been used. The spatial distribution of NO_x emissions is shown in Figure 5.5(a). Highest emission values can be found for the main street canyon Göttinger Straße in the centre of the plot. High values also occur for the large roundabout towards the North of Göttinger Straße. Locally increased emissions occur at intersection with stopping and accelerating vehicles. Some emissions of different magnitude also occur in all side streets. Across Göttinger Straße the four different lanes can be distinguished in the gridded emission data (Figure 5.5(b)). Figure 5.6 shows the temporal distribution of emissions. In order to calculate a relevant situation with high emissions, the morning rush hour has been selected for the model run. At this time the emissions are close to the maximum for the day. The traffic emission data was reported for NO_x , SO_2 , CO , NH_3 , CH_4 and 31 NMVOCs on 11 April 2003. Nitrogen oxides had to be split further for the model into NO_2 and NO . A ratio of $\text{NO}/\text{NO}_x = 0.85$ has been assumed for this case

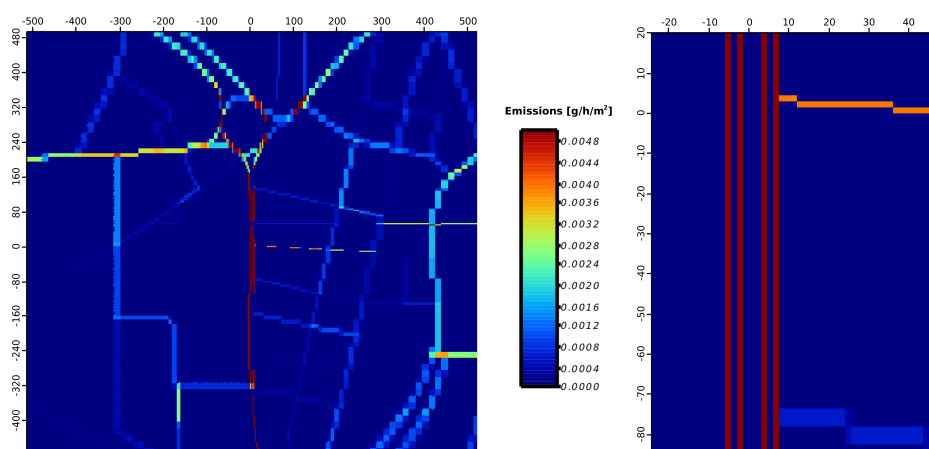


Figure 5.5: Spatial pattern of NO_x emissions for 7-8 a.m. on 11 April 2003 (Kühlwein, 2003). (a) Complete model domain; (b) enlarged section of the main street canyon to highlight the resolution of individual traffic lanes.

due to the high fraction of heavy duty vehicles in Göttinger Straße. The total sum of VOC emissions was split into and allocated to separate species of the RADM2 mechanism according to Appendix C.

5.4 Results

Chemical reactions were calculated for one hour and averaged over the period. Averaging the results is consistent with the quasi-stationary calculation of the wind field. It also allows the comparison with time-averaged field measurements. Figure 5.7 shows horizontal and vertical cross sections of the concentration of CO in the domain. CO is assumed to be non-reacting within the model run time. The horizontal cross section is at $z = 1.5$ m, the so-called *nose height* at which adults breath air. It is also the height of the field measurements in the street canyon. The horizontal cross section shows low concentrations representative of the urban background upwind of the main street canyon (South-West, lower left in the figure). Elevated concentrations occur for all streets with traffic emissions within the domain. Concentrations are particularly high in locations with low wind speeds. These occur in the main street canyon, but also in some smaller streets across the domain. Horizontal concentration patterns in the main street canyon resemble the

5. ASSESSMENT OF SIMULATED CONCENTRATIONS

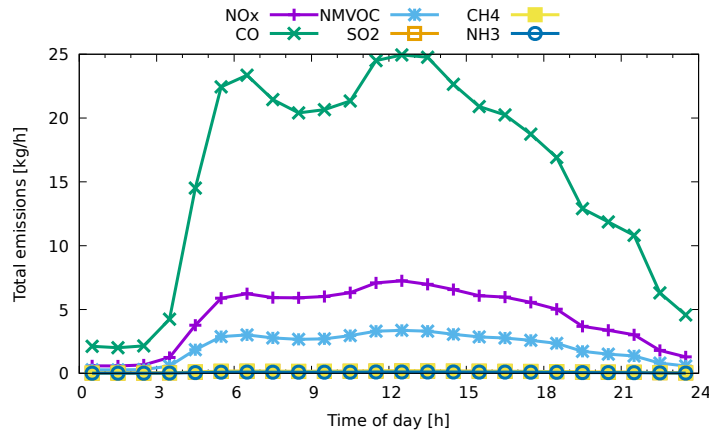


Figure 5.6: Total emissions of selected species across the MICTM domain (Kühlwein, 2003) for 11 April 2003. Time of day is given in UTC; therefore the value indicated between e.g. 5 and 6 a.m. corresponds to the hourly emissions between 7 and 8 a.m. local time. NMVOC indicates VOC emissions without methane CH_4 .

air flow described in Section 5.3.1: Air flow through the underpass travels in a corcscrew pattern across the street canyon and transports the emitted CO towards the leeward side of the canyon. Particularly towards the North exit of the canyon very low wind speeds occur so that pollutants are less diluted leading to increased concentrations. Within very short distances of several metres across the street canyon the concentrations easily vary by a factor of four and more. Above the canopy layer concentrations are mostly homogeneous (Figure 5.7(b)). The vertical cross section is placed in a section where the street canyon is closed at the lateral sides. It shows high spatial variability and large gradients in the street canyon. Highest concentrations occur near the ground where the emissions occur separated into four traffic lanes. The corcscrew patterned flow transports the pollutants towards the leeward site of the street canyon where again they can accumulate due to the low wind speeds. Substantially increased concentrations also occur at the downwind edge of the street canyon, implying that much of the emitted pollutants are trapped in the street canyon. Some concentrations, however, are drained from the street canyon and transported into the courtyards adjacent to the street canyon and further.

Vertically, also very high concentration gradients occur. Highest values are

found at the bottom near the emission sources and immediately downwind (left in Figure 5.7(b)). The vortex then transports the emitted pollutants up along the leeward (left) building of the street canyon where eventually it is mixed with clearer background air aloft.

Figures 5.8 and 5.9 show the concentrations of NO and NO₂, respectively. Oxides of nitrogen are emitted as nitric oxide (NO) and nitrogen dioxide (NO₂) in a ratio of 85% and 15%. Of the emitted NO_x, NO₂ is reduced by photolysis and NO reacts with existing background O₃ changing the ratio of NO₂ and NO towards more NO₂ (this cannot be seen in the figure due to high emissions).

Figures 5.7 – 5.9 show concentrations of emitted pollutants. These are emitted in the street canyon and hence increased concentrations can be found there. O₃ is a secondary pollutant formed in slow reactions from e.g. VOCs. These reactions are represented in MECTM as well as in MICTM. Increased values therefore occur further from emission sources of *VOCs*. For urban areas, O₃ represents primarily a background value. A relatively high background concentration occurs above the canopy layer. This O₃ is reduced from reactions with NO particularly near the emission sources at the ground (Figure 5.10). The spatial pattern of the concentrations is very similar for all species although some species show increases while others show decreases. For the evaluation of numerical model results, good comparison data is an important requirement. In general, independent comparison data can be obtained with either field measurements or physical model measurements. The latter is usually obtained from a wind tunnel. Both techniques have advantages and disadvantages for the comparison. Field experiments often include only a limited number of data points due to the required measurement instruments. Wind tunnel results allow many more data points at a very high spatial resolution and are prepared with well defined boundary conditions, but do not take into account the chemical processes and not necessarily all physical processes in the boundary layer. Both types of data are available in this study and a comparison is shown for both datasets in the following sections.

5. ASSESSMENT OF SIMULATED CONCENTRATIONS

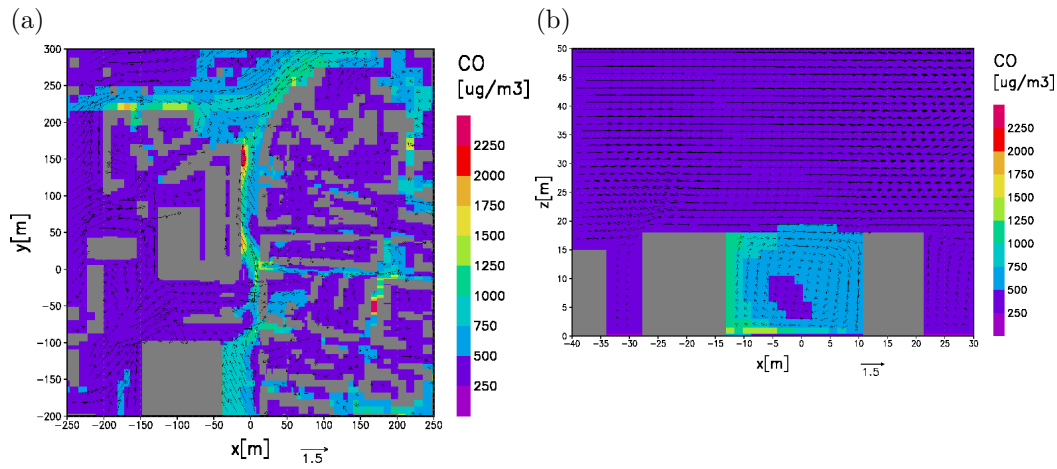


Figure 5.7: Calculated concentration of CO for 7-8 a.m. on 11 April 2003. (a) horizontal cross section at $z = 1.5$ m, (b) vertical cross section across main street canyon at $y = 80$ m.

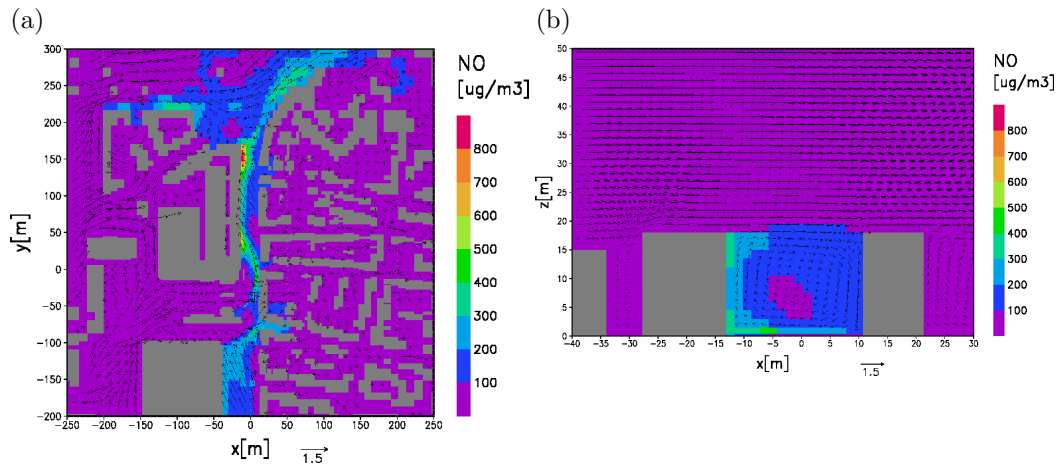


Figure 5.8: Calculated concentration of NO for 7-8 a.m. on 11 April 2003. (a) horizontal cross section at $z = 1.5$ m, (b) vertical cross section across main street canyon at $y = 80$ m.

5.4.1 Comparison with wind tunnel data

The wind tunnel data used in this study were measured with a physical scale model in the large boundary layer wind tunnel WOTAN of the Environmental Wind Tunnel Laboratory (EWTL) at the University of Hamburg. Measurements were taken over flat terrain for the area of Göttinger Straße. A

5. ASSESSMENT OF SIMULATED CONCENTRATIONS

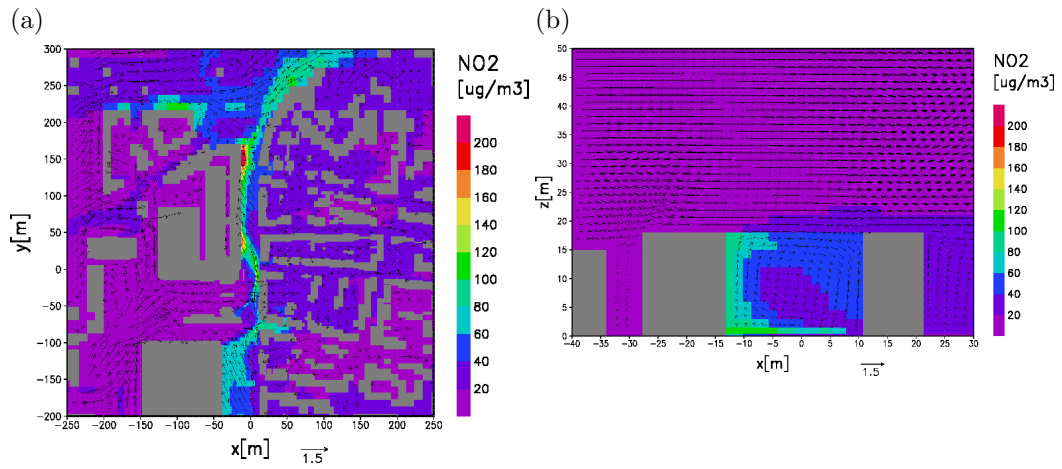


Figure 5.9: Calculated concentration of NO₂ for 7-8 a.m. on 11 April 2003. (a) horizontal cross section at $z = 1.5$ m, (b) vertical cross section across main street canyon at $y = 80$ m.

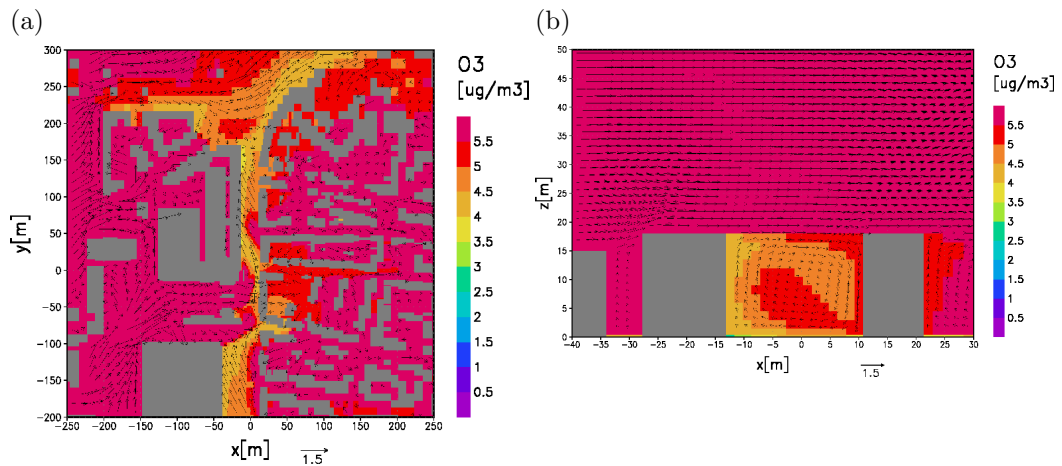


Figure 5.10: Concentration of O₃ for 7-8 a.m. on 11 April 2003. (a) horizontal cross section at $z = 1.5$ m, (b) vertical cross section across main street canyon at $y = 80$ m.

passive tracer was used to measure concentrations at three horizontal cross sections and for three different approach flow wind directions. Out of the three available data sets the wind direction for one case matches the realistic MICTM test case.

However, the modelling approach is somehow different between both mod-

els. The wind tunnel result has ground level emissions but no background concentration. The models were also applied for different wind speeds. In order to make the data comparable, the concept of a non-dimensional concentration c^* has been used (VDI, 2000). The concentration in this concept is considered to be a function of wind speed, wind direction, emission strength, background concentration and obstacle geometry. These variables can be recombined in a dimensional analysis to a non-dimensional variable c^* .

$$c^*(x, y, z) = \frac{|C(x, y, z) - C_0| \cdot |U|}{E \cdot L} \quad (5.10)$$

where C is the local concentration (in $\mu\text{g}/\text{m}^3$), C_0 the background concentration ($\mu\text{g}/\text{m}^3$), $|U|$ the characteristic wind speed (in m/s), E the emissions (in $\mu\text{g}/\text{m}^3/\text{s}$), and L the characteristic length scale of the obstacle geometry (in m). Assuming that other relevant factors such as thermal stratification are the same between both models, the resulting c^* only depends on the large scale wind direction. For the comparison performed here this is not completely the case. The emission source pattern for both models is complex and covers different areas. The wind tunnel model focusses on the main street canyon and some side streets. MICTM uses emissions with different rates across all streets in the domain. To take this into account for the whole domain, the average concentration was used to normalise c^* further. However, this can only make up for different total emissions, not for differences of the spatial distribution of the emissions. The overall distribution of normalised concentrations is similar between wind tunnel data and numerical model result (Figure 5.11). Maximum concentrations occur near the building on the leeward side of the street canyon (left in the Figures 5.11 5.10(a) and 5.10(b)). For this wind direction the wind also has a component along the street canyon so that higher concentrations occur towards the northward outlet of the street. For both data sets there is no substantial flow into backyards on either side of the canyon. However, the numerical model has some elevated concentrations in side streets where emissions occur which were not included in the physical model. A pronounced difference between both datasets is that the area of high concentrations along the axis of the canyon is substantially narrower in the numerical model compared to the

physical model.

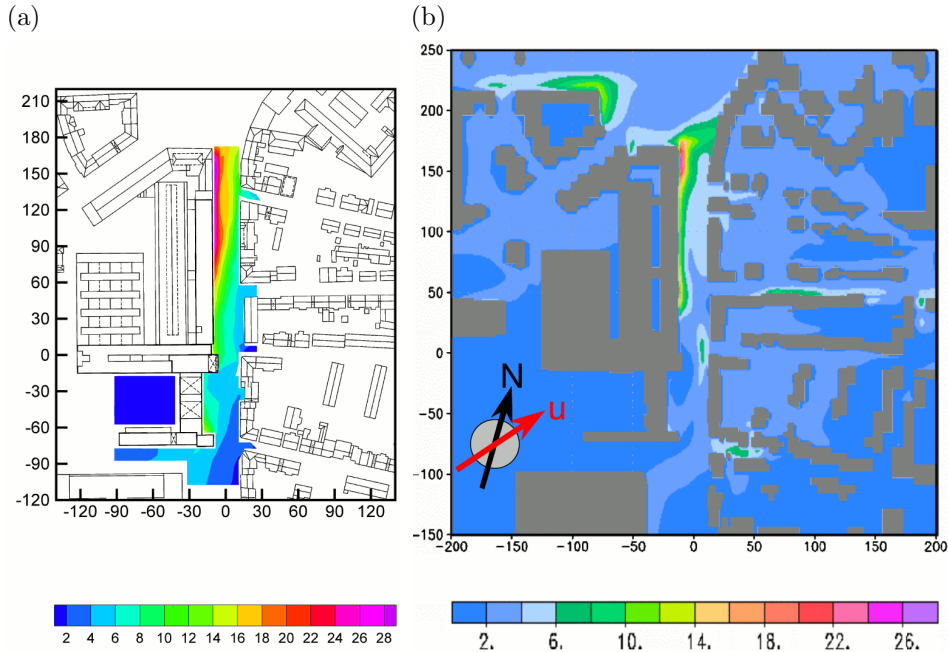


Figure 5.11: Wind tunnel data (a) and numerical model result (b) for a passive tracer for 220° approach flow. Shaded areas show the non-dimensional concentration c^* at $z = 1.5$ m (Equation 5.10). Note the slightly different colour scales. Arrows indicate the approach flow wind direction for this case. (wind tunnel data reproduced from EWTL, University of Hamburg Pascheke (2013))

Similar to the evaluation method for the wind field (Section 4.2.2), *Hit* and *Miss* values are calculated for c^* with an allowed relative difference of a factor of two. No absolute difference is applied. For the 651 concentration points measured in the wind tunnel, the comparison yields a hit rate of 80%. Figure 5.12 shows the distribution of *Hit* and *Miss* values. The pattern is similar at all levels. Across the main street canyon the concentrations match well. *Miss* values occur at the upwind end of the main street canyon. The comparison of wind fields has identified that in this area differences occur for both wind components (Figure 4.12(a)). Here, the complex flow pattern with, e.g. an underpass for the main building nearby, is represented differently in both models. Also in this area the emission pattern differs between wind tunnel and numerical model. Both models can therefore not be expected to match perfectly in this area.

5.4.2 Comparison with field data

In total six measurement sites were available in Göttinger Straße for the period investigated here. Hourly measurements were taken for NO_2 , NO , O_3 and CO , but not all species are available at all sites. Figure 5.13 shows the location of all measurement sites. HRSW is positioned at a mast in 42 m above ground. The building directly below has a height of 30 m. For air quality assessments this site is often used as a background site, assuming that it is not affected by local emissions and building geometry. HRVS is a long-term hot-spot measurement site with measurements at 4 m above ground. It is placed in direct vicinity of complex building structures with underpasses and near a corner. HRV1–4 are ground measurement sites at 1.5 m above ground and set-up for shorter-term measurements. HRV1 is near HRVS and placed directly next to the outermost traffic lane. HRV3 is

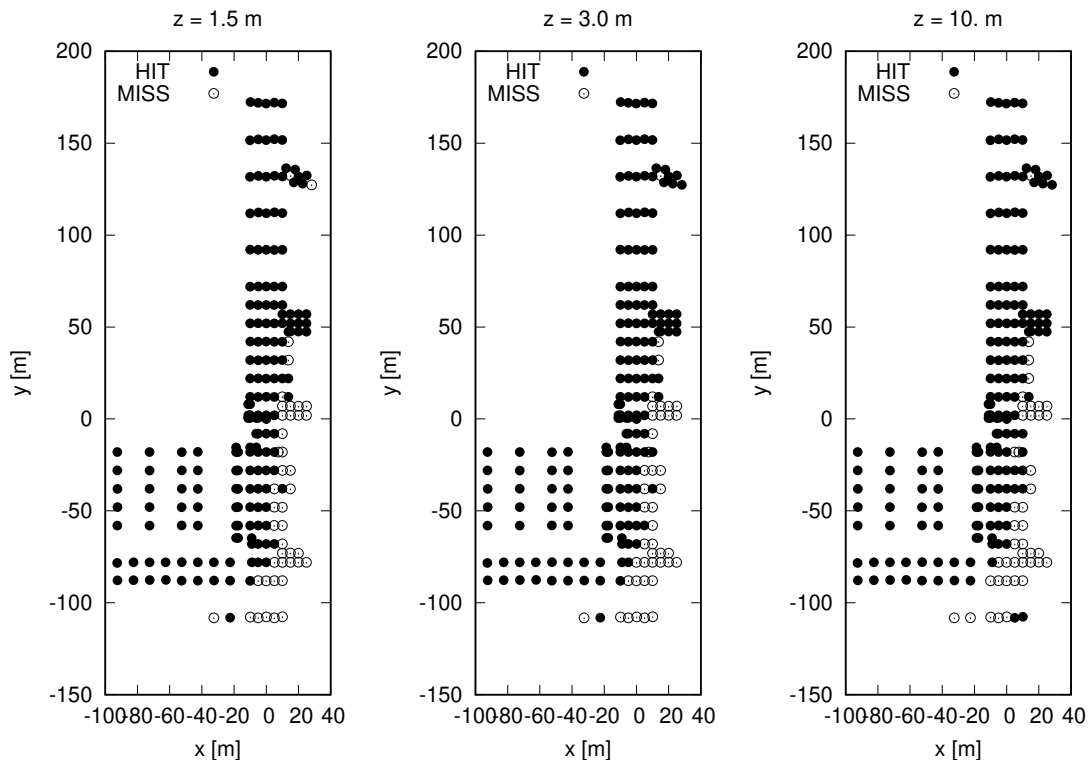


Figure 5.12: *Hit* and *Miss* pattern for 220° approach flow at three different heights ($z = 1.5$ m, $z = 3.0$ m, $z = 10.0$ m) for all available data points.



Figure 5.13: Location of field measurement sites in the model domain. Shaded areas indicate the outline of buildings, red dots show the position of six measurements sites: one above roof station (HRSW) and five roadside stations (HRVS, HRV1-4). Not all species are measured at every location.

similarly placed but on the other side of the street canyon. HRV2 is placed at the end of the street canyon between the traffic lanes. HRV4 is located in a side street off the main street canyon.

The comparison of all measurements with corresponding results of the numerical model is shown in Table 5.1. NO_x is added for information. All model values which are not within a factor of two of the measured data are shown in red. Several features of the concentration pattern identified in Figures 5.7 – 5.10 can also be found here. The background concentrations at HRSW are lower than for all traffic sites. HRV3 on the windward side of the canyon shows consistently lower concentrations of CO compared to HRV1 on the leeward side. HRV4 also exhibits lower concentrations than the traffic sites. Very good agreement between model and measurement can be found for CO at all sites. Because CO reacts slowly, this implies that emissions as well as transport and dispersion modelling are reasonable for this case. The

5. ASSESSMENT OF SIMULATED CONCENTRATIONS

Station	Data source	NO ₂	NO	O ₃	NO _x	CO
HRVS	MICTM	90	302	—	553	1156
	Validata	114	211	—	437	1354
HRV1	MICTM	—	—	—	—	1975
	Validata	—	—	—	—	1587
HRV2	MICTM	69	222	—	409	875
	Validata	172	189	—	462	1663
HRV3	MICTM	45	133	—	249	796
	Validata	80	97	—	229	720
HRV4	MICTM	29	78	5.2	149	—
	Validata	33	14	22	54	—
HRSW	MICTM	16	35	6.4	70	306
	Validata	34	13	24	54	300

Table 5.1: Comparison of model results with measured data for NO₂, NO, O₃, NO_x and CO. NO_x is calculated from NO₂ and NO as NO₂. All model values which are not within a factor of two of the measured data are shown in red. Validata measurements are taken from NLÖ and FZK (2004).

results for NO_x are similar, but with an overprediction for HRV4 in the side street.

MECTM shows an underprediction of O₃ and an overprediction of NO at HRSW. NO₂ is within the allowed deviation but also fairly low. HRSW is located above the roof and for this situation upwind of the main street canyon. The concentrations at this site are therefore mainly a reproduction of the background concentrations used in the model set-up. The measured concentration implies that for this situation the background concentration of ozone was below measured data. More available O₃ in this case would react with NO to form NO₂ and it would therefore shift the ratio of NO and NO₂ towards NO₂ in the numerical model leading to a better agreement for all three species.

Similar relations can be found for HRV4 in the side street. O₃ shows a similar underprediction, but an overprediction of NO. This implies that the concentrations at HRV4 are mainly influenced by the background and less by the local emissions, although the site is downwind of the main street canyon. Due to the street canyon vortex the flow at the level of traffic emissions is

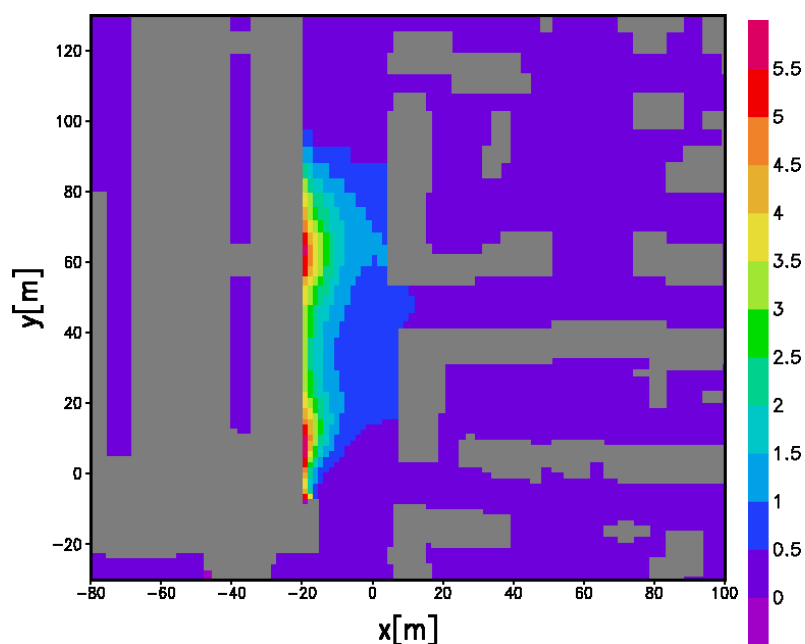


Figure 5.14: Normalised representativeness of concentrations in the main street canyon. Shaded areas show the relative concentration of a passive tracer. Values are normalised so that the concentration at the traffic station HRVS is 1.

reversed. It is then mixed at the top of the canyon into the air above. For this side street there is no additional recirculation zone which would entrain air with higher concentrations back to street level. I.e. the concentration differences are also consistent with the differences in background ozone.

5.5 Spatial representativeness

The previous sections have shown that concentrations in the investigated urban domain are highly variable and high concentration gradients exist. Particularly within the main street canyon, complex flow patterns and high emissions lead to a highly variable concentration field. Long-term point measurements have been made in this domain and it is interesting to determine how representative these measurements are for the street canyon or the wider area.

Figure 5.14 shows normalised concentrations for a passive tracer emitted from

5. ASSESSMENT OF SIMULATED CONCENTRATIONS

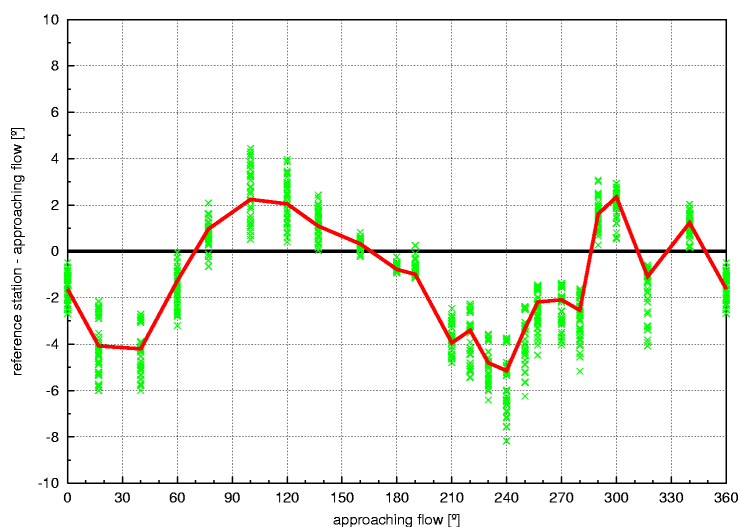


Figure 5.15: Difference between the wind direction of the approach flow and the wind direction at the above roof measurement station HRSW. The green symbols indicate the wind direction at grid points at and around the measurement location. The line connects the average value for each approach flow.

an idealised line source in the centre of the main street canyon. The approach flow is perpendicular to the street canyon from the left of the figure. The values are normalised so that the concentration at the existing measurement site HRVS is 1. It is obvious from the figure that this site cannot capture the highest concentrations of more than 5 in the street canyon which occur at the leeward side. The highest concentrations occur opposite of two side streets. For the current approach flow conditions (220° from the bottom left of the figure) this is where the recirculation in the canyon is weakest due to the side streets. Normalised concentrations around 1 occur along the street canyon. For this situation one could therefore assume that the site HRVS is representative of the concentration at a certain distance to the source. However, the measurement site is located in an area of a particularly high concentration gradient. Taking the measurement at a position shifted by only 4 m would yield a different result by up to a factor of 4. This site does therefore not fulfil the requirements on the spatial representativeness for air quality assessment. For other approach flow directions the details of the representativeness will be quantitatively different, but qualitatively very similar.

5. ASSESSMENT OF SIMULATED CONCENTRATIONS

The EU guideline (European Union, 2008) requires a spatial representativeness of 100 m along the street. To achieve this representativeness in this case would require to place a measurement site in the vicinity of less complex obstacle and emission conditions. For the current situation this would be a location further along the main street canyon by approximately 30-40 m. Here, similar conditions along the street still exist, but the concentration gradient across the street is much lower which reduces the uncertainty of the measurement. In order to apply this suggestion for the street canyon, a similar investigation should be performed for other wind directions. The spatial representativeness within the street canyon will, however, remain low if only one measurement is taken. Placing several measurement sites within one domain could help to assess the spatial variability and thereby increase the spatial representativeness of combined measured data.

Screening models often require a background measurement of wind and in some cases concentrations to determine the concentration increment for a street canyon. For the domain Göttinger Straße, the above roof station HRSW is often used as it is considered independent of local obstacles and emissions due to its height of 12 m above the highest building. Figure 5.15 shows the deviation of the wind direction at the location of HRSW calculated from different approach flow conditions with MITRAS. The red line shows results at the measurement site, green symbols show results for the surrounding grid points. Depending on the direction of the approach flow, the wind at the measurement site is sometimes deflected to the right or the left leading to positive and negative differences. The added systematic uncertainty of wind direction measurements is therefore in some cases 4-8°. It can be expected that together with the impact on wind direction the obstacles also affect the wind speed.

If the model is able to provide data at a sufficiently high resolution for a complex canopy layer, it has to be shown that these data also fulfil quality requirements. This can be performed by comparing to a network of in-situ field measurements or by comparing with another model, here a physical wind tunnel model has been used. Such an evaluation needs to include the

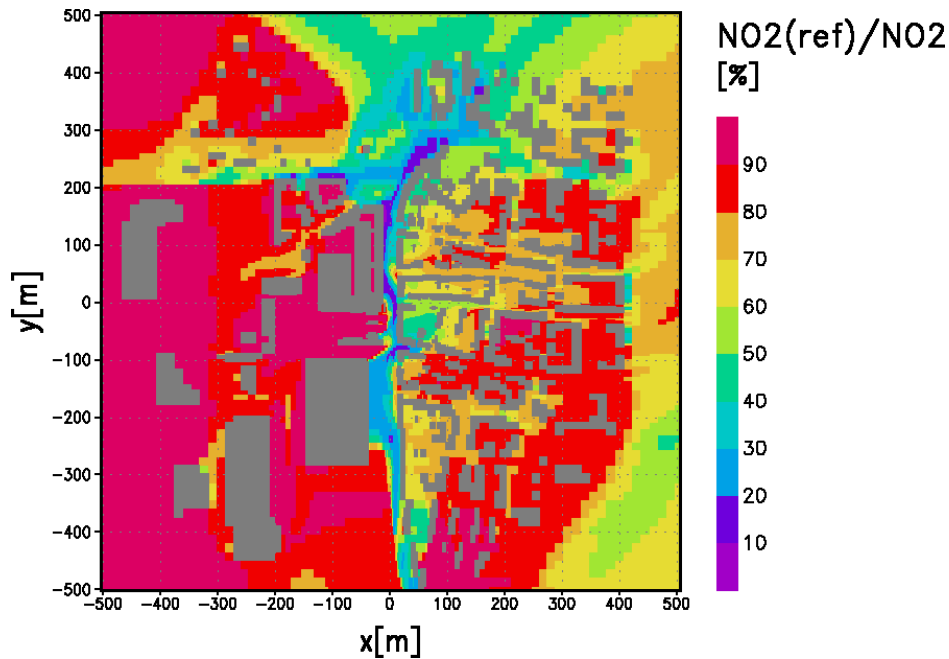


Figure 5.16: Horizontal cross section of NO_2 background concentration ($\text{NO}_2(\text{ref})$) calculated by MECTM in relation to canopy layer concentrations calculated by MICTM.

whole modelling process, not just the model itself. It could be seen from 5.4.2 that if input data (in this case boundary data) shows differences compared to reference data, such differences can also be found in the canopy layer concentrations.

5.6 Added value of urban canopy modelling of concentrations

The use of an obstacle resolving microscale model entails a high computational cost. In some cases a mesoscale model is therefore used with lower demands on computing resources. A mesoscale model does not commonly resolve the canopy layer, particularly with respect to transport and dispersion of air pollutants. Figure 5.16 shows the background concentration (calculated in this case with the mesoscale model MECTM at 1 km horizontal resolution) divided by the local ground level concentration of MICTM. Note

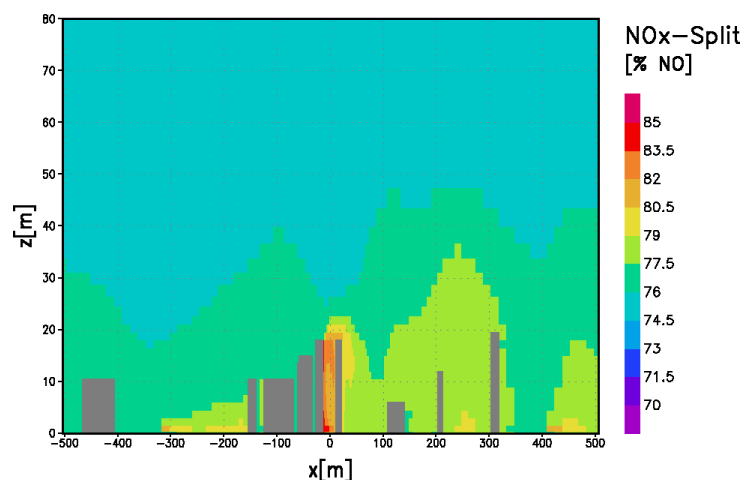


Figure 5.17: NO/NO_X ratio in and above the canopy layer. Note that the x - and z -axis have different scaling. Only a part of the domain is shown.

that the mesoscale model already incorporates urban emissions. High fractions in the figure indicate that the background value is a good representation of the ground level concentration. This is the case for e.g. upwind locations where no local emissions occur, i.e. the sector $x < -100$ m and $y < 0$ m in Figure 5.16. Near local emissions, however, the background value in some cases represents less than 20% of the hot spot concentrations. Also areas without local emissions but downwind of the main street canyon exhibit high concentrations so that the background only represents 50-80% of the ground level concentrations. The figure highlights the additional benefit of resolved recirculation zones in the urban canopy layer. It should also be noted that the highest concentrations do not necessarily occur directly near the emission source, but also in areas where emissions coincide with particularly low wind speed and therefore low ventilation.

Oxides of nitrogen are emitted into the atmosphere as nitric oxide and nitrogen dioxide. For traffic emissions the ratio of these two species depends on the type of vehicle and the driving mode. In this study an emission ratio of NO/NO_X of 85% has been used. Figure 5.17 shows the concentration ratio for a vertical cross section across the main street canyon. Near the emission sources in the main street canyon a concentration ratio of near 85% can be seen. Due to the fast chemical reactions between NO₂, NO and background

5. ASSESSMENT OF SIMULATED CONCENTRATIONS

O₃ the concentration ratio quickly changes and at the top of the street canyon a value around 80% can be found.

Surrounding areas have a concentration ratio of 75-85% while above the canopy layer a ratio around 75% prevails. This corresponds to the value from the background concentrations (Figure 5.3).

A mesoscale model without urban canopy representation would be able to consider the emissions in the domain, but it would not resolve the separation of high and low concentrations caused by the increased residence time of emitted species in a street canyon. Because the relevant chemical reactions are highly non-linear this can lead to different concentration ratios also above the canopy layer. Such analyses can be used for upscaling of detailed microscale information for the use in a mesoscale model. In the presented case the corresponding emission ratio for a meso-scale model has to be lower than that used in the micro-scale model.

6 Analysis of shading effects on concentrations

This chapter has been published as:

Grawe, D., Cai, X.-M., Harrison, R. M., 2007. Large eddy simulation of shading effects on NO₂ and O₃ concentrations within an idealised street canyon. *Atmospheric Environment* 41 (34), 7304–7314.
doi: 10.1016/j.atmosenv.2007.05.015

The chapter includes the full manuscript of the published article except for some editorial changes. Layout and numbering have been adapted to the thesis document. The abstract is not included and references and acknowledgements have been integrated into the separate sections of the thesis document.

Xiao-Ming Cai and Roy M. Harrison have contributed ideas to the study design and analysis. Xiao-Ming Cai has supported the initial set-up of the model.

6.1 Introduction

Urban air quality is an important health issue, as an increasing number of people live in urban areas. To develop abatement strategies the actual pollution levels need to be assessed. There are typically legislative requirements for such measurements and the European Union, for example, requires its member states to assess air quality metrics for a number of pollutants within their respective territories according to standards laid out in an EU framework directive (European Communities, 1996) and its daughter directives (European Communities, 1999, 2000). Besides operational measurements, numerical models are proposed as a tool to accomplish the requirements of the directives. For the assessment of air quality within the canopy layer of urban areas, obstacle resolving numerical models are an established technique (Vardoulakis et al., 2003). Increasingly, these models not only account for transport of passive pollutants but also for chemical reactions of the compounds involved (Trukenmüller et al., 2004).

Oxides of nitrogen ($\text{NO}_X = \text{NO}_2 + \text{NO}$) and ozone (O_3) form a set of important pollutants that can efficiently be represented in such models, because they involve only in a small number of chemical reactions with time scales relevant in urban street canyons (Baker et al., 2004; Baik et al., 2007). NO_X is mainly emitted by road traffic with the dominant fraction being nitric oxide (NO) (Carslaw, 2005). This reacts in the presence of ozone (O_3) quickly to form nitrogen dioxide (NO_2). Under sunlit conditions, NO_2 is dissociated back into NO and O_3 . NO_2 and O_3 are both listed in the EU First Daughter Directive (European Communities, 1999) and there are currently many locations in the United Kingdom which exceed the annual mean Limit Value of $40 \mu\text{g}/\text{m}^3 \approx 21 \text{ ppb}$ for NO_2 required to be met by 2010 (Air Quality Expert Group, 2004).

Under typical daytime conditions these reactions quickly reach a quasi-steady state, where NO_2 is formed at the same rate as it is dissociated. The concentrations of NO_2 , NO and O_3 in the steady state depend on the rates of the two reactions involved and hence on the amount of sunlight available. Building configurations in most European cities form street canyons

6. ANALYSIS OF SHADING EFFECTS ON CONCENTRATIONS

where for a significant part of the daytime one side of the street canyon will be shaded, while the other side will be unshaded. This leads to a high spatial variability of different reaction rates for the photolytic dissociation of NO_2 and hence to changes in the concentrations of NO_2 , NO and O_3 . The magnitude of this effect depends on the relative reduction of the photolytic reaction rate in the shaded areas and the extent of these areas. Also traffic emissions and the vertical pollutant flux from the street canyon into the above-roof boundary layer are expected to affect the magnitude of the concentration change. Barlow and Belcher (2002) have investigated the vertical flux of passive tracers out of idealised street canyons into the boundary layer above. Their results show that the flux is governed by the above-roof wind speed and the aspect ratio of canyon height to canyon width (H/W). However, for a well developed boundary layer where the upstream flow is in equilibrium with the urban surface, the dependency on H/W was suggested to be less pronounced. For reactive pollutants, the location of the shaded patches in relation to emission sources and above-roof wind direction, and the upstream concentrations of the pollutant are also expected to influence the shading effect. Finally, heating the ground and building surfaces within the street canyon due to solar radiation may influence the flow field and hence the pollutant dispersion. However, thermal effect on the flow field are still controversial (e.g. Bohnenstengel et al. (2004); Sini et al. (1996)); they have therefore not been investigated in this study.

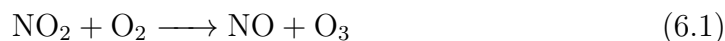
This study employs an obstacle resolving numerical model for an idealised urban street canyon to investigate the effects of local shading on the concentrations of NO_2 and O_3 . In Section 6.2.1 the numerical model used in this study is presented. Sections 6.2.2 and 6.2.3 describe the domain set-up and input parameters for all model simulations. Results of model simulations for different shading configurations, emission and background scenarios and above-canyon wind speed are shown in Section 6.4. Summary and conclusions are given in Section 6.5.

6.2 Method

6.2.1 Model description

The numerical model employed in this study is a large eddy simulation (LES) model initially developed based on the dynamical core of the Regional Atmospheric Model System (RAMS, Pielke et al., 1992). It has since been adapted for the urban canopy layer through the explicit treatment of the effect of building obstacles onto the flow field (Cui et al., 2004). Furthermore it has been extended to include transport and reactions of chemical species by Baker et al. (2004):

The chemistry module introduced into RAMS accounts for reactions between NO_2 , NO and O_3 . Equations 6.1 and 6.2 show the implemented reactions.



In the presence of sunlight, NO_2 is dissociated into NO and O . In an intermediate reaction the latter combines with O_2 to form O_3 (Equation 6.1). The photolysis rate $j(\text{NO}_2)$ for this reaction depends on the amount of sunlight available. Equation 6.2 forms NO_2 from NO and O_3 and is independent of solar radiation. The rate constant k for this reaction depends on the ambient temperature T in K and is given by the Arrhenius equation $k = A \cdot \exp(-E_a R^{-1} T^{-1})$ with $A = 44.05 \text{ s}^{-1} \text{ ppm}^{-1}$ and $E_a R^{-1} = 1370 \text{ K}$. See Baker et al. (2004) for a detailed description of the chemical module. For known initial concentrations of the three species, the ratio of these reaction rates $j(\text{NO}_2)/k$ defines the steady-state concentrations. The deviation from the steady-state can be quantified with the photostationary defect $\delta ps = (k/j(\text{NO}_2) \cdot [\text{NO}] \cdot [\text{O}_3]/[\text{NO}_2] - 1) \cdot 100\%$ (Baker et al., 2004). For chemical equilibrium the photostationary defect vanishes: $\delta ps = 0$.

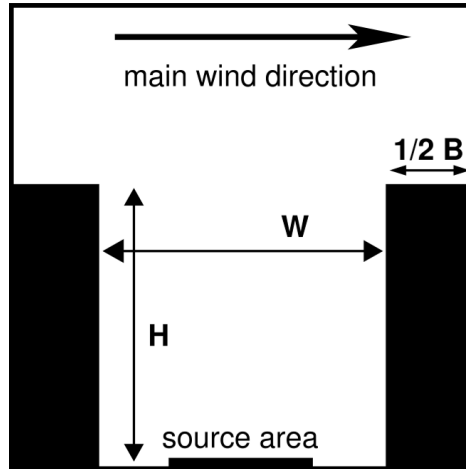


Figure 6.1: Vertical cross section of the model domain. H and W denote the height and width of the canyon, respectively. B is the building width. Also shown are the NO_x source area and the main wind direction above the street canyon.

6.2.2 Model domain

Figure 6.1 shows a vertical cross section of the domain used in the present study. Two buildings of $H = 18$ m height and $B = 6$ m width are located at opposite sides of the domain separated by a street canyon of $W = 18$ m width. A cartesian grid is defined with the x -axis perpendicular to the street-canyon axis, the y -axis parallel to the street canyon and the z -axis in the vertical. The lateral extent of the buildings spans across the complete width L_y of the domain, forming a quasi-two-dimensional regular street canyon with aspect ratio of $H/W = 1$. A horizontal grid resolution of $\Delta x = 0.3$ m is used across the canyon and of $\Delta y = 1.0$ m along the canyon. The vertical grid resolution is $\Delta z = 0.3$ m within the street canyon and increases above the roof level by a factor of 1.15 per grid cell up to a resolution of $\Delta z = 5.0$ m. With these parameters, the actual street canyon is resolved by $60 \times 40 \times 60$ grid cells, while the complete domain comprises of $80 \times 40 \times 90$ cells in x -, y - and z -direction, respectively. This leads to an overall domain height of $L_z = 94.0$ m ($> 5H$), and width and length of $L_x = 24$ m and $L_y = 40$ m, respectively.

6.2.3 Model set-up

The wind field was initialised using a logarithmic profile above the street canyon with a maximum wind speed of $U_{max} = 2.6 \text{ m} \cdot \text{s}^{-1}$ for the reference model run at the model top. The direction of the main flow was perpendicular to the street canyon along the x-axis for all model runs (this is from left to right in all figures). The initial wind speed within the canyon was set to zero. A homogeneous temperature of $T = 293 \text{ K}$ was assumed with neutral stratification. The effect of thermal stratification is not investigated in this study. Based on the maximum wind speed of $2.6 \text{ m} \cdot \text{s}^{-1}$ and the grid resolution of 0.3 m , a time-step of $\Delta t = 0.04 \text{ s}$ was chosen to reduce possible numerical instabilities.

To parameterise eddies which are not explicitly resolved, the Smagorinsky subgrid-viscosity model is used in RAMS. See Cui et al. (2004) for details of the configuration.

Chemical compounds were emitted from an area source located at the bottom of the street canyon, centred between the canyon sides. The source extended over the full canyon length and covered half of the canyon width (Figure 6.1). For the reference model run, NO was emitted at a constant rate of $33.6 \text{ } \mu\text{g/s}$ and NO₂ at a constant rate of $5.1 \text{ } \mu\text{g/s}$.

Cyclic boundary conditions were applied at the lateral boundaries for all wind components. The domain can hence be interpreted as a sequence of an infinite number of infinitely long street canyons. Chemical concentrations were kept at a constant background value at the inflow boundary throughout the model run. At the outflow boundary a radiative boundary condition was used for chemical concentrations to reduce the possibility of artificial reflection.

Each model run had an initialisation phase of 75 min altogether. For the first 30 min no chemical compounds were emitted. After this time the turbulent wind field was well established and a primary canyon vortex had developed. During the following 30 min, NO_x was emitted from the bottom source while chemical reactions were kept deactivated to establish a well mixed concentration field within the canyon in which pollutant emission and venting from the canyon were approximately equal. Emissions were subsequently kept at

the constant rate and chemical reactions were activated. For the reference run, the photolysis rate was set to $j(\text{NO}_2) = 0.008 \text{ s}^{-1}$. The model was run for another 15 min to adjust the concentration field before results were used for interpretation. Each run continued for further 15 min for analysis.

For all model runs with shading the photolysis rate was reduced within the bottom triangular half of the canyon on the windward or leeward side, respectively.

6.3 Model validation

Meroney et al. (1996) and Pavageau and Schatzmann (1999) have conducted wind tunnel experiments to investigate the dispersion in a street canyon with aspect ratio $H/W = 1$. In the experiments, a passive tracer is emitted from a ground level line source at the centre of the street canyon. Vertical concentration profiles of these measurements and results of this numerical model have been compared (Cai et al., 2005). For the comparison, the model set-up was used as described in Sections 6.2.1 – 6.2.3, but the source configuration was adapted to represent the wind tunnel source. A good agreement was found for the leeward side of the canyon (close to the source), and a very good agreement for the windward side.

6.4 Results

The denominations and configuration for all model runs are shown in Tables 6.1 and 6.2. Run LR is the reference run. Note that the photolysis rate for all model runs with shading is given in percent of the value used in the reference run. The initialisation phase of this run is further investigated to ensure validity of the results.

6. ANALYSIS OF SHADING EFFECTS ON CONCENTRATIONS

Name	Emission rate		Background concentration		
	NO (ppb/s/cell ²)	NO ₂ (ppb/s/cell ²)	NO (ppb)	NO ₂ (ppb)	O ₃ (ppb)
LR	100	10	0.0	0.0	20.0
L20LR	100	10	0.0	0.0	20.0
L20RR	100	10	0.0	0.0	20.0
L80RR	100	10	0.0	0.0	20.0
L50RR	100	10	0.0	0.0	20.0
L20RR	100	10	0.0	0.0	20.0
L00RR	100	10	0.0	0.0	20.0
LF	100	10	0.0	0.0	20.0
L20LF	100	10	0.0	0.0	20.0
HR	<u>500</u>	<u>50</u>	0.0	0.0	20.0
H20LR	<u>500</u>	<u>50</u>	0.0	0.0	20.0
LB1	100	10	<u>0.0</u>	<u>0.0</u>	<u>0.0</u>
L20LB1	100	10	<u>0.0</u>	<u>0.0</u>	<u>0.0</u>
LB2	100	10	<u>25.0</u>	<u>25.0</u>	<u>20.0</u>
L20LB2	100	10	<u>25.0</u>	<u>25.0</u>	<u>20.0</u>
LB3	100	10	<u>25.0</u>	<u>25.0</u>	<u>30.0</u>
L20LB3	100	10	<u>25.0</u>	<u>25.0</u>	<u>30.0</u>
LB4	100	10	<u>37.5</u>	<u>25.0</u>	<u>20.0</u>
L20LB4	100	10	<u>37.5</u>	<u>25.0</u>	<u>20.0</u>

Table 6.1: Overview of chemistry settings for each model run. The run LR is referred to as reference run in the text. Underlined text highlights the property investigated with the respective run. Case names contain two segments for runs without shading: L/H for Low/High emission rate, and for further distinction of the investigated property R/B/F for reference setting/background concentration/fast wind. Case names for runs with shading contain two additional segments: a number indicating the reduced photolysis rate and L/R for shading of the left/right side of the canyon.

6.4.1 Analysis of the reference run

Figure 6.2(a) shows the development of the wind speed during the spin-up phase of the reference run. The two curves refer to the wind speed at two near ground locations, one at the windward and the other at the leeward

6. ANALYSIS OF SHADING EFFECTS ON CONCENTRATIONS

Name	Wind speed	$j(\text{NO}_2)$	Shaded section
	(m/s)	(%)	
LR	2.6	100	—
L20LR	2.6	20	Leeward
L20RR	2.6	20	<u>Windward</u>
L80RR	2.6	<u>80</u>	Windward
L50RR	2.6	<u>50</u>	Windward
L20RR	2.6	<u>20</u>	Windward
L00RR	2.6	<u>0</u>	Windward
LF	<u>5.2</u>	100	—
L20LF	<u>5.2</u>	20	Leeward
HR	2.6	100	—
H20LR	2.6	20	Leeward
LB1	2.6	100	—
L20LB1	2.6	20	Leeward
LB2	2.6	100	—
L20LB2	2.6	20	Leeward
LB3	2.6	100	—
L20LB3	2.6	20	Leeward
LB4	2.6	100	—
L20LB4	2.6	20	Leeward

Table 6.2: Overview of meteorology settings for each model run. The run LR is referred to as reference run in the text. The reaction rate constant $j(\text{NO}_2)$ is given in percent of the value used in the reference run. A shading section windward indicates shading of the bottom right triangular half of the street canyon, while a shading section leeward indicates shading of the bottom left triangular half of the street canyon. Underlined text highlights the property investigated with the respective run. For notation of case names see Table 6.1.

side. A primary vortex develops in the street canyon within approximately 10 min. After approximately 30 min all three wind components have reached quasi-stationary conditions where the trend is negligible. A primary vortex has developed in the street canyon with wind speeds of $0.15 \text{ m} \cdot \text{s}^{-1}$ and above near the street canyon sides and hence a turn over time of the vortex is about 3 min. Figure 6.2(b) shows a time series of the domain-averaged

6. ANALYSIS OF SHADING EFFECTS ON CONCENTRATIONS

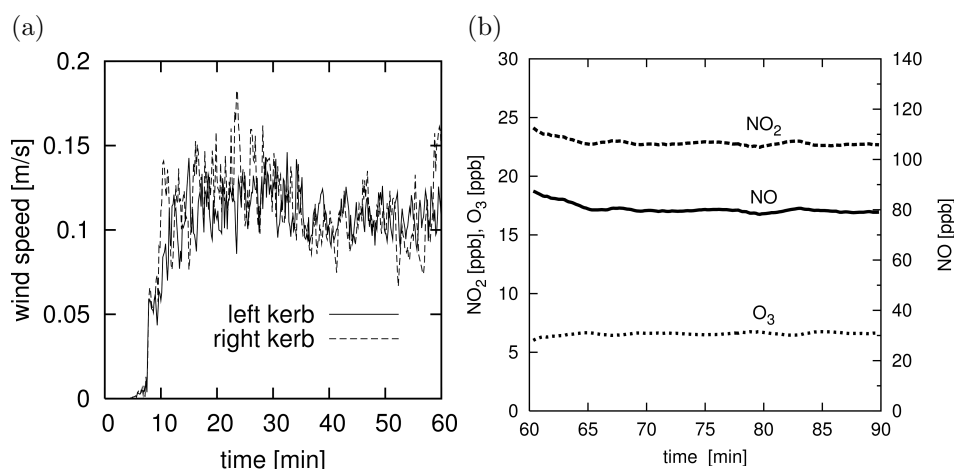


Figure 6.2: (a) Time series of individual wind speed components during the initial 60 min of the reference model run; values are averaged along the street canyon for location $x = -8$ m, $z = 2$ m (left kerb) and $x = 8$ m, $z = 2$ m (right kerb), (b) Time series of chemical concentrations after chemical reactions have been activated; values are averaged for the entire street canyon.

concentrations of all three species after NO_x has been emitted for 30 min and chemical reactions have been activated. It can be seen that all three concentrations adjust to a quasi-stationary state within a few minutes. The period of 75-90 min is subsequently being used for the analysis of all model runs.

Figure 6.3 shows NO_2 and O_3 concentrations for the reference run. For NO_2 , the highest concentrations can be found near the ground level emission sources in the centre of the street canyon and subsequently downwind of this location leading to higher concentrations on the leeward side compared with those on the windward side of the street canyon. NO_2 is then lifted through the primary vortex towards the canyon top, where it mixes with NO_x free air from aloft. Hence, lower concentrations are observed on the windward side of the street canyon. For O_3 , highest concentrations occur at the top of the windward side of the canyon. Here, background O_3 is mixed into the canyon, but vanishes quickly through reaction with the existing NO to form NO_2 as it is transported downwards. Near the emission source at ground level, O_3 is formed from photodissociation of emitted NO_2 , while it is depleted through reaction with emitted NO . The emission ratio of $\text{NO}/\text{NO}_2 = 10/1$ favours the

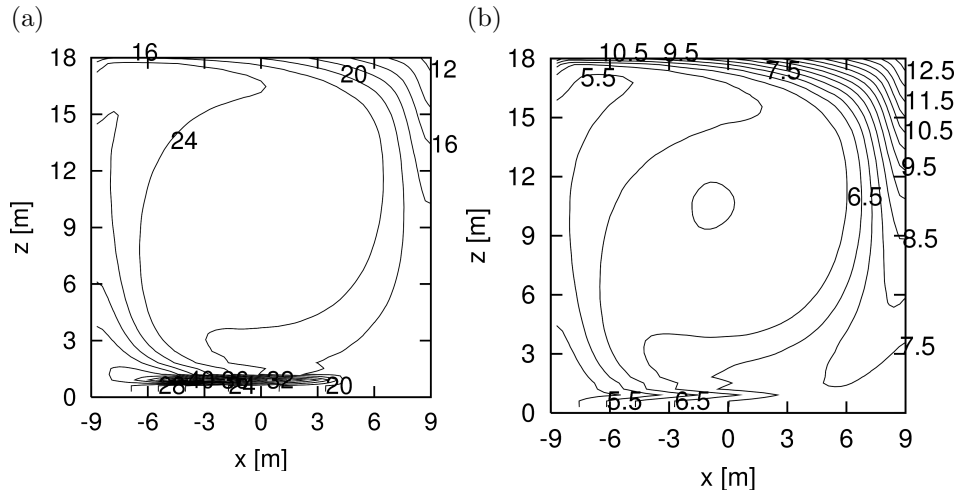


Figure 6.3: (a) NO_2 and (b) O_3 concentrations in (ppb) for the reference model run (LR). The values have been averaged for the analysis period (75-90 min) and along the street canyon axis.

depletion, leading the minimum O_3 concentration near the NO_x emissions.

6.4.2 Effect of shading

Figure 6.4(a) shows the difference of the concentrations between the reference run and L20LR with a photolysis rate of 20% of the original value at the leeward side of the canyon. Compared to the reference run, higher NO_2 concentrations and lower O_3 concentrations occur for the shaded run. This is due to the reduced photodissociation of NO_2 into NO and O_3 (Equation 6.1). Following the path of the primary vortex in the street canyon, NO_2 concentrations are increased as soon as the shaded area has been reached. The differences then grow in magnitude while the air moves through the shaded section and reach a maximum of above 3.6 ppb close to the canyon top. Coming into the unshaded area at the canyon top, the differences are quickly reduced, as photo-dissociation increases again. This effect is further enhanced through mixing of air from above the canyon into the canyon. For O_3 the effect is very similar in magnitude and spatial pattern. However, the sign of the difference is opposite. The concentrations are reduced when compared to the reference run since the shading suppresses the production of

O₃. The spatial extend is broadly limited to the shaded area for both species. Substantial shading differences of 1.5 ppb and above are found throughout the complete shaded area and with limited extent in the unshaded area at the model top.

6.4.3 Influence of the shading geometry

Figure 6.4(b) shows the differences for NO₂ and O₃ concentrations when the windward side of the canyon is shaded. (This has an identical set-up as for the results shown in Figure 6.4(a), but with shading of the opposite side.) Following the concentrations along the primary street canyon vortex, for shading of the windward side NO₂ concentrations are reduced as soon as the shaded section is reached. The differences then increase as the air travels downward in the shaded area and reaches a maximum of 3.8 ppb near the bottom. In the bottom centre of the canyon however, the effect is reduced by local emissions of NO_x. Here, the emission lead to high concentration gradients, so that the steady-state cannot be reached at this location. Hence, the effect induced by the shading is distributed over a larger area.

Reaching the unshaded section of the canyon, the differences are quickly reduced, but still extend with values above 2 ppb for the bottom 5 m. The effect for O₃ is the same, but with opposite sign. Compared to Figure 6.4(a), the behaviour is very similar. However, when the windward side is shaded maximal differences occur close to the ground, while for shading the leeward side the maximum occurs at the canyon top and the differences at the bottom are substantially lower (up to 3.0 ppb compared to up to 3.8 ppb).

6.4.4 Influence of the wind speed

Figure 6.4(c) shows the shading effect on NO₂ and O₃ concentrations for model runs with increased wind speed. O₃ concentrations are again reduced in this case as the flow reaches the shaded area, while NO₂ concentrations are increased. The maximal difference reached at the top of the shaded area is 3.6 ppb for both, NO₂ and O₃. However, due to increased wind speed the

6. ANALYSIS OF SHADING EFFECTS ON CONCENTRATIONS

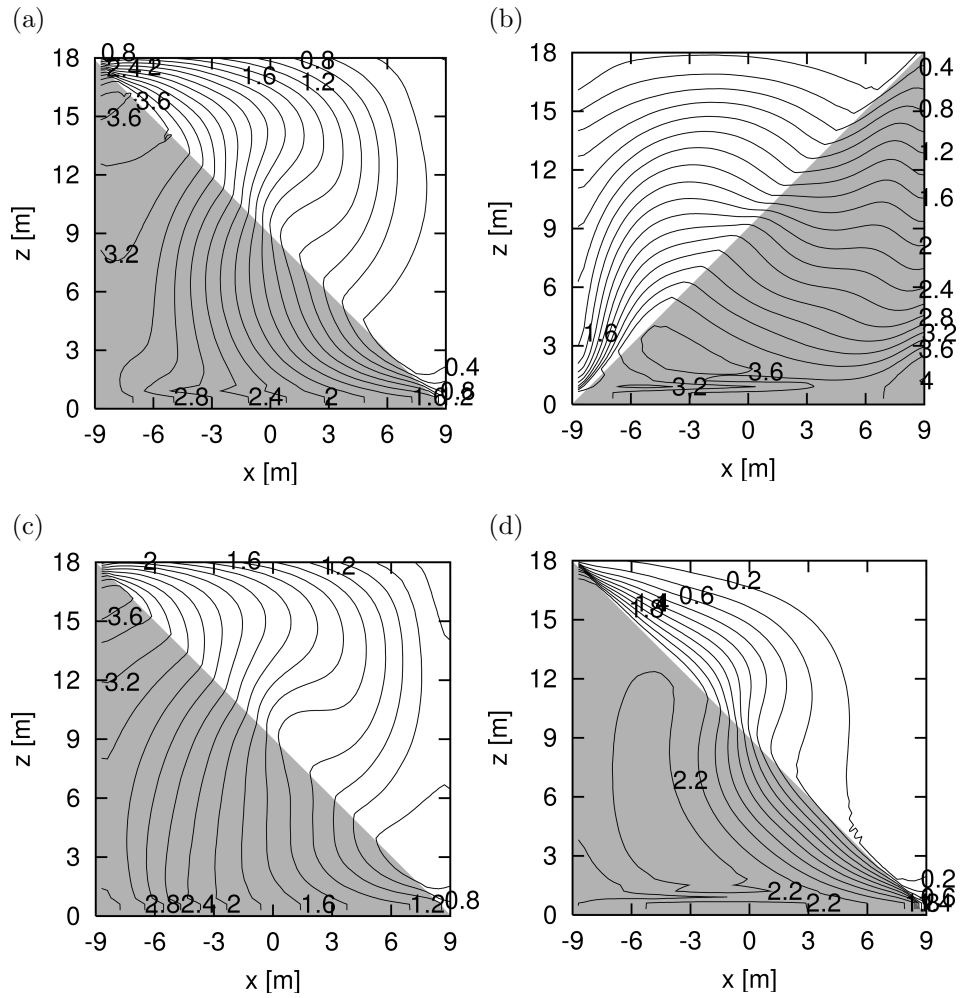


Figure 6.4: Magnitude of differences for NO_2 and O_3 concentrations in (ppb) for (a) $|\text{LR} - \text{L20LR}|$, (b) $|\text{LR} - \text{L20RR}|$, (c) $|\text{HR} - \text{H20LR}|$, (d) $|\text{LF} - \text{L20L}|$. All values have been averaged for the analysis period (75-90 min) and along the street canyon axis. Actual differences due to shading are increases for NO_2 and decreases for O_3 . The shaded triangle indicates the shaded section of the street canyon.

whole canyon is more efficiently mixed between shaded and unshaded areas. Compared to the reference case with lower wind speed (Figure 6.4(a)) the differences are reduced at the bottom of the street canyon but increased at the top. Within the time required for the photolysis reduction by the shading to take effect, the air has travelled further within the primary vortex in the canyon. Hence the pattern of a clear distinction of shaded and unshaded areas obvious in all other cases is less pronounced in this case, where a gradient from the windward to the leeward side of the canyon can be observed.

6.4.5 Influence of the emission rate

For an unshaded model run with increased NO_x emissions (HR), NO_2 concentrations are substantially increased in the street canyon, while ozone concentrations are reduced significantly. While the reference run with low emissions leads to ozone concentrations of 5.0-6.5 ppb downwind of the source (compare Figure 6.3(b)), the concentrations for high emissions are 2.5-3.5 ppb. Figure 6.4(d) shows the differences of NO_2 and O_3 concentrations due to shading when higher NO_x emissions occur. Compared to Figure 6.4(a), the shading effect is reduced for this case. Maximal differences of 2.2 ppb are found close to the source and the influence on the unshaded area is much smaller in magnitude and in spatial extent. Sufficient O_3 needs to be available for the shading to have an effect. Both, higher emissions and shading reduce the O_3 concentration, thereby reducing the shading effect in this case.

6.4.6 Influence of the shading magnitude

Figure 6.5 shows the difference of NO_2 and O_3 concentrations for different values of the photolysis rate in the shaded area at the leeward side of the canyon. The differences suggest a near linear relation to the amount of shading for all locations shown. This implies that due to the fast reactions involved, the reduction is dominated by the change in the photolysis rate, while processes that could introduce non-linear effects are less important.

6. ANALYSIS OF SHADING EFFECTS ON CONCENTRATIONS

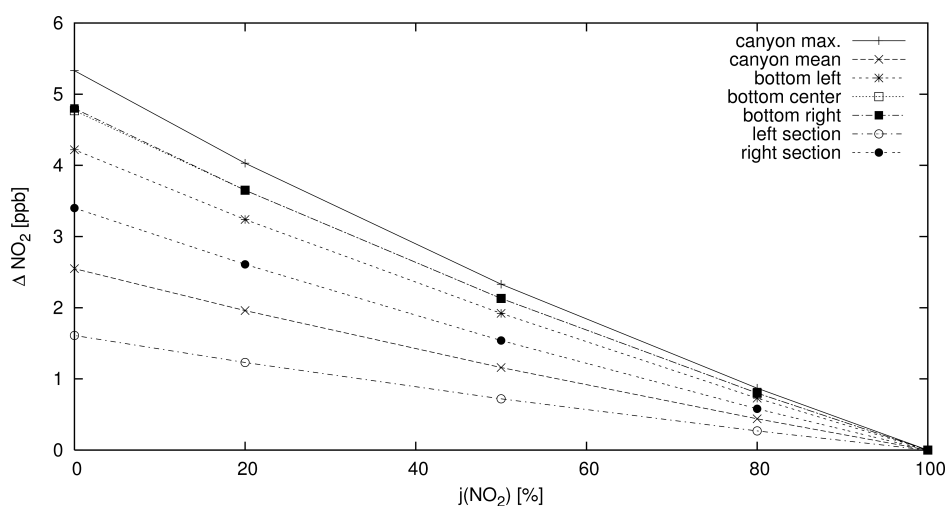


Figure 6.5: Magnitude of differences for NO_2 and O_3 concentrations for different values of the photolysis rate on the shaded area. The photolysis rate is shown in percent of the value used for the reference run. The difference is shown for different points and for different spatial averages (maximum value within the canyon; average value throughout the canyon; bottom values 2m above the ground at the left, centre and right side of the canyon; and the bottom left and right triangular sections, respectively). Actual differences due to shading are increases for NO_2 and decreases for O_3 .

6.4.7 Influence of the background concentration

Four scenarios with different background concentrations have been investigated. The runs can be characterised with the photostationary defect δps of the background concentration field:

$$\begin{aligned}\delta ps(\text{LB1}) & \quad \text{is not defined,} \\ \delta ps(\text{LB2}) & = 2.6\%, \\ \delta ps(\text{LB3}) & = 54\%(\text{with excess O}_3), \\ \delta ps(\text{LB4}) & = 54\%(\text{with excess NO}).\end{aligned}$$

The lower O₃ background concentration in LB1 leads to lower concentrations of O₃ throughout the street canyon, since only O₃ from locally photodissociated NO₂ is available. Figure 6.6(a) shows the subsequently altered shading effect. Within the shaded area O₃ concentrations are reduced by up to 2.8 ppb by shading in the street canyon, while NO₂ concentrations are increased by the same magnitude. In comparison with higher background concentrations (Figure 6.4(a)) this is a reduced shading effect. This is caused by a similar mechanism as outlined in Section 6.4.5: Less O₃ is available due to reduced background concentrations, hence the reduction of O₃ is limited and subsequently the increase of NO₂.

For all runs with increased background concentrations of NO_x (LB2/B3/B4), higher concentrations of NO₂ can be found in the street canyon. While for the reference run maximum concentrations of 40 ppb occur near the emission source, runs with higher background concentrations reach maximum concentrations of 56-62 ppb at the same location. For the same model runs an overall increase of ozone of 1-2 ppb can also be observed throughout the street canyon compared to the reference run. For the run with in addition increased ozone background concentration (LB3), street canyon concentrations of ozone are increased by additional 2-4 ppb. Figures 6.6(b), 6.6(c) and 6.6(d) show the shading effect for runs with increased background concentrations. The results show the same spatial patterns as for runs with lower background concentrations. However, the magnitude of differences is increased in all cases. The largest increase can be found for the case with

6. ANALYSIS OF SHADING EFFECTS ON CONCENTRATIONS

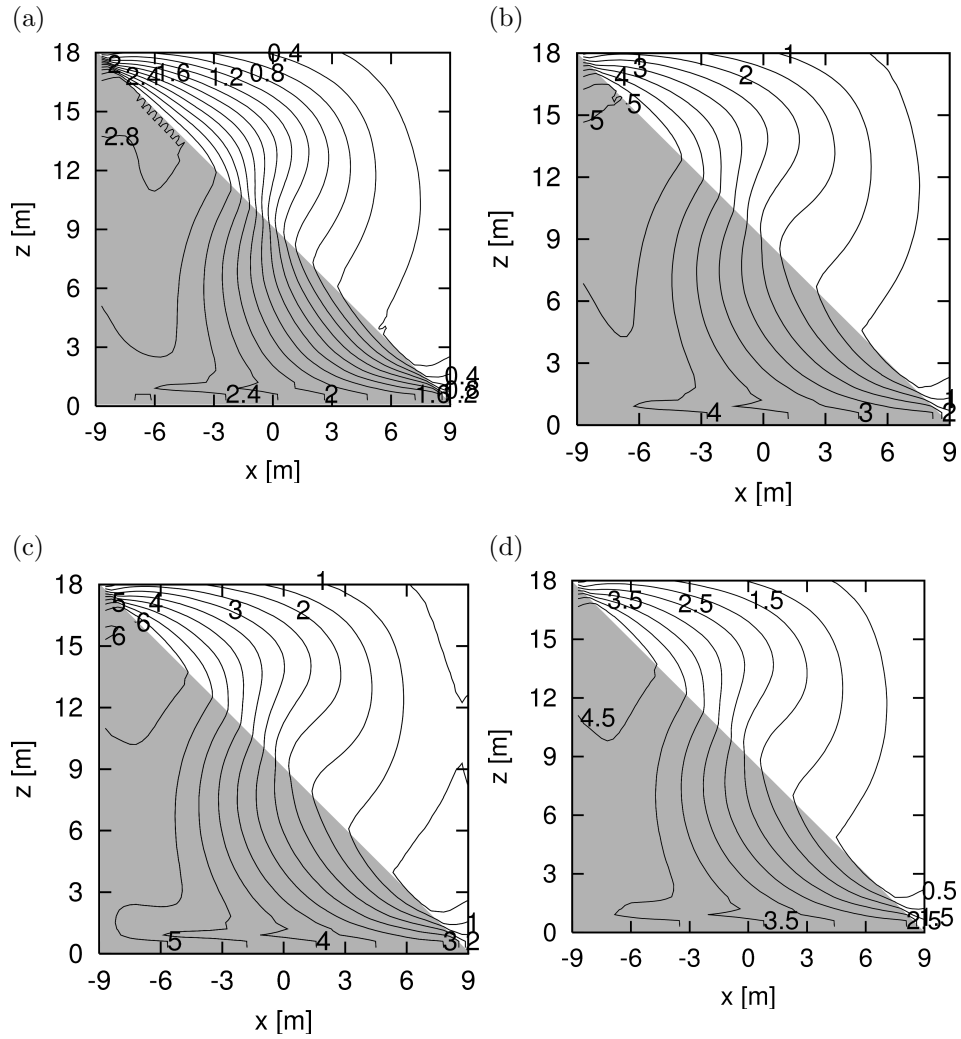


Figure 6.6: Magnitude of differences for NO₂ and O₃ concentrations in (ppb) for (a) |LB1 - L20LB1|, (b) |LB2 - L20LB2|, (c) |LB3 - L20LB3|, (d) |LB4 - L20LB4|. All values have been averaged for the analysis period (75-90 min) and along the street canyon axis. Actual differences due to shading are increases for NO₂ and decreases for O₃. The shaded triangle indicates the shaded section of the street canyon.

increased ozone and nitrogen oxides, while both cases with only nitrogen oxides concentrations increased still show a larger effect than cases with lower background concentrations.

6.5 Summary and conclusions

A summary of results for all model runs is shown in Table 6.3. The magnitude of differences is identical for NO_2 and O_3 within the precision of the values in the table, hence only one value is shown for each result. It can be seen from the table that the shading magnitude has a very strong effect on the differences found. A nearly linear dependence of the differences on the magnitude of the reduction of the reaction rate constant $j(\text{NO}_2)$ has been found. Also a strong influence could be observed for the chemical regime upstream of the street canyon. The more excess ozone is left after mixing into the street canyon the higher the magnitude of the shading effect. Lower ozone background concentrations limit the amount of ozone available to form nitrogen dioxide and hence decrease the shading effect. For different geometries of the shaded area, shading of the windward side of the canyon leads to higher differences than shading of the leeward side especially near the ground, where a strong reduction can be found across the whole width of the canyon. The wind speed has been found to affect the shading through mixing within the street canyon. Higher wind speeds lead to enhanced mixing and hence change the spatial distribution rather than the magnitude of the shading effect. Thermal influence on the flow field due to surface heating by solar radiation has not been explicitly investigated in this study. However, Sini et al. (1996) suggest that heating on the surface on the leeward side (i.e. shading of the windward side merely changes the intensity of the primary vortex. It may be concluded that in analogy to changes of the wind speed the effect is a change of the spatial distribution rather than in magnitude.

For reaction rates of 20% in the shaded area compared to the unshaded area, NO_2 concentrations are increased by up to 6.2 ppb for the cases investigated in this study and by up to 4.9 ppb for near ground locations where pedestrians or sampling sites would be located. Considering that on an overcast day,

6. ANALYSIS OF SHADING EFFECTS ON CONCENTRATIONS

the photolysis rate for NO_2 can already be 20–30% of the theoretical value (Finlayson-Pitts and Pitts, 2000), this magnitude of shading does not seem unrealistic. The effect found is substantial compared to the EU limit value for NO_2 of 21 ppb (European Communities, 1999). With an hourly EU Limit Value of $200 \mu\text{g}/\text{m}^3 \approx 105 \text{ ppb}$ for NO_2 , the shading effect is expected to be most important in areas where local shading strongly affects the conditions for a substantial part of the year, e.g. areas with mainly clear sky conditions and narrow street canyons. Especially in these areas, local shading should be taken into account for numerical model runs and should also be considered when sampling sites are set up.

Effect	Difference	Max	Mean			Point		
			All	Left	Right	Left	Middle	Right
Base	LR – L20LR	3.8	1.8	2.3	2.5	3.0	2.1	0.5
Geom.	LR – L20RR	4.0	2.0	1.2	2.6	3.2	3.7	3.7
Magn.	LR – L80RR	0.9	0.4	0.3	0.6	0.7	0.8	0.8
	LR – L50RR	2.3	1.2	0.7	1.5	1.9	2.1	2.1
	LR – L20RR	4.0	2.0	1.2	2.6	3.2	3.7	3.7
	LR – L00RR	5.3	2.6	1.6	3.4	4.2	4.8	4.8
Wind	LF – L20LF	3.8	1.8	2.4	2.2	2.8	1.6	0.6
Rate	HR – H20LR	2.6	1.1	1.3	2.0	2.0	2.2	0.5
Conc.	LB1 – L20LB1	3.2	1.4	1.9	2.2	2.5	2.1	0.4
	LB2 – L20LB2	5.3	2.5	3.2	3.6	4.3	3.3	0.8
	LB3 – L20LB3	6.2	2.9	3.8	4.2	4.9	3.9	0.9
	LB4 – L20LB4	5.1	2.4	3.1	3.5	4.1	3.3	0.8

Table 6.3: Overview of results for all model runs for different locations. Values show the absolute difference in NO_2 and O_3 concentrations (ppb), averaged for the analysis period (75–90 min). Actual differences due to shading are increases for NO_2 and decreases for O_3 . (Max: highest difference in the canyon; Mean All/Left/Right: average difference in the complete canyon, and the lower left and right triangular half of the canyon, respectively; Point Left/Right/Middle: difference at the point 2 m above ground and 2 m from the left and right building wall and at the centre of the canyon, respectively.)

7 Conclusions

This thesis has investigated the spatial representativeness of air quality assessment either with a numerical model or for measurements. The EU requires that air quality at hot-spot locations have a spatial representativeness of 100 m along the street. In order to fulfil this representativeness, foremost, such an area needs to exist. If air quality data varies highly across any stretch of 100 m then this requirement cannot be readily fulfilled. A solution could be to determine an average concentration that matches the average across the representative stretch along the road. Further than just fulfilling a geometric spatial requirement, the obtained data has to be evaluated in order to ensure that the values are also realistic. A wrong value in the right resolution cannot be representative. Chapter 5 has shown that this evaluation needs to include the full technique to determine pollutant concentrations and not just the model itself. If a bias occurs in relevant input data, the output of the model can be expected to be similarly affected. Determining the input data such as background concentrations and approach flow wind direction with a consistent larger scale model will be helpful to new limit deviations. But in this case the larger scale model has to be included in the evaluation.

Instead of providing the air quality assessment directly, models can also be used to support the placement of sampling sites. The model can determine the spatial variability and help to detect an area with lower variability. It can also help to avoid systematic errors from inconsiderate placement of sampling sites. Chapter 6 has shown that systematic shading of one side of a street canyon can yield noticeably different concentrations. Therefore, placement of a sampling site on a systematically more shaded pavement can hardly be representative for the opposite site of the street.

This thesis has also presented results of the model MICTM to assess concentrations in the urban canopy layer in high resolution. MICTM uses MITRAS wind fields to calculate chemical transport and dispersion. Both components are closely related to their sister models METRAS, and MECTM. Within M-SYS the microscale meteorology model MITRAS and its mesoscale sister model METRAS provide meteorology fields for the chemistry components, MECTM for mesoscale and MICTM for microscale applications. Both chemistry models employ the same set of chemical reactions in order to enable consistent nesting of the microscale model into the mesoscale model results. The employed chemistry mechanism RADM2 has originally been developed for regional applications. Here it is for the first time used for urban microscale applications.

Both components, MITRAS and MICTM, have been evaluated by comparison with measured data. The evaluation of MITRAS followed the corresponding guideline for microscale obstacle resolving wind field models of The Association of German Engineers (VDI, 2005). It requires the model to pass a selection of idealised test cases in comparison to wind tunnel data. For this thesis the evaluation approach was extended and performed for realistic test cases. The performance criteria of the guideline and for the additional realistic test case were all passed by MITRAS. MICTM results were also compared to wind tunnel data for a similar set-up with passive tracer concentrations. To test the results of chemical reactions, the predicted concentrations for a case were also compared to field measurements at several sites in one domain. The comparison of microscale concentrations for passive tracer was within the expected differences. Where higher differences were found they could be attributed to slight differences in the set-up. The comparison with field measurements showed a good agreement with measured data for carbon monoxide, a substance involved in relatively slow reactions. The comparison for more reactive species highlighted the relevance of good quality background information. All concentration differences were consistent with a somehow too low background concentration of ozone. As a consequence concentrations of nitric oxide were high compared to the measurements and nitrogen dioxide was low.

7. CONCLUSIONS

Concentrations in the urban canopy layer are highly variable and depend on influences from different scales. Large-scale weather conditions and background concentrations affect urban canopy concentrations as well as concentrations at urban background sites. Particularly in the urban canopy layer a plethora of further influences affect the level and variability of concentrations. Due to buildings and other obstacles the flow field is very variable and recirculation zones around buildings exist and interact with each other to form complex dispersion conditions. Within the urban canopy layer, any assessment of concentrations will be in the vicinity of local sources which are associated with high concentration gradients. A further analysis of concentration results for the realistic test case has highlighted the low spatial representativeness of an actual measurement site in the main street canyon. Although a large area exists parallel to the street axis for which similar concentrations are predicted, a shift of the measurement site by few metres in the across canyon direction would yield concentration differences by up to a factor of 5.

In order to investigate the influence of further parameters of the model, a sensitivity study with a simplified model has been performed which quantified the impact of differential shading on chemical reactions in a street canyon. The street canyon was designed as an idealised version of the main street canyon in the realistic test case. The study has shown that roadside concentrations in a partially shaded street canyon could differ substantially between the shaded side and the sunlit side of the canyon. Shading in the street canyon leads to lower concentrations of ozone and higher concentrations of nitrogen dioxide. The differences are not limited to the shaded area, but particularly for shading of the windward side the impact extends throughout the street canyon. The magnitude of the concentration impact depends on the magnitude of the shading, but can reach substantial values compared to the annual limit value of nitrogen dioxide, but is low in comparison with the short-term limit value. Therefore, shading should be included in cases where shading occurs for a substantial part of the year.

It is clear from the results that the quality of input data matters and the influence of e.g. background concentration has been shown. Of similar im-

portance is e.g. the emission modelling. In this project high quality emission data was provided based on a sample of cars in the street at the time of the measurements. But usually traffic emission are parameterised based on activities that represent statistics of the non-deterministic behaviour of human agents. It has to be noted that concentrations with high temporal and spatial resolution are only possible with equally high-quality emission data. The more processes are considered relevant the more quality assurance of input data has to be made.

These results are relevant for the application of numerical models, but they are also helpful for the placement of measurement sites. An assessment of the representativeness of measurement sites should be performed so that the measurements can be placed in a location where the variability is limited. This should avoid local recirculation zones that do not represent the whole street canyon, or proximity to emission sources.

The obstacle resolving models presented in this thesis have been used to demonstrate the impact of in-canyon emissions on the levels of air pollution. If the model resolves the urban canopy layer, areas with low concentrations such as courtyards are separated from areas with high concentration such as streets due to an increased residence time of the air. If the urban canopy layer is not explicitly resolved the emitted pollutants can mix more readily. Because the relevant chemical reactions are highly non-linear, the delayed mixing can lead to more realistic concentrations even beyond a particular street canyon.

The computational requirements for MICTM are fairly high due to the high number of chemical reactions calculated. This is particular true in situations where the time-slice approach cannot be used. It may be feasible to replace this by a somehow further reduced mechanism (e.g. VDI (2017a)) to reduce the computational requirement. In order to avoid deviations from nesting between different chemical mechanisms, this set of equations should then also be used to calculate mesoscale boundary values. To replace the complex set of reactions with a simple steady-state relation would be inadvisable. Slower reactions that form O_3 from VOCs do occur, even if at lower time scales. With ever increasing computing power the numerical domains may

7. CONCLUSIONS

also become larger thereby increasing the residence time of pollutant and requiring somehow more complex chemical reactions.

Acknowledgements

First and foremost I would like to thank Prof. K. Heinke Schlünzen for the suggestion and the possibility to work on this topic. I am very grateful for the persistent support and belief throughout the preparation of this dissertation. Danke, Heinke.

Thank you to Prof. Bernd Leitl for acting as a co–advisor.

The framework for this work was the project VALIUM and I would like to thank all project partners for their support, particularly all those who provided necessary data for the microscale modelling.

Many fruitful discussions in the weekly MeMi group meeting provided a useful environment for this thesis. As did regular meetings in the wind tunnel workshop. And the bridge lunch at CSIRO.

Many thanks to Karsten and Frauke for editing this document on short notice.

I would not have managed to finish this thesis without the untiring effort of Frauke in running the family over many weeks with help from my parents and my sister. Danke, Frauke. I was just putting words and numbers together. The real effort was yours. Danke, Annette, Ditmar und Sarah.

And finally, I would like to apologise to my children Eric, Piet & Carl, who could not understand my continued absence. But on a fundamental level, you got me to finish this. Danke.

The work for Chapters 4 and 5 has been funded by the German Ministry for

7. CONCLUSIONS

Education and Research (BMBF) through the Atmospheric Research Programme AFO2000. Wind tunnel comparison data were kindly provided by Environmental Wind Tunnel Laboratory (EWTL) of the University of Hamburg. Emission data were provided by Jörg Kühlwein of IER, University of Stuttgart. The work for Chapter 6 was funded by the Natural Environmental Research Council (NERC) within the National Centre for Atmospheric Sciences (NCAS). The numerical code was provided by Dr Craig Tremback of ATMET.

A Concentration units

Chemical concentrations can be given in mass concentrations or number concentrations. Regulatory limit values are mostly prescribed in mass concentrations with units of $\mu\text{g}/\text{m}^3$. However, from the calculation of chemical conversion number concentrations may be more relevant as chemical conversion occurs based on number concentrations. In this thesis both units are used depending on the purpose. The conversion is described in DEFRA (2005). Number concentrations can be converted to mass concentrations according to

$$C_{mass} = C_{number} \cdot M_{mol}/V_{mol} \quad (\text{A.1})$$

where C_{mass} is the mass concentration given in $\mu\text{g}/\text{m}^3$ and C_{number} is the number concentration in ppb. M_{mol} is the molar mass of the converted species and V_{mol} is the molar volume. The table shows the molar weight of some species and the resulting conversion factor at air pressure of 1013 hPa and temperature of 20 °C with $V_{mol} = 24.0 \text{ g/l}$:

Species	Molar mass (g/mol)	M_{mol}/V_{mol} (g/l)
NO ₂	46	1.91
NO	30	1.25
O ₃	48	2.00
CO	28	1.16

B Chemistry mechanism in MICTM

B.1 List of chemical species in MICTM

The chemical species considered in MICTM are reproduced here from Trukenmüller et al. (2004) and Stockwell et al. (1990).

Number	Molecular formula	MICTM name	Name of species
1	NO ₂	NO2	Nitrogen dioxide
2	NO	NO	Nitric oxide
3	O ₃	O3	Ozone
4	HONO	HONO	Nitrous acid
5	HNO ₃	HNO3	Nitric acid
6	HNO ₄	HNO4	Pernitric acid
7	NO ₃	NO3	Nitrogen trioxide
8	H ₂ O ₂	H2O2	Hydrogen peroxide
9	HCHO	HCHO	Formaldehyde
10	CO	CO	Carbon monoxide
11	ALD	ALD	Acetaldehyde
12	CH ₃ OOH	OP1	Methyl hydrogen peroxide
13	RO ₂ H	OP2	Higher organic peroxides
14	CH ₃ (CO)OOH	PAA	Peroxyacetic acid and higher analogues
15	CH ₃ COCH ₃ [§]	KET	Ketones

continued on next page

[§]and other similar species

B. CHEMISTRY MECHANISM IN MICTM

continued from last page

Number	Molecular formula	MICTM name	Name of species
16	OHC – CHO	GLY	Glyoxal
17	CH ₃ COCCHO	MGLY	Methylglygloxal and other aldehydes
18	R – (CHO) ₂	DCB	Unsaturated dicarbonyls
19	R – ONO ₂	ONIT	Organic nitrate
20	N ₂ O ₅	N2O5	Dinitrogen pentoxide
21	SO ₂	SO2	Sulphur dioxide
22	H ₂ SO ₄	SULF	Sulfuric acid
23	CH ₄	CH4	Methane
24	C ₂ H ₆	ETH	Ethane
25	C ₃ H ₈ [§]	HC3	Alkanes C3-C5
26	C ₇ H ₁₆ [§]	HC5	Alkanes C6-C8
27	C _n H _{2n+2} [§]	HC8	Alkanes C10 and higher
28	C ₂ H ₄	OL2	Ethene
29	C _n H _{2n} [§]	OLT	Terminal alkanes
30	C _n H _{2n} [§]	OLI	Internal alkanes
31	C _n H _{2n} [§]	TOL	Toluene and less reactive aromatics
32	HOC ₆ H ₄ CH ₃ [§]	CSL	Cresol and other hydroxy substituted
33	C ₆ H ₄ (CH ₃) ₂ [§]	XYL	Xylene and more reactive aromatics
34	CH ₃ C(O) ₂ NO ₂ [§]	PAN	Peroxyacetyl nitrate and higher saturated PANs
35	C ₅ H ₈	ISO	Isoprene
36	CHOCH = CHC(O)O ₂ NO ₂	TPAN	Unsaturated PANs
37	HCOOH	ORA1	Formic acid
38	CH ₃ COOH [§]	ORA2	Acetic acid and higher acids
39	HO ₂	HO2	Hydroperoxy radical

continued on next page

B. CHEMISTRY MECHANISM IN MICTM

continued from last page

Number	Molecular formula	MICTM name	Name of species
40	MO ₂	MO2	Methyl peroxy radical
41	OLN	OLN	NO ₃ -alkene adduct radicals
42	ACO ₃	ACO3	Acetyl peroxy and higher saturated acyl peroxy radicals
43	TCO ₃	TCO3	Unsaturated acyl peroxy radicals
44	HO	HO	Hydroxy radical
45	ETHP	ETHP	Peroxy radical formed from ETH
46	HC ₃ P	HC3P	Peroxy radical formed from HC3
47		HC5P	Peroxy radical formed from HC5
48		HC8P	Peroxy radical formed from HC8
49		OL2P	Peroxy radical formed from OL2
50		OLPT	Peroxy radical formed from OLT
51		OLIP	Peroxy radical formed from OLI
52		TOLP	Peroxy radical formed from TOL
53		XYLP	Peroxy radical formed from XYL
54		KETP	Peroxy radical formed from KET
55	XNO ₂	XNO2	Additional NO to NO ₂ conversions
56	XO ₂	XO2	Additional HO to HO ₂ conversions
57	NH ₃	NH3	Ammonia
58	HCl	HCl	Hydrochlorid acid
59	NH ₄ NO ₃	NH4NO3	Ammonium nitrate

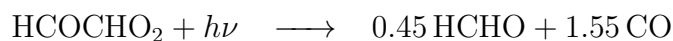
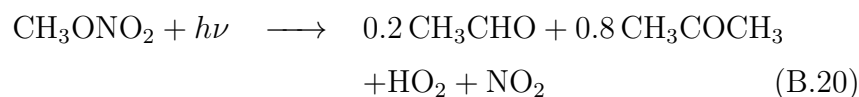
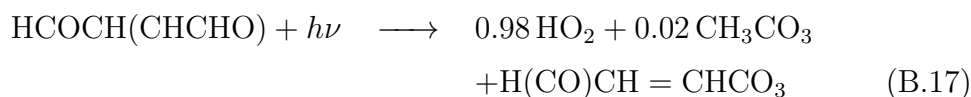
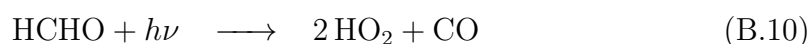
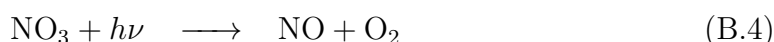
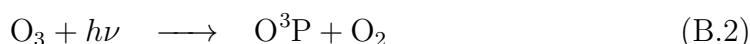
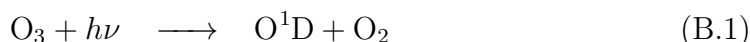
B.2 Emissions

The emission species required in MICTM are reproduced here from Trukenmüller et al. (2004) and Stockwell et al. (1990).

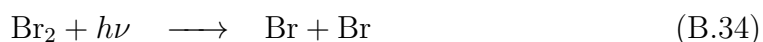
Number	Species
1	SO ₂ Sulphur dioxide
2	NO ₂ Nitrogen dioxide
3	NO Nitric oxide
4	CO Carbon monoxide
5	ALD Acetaldehyde
6	HCHO Formaldehyde
7	ORA ₂ Acetic acid and higher acids
8	HC ₃ Alkanes, alcohols, esters and alkynes with HO rate constant less than $3.4 \cdot 10^{-12} \text{cm}^3 \text{s}^{-1}$
9	HC ₅ Alkanes, alcohols, esters and alkynes with HO rate constant between $3.4 \cdot 10^{-12} \text{cm}^3 \text{s}^{-1}$ and $6.8 \cdot 10^{-12} \text{cm}^3 \text{s}^{-1}$
10	HC ₈ Alkanes, alcohols, esters and alkynes with HO rate constant greater than $6.8 \cdot 10^{-12} \text{cm}^3 \text{s}^{-1}$
11	ETH Ethane
12	OL ₂ Ethene
13	OLT Terminal alkanes
14	OLI Internal alkanes
15	TOL Toluene and less reactive aromatics
16	XYL Xylene and more reactive aromatics
17	KET Ketones
18	CSL Cresol and other hydroxy substituted aromatics
19	NH ₃ Ammonia
20	CH ₄ Methane

B.3 Calculation of photolysis rates (STAR)

The photolytic reactions considered in STAR are reproduced here from Ruggaber (1994) and Ruggaber and Dlugi (1994).

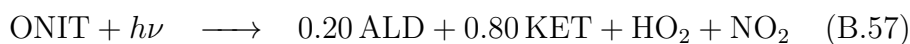
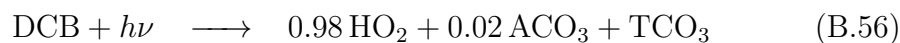
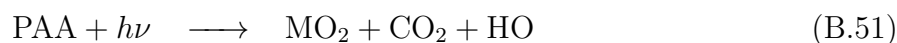
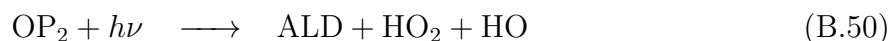
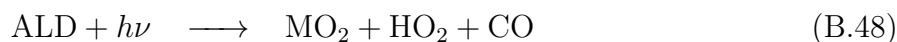
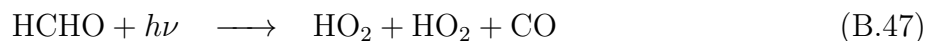
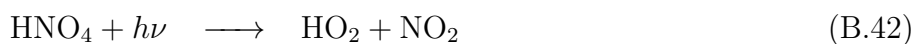
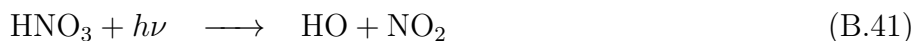


B. CHEMISTRY MECHANISM IN MICTM



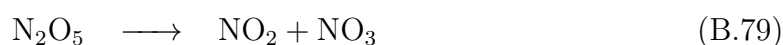
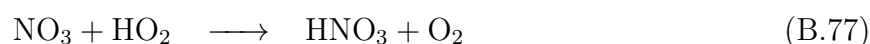
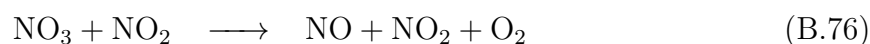
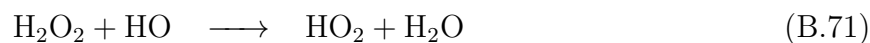
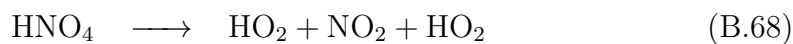
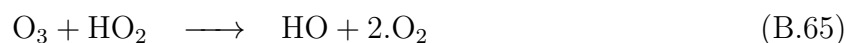
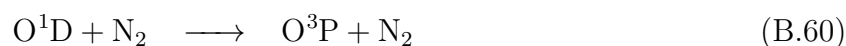
B.4 First order (photolytic) reactions

The first order photolysis reactions employed in MICTM are reproduced here from Trukenmüller et al. (2004) and Stockwell et al. (1990).

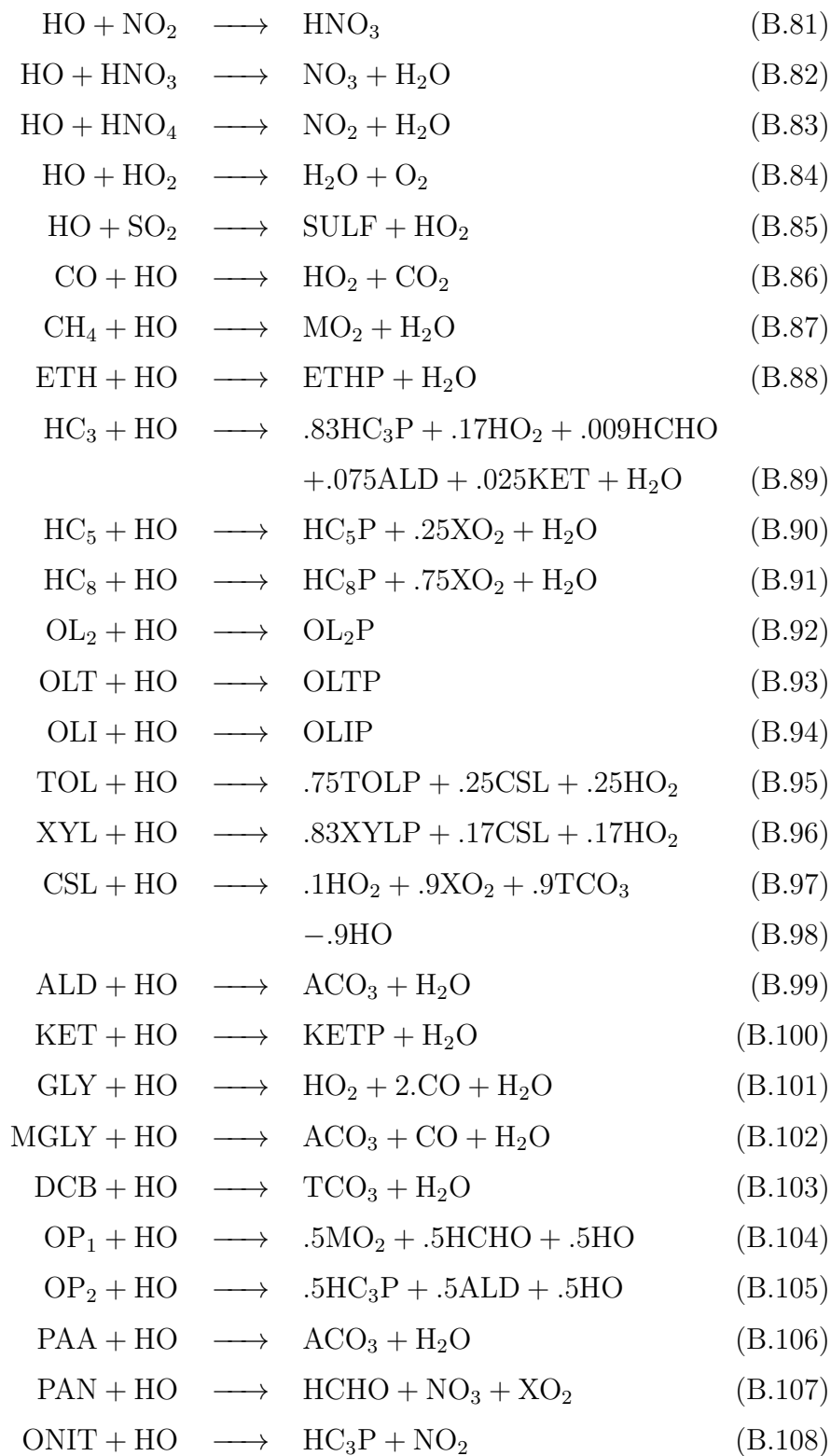


B.5 Higher order chemical reactions

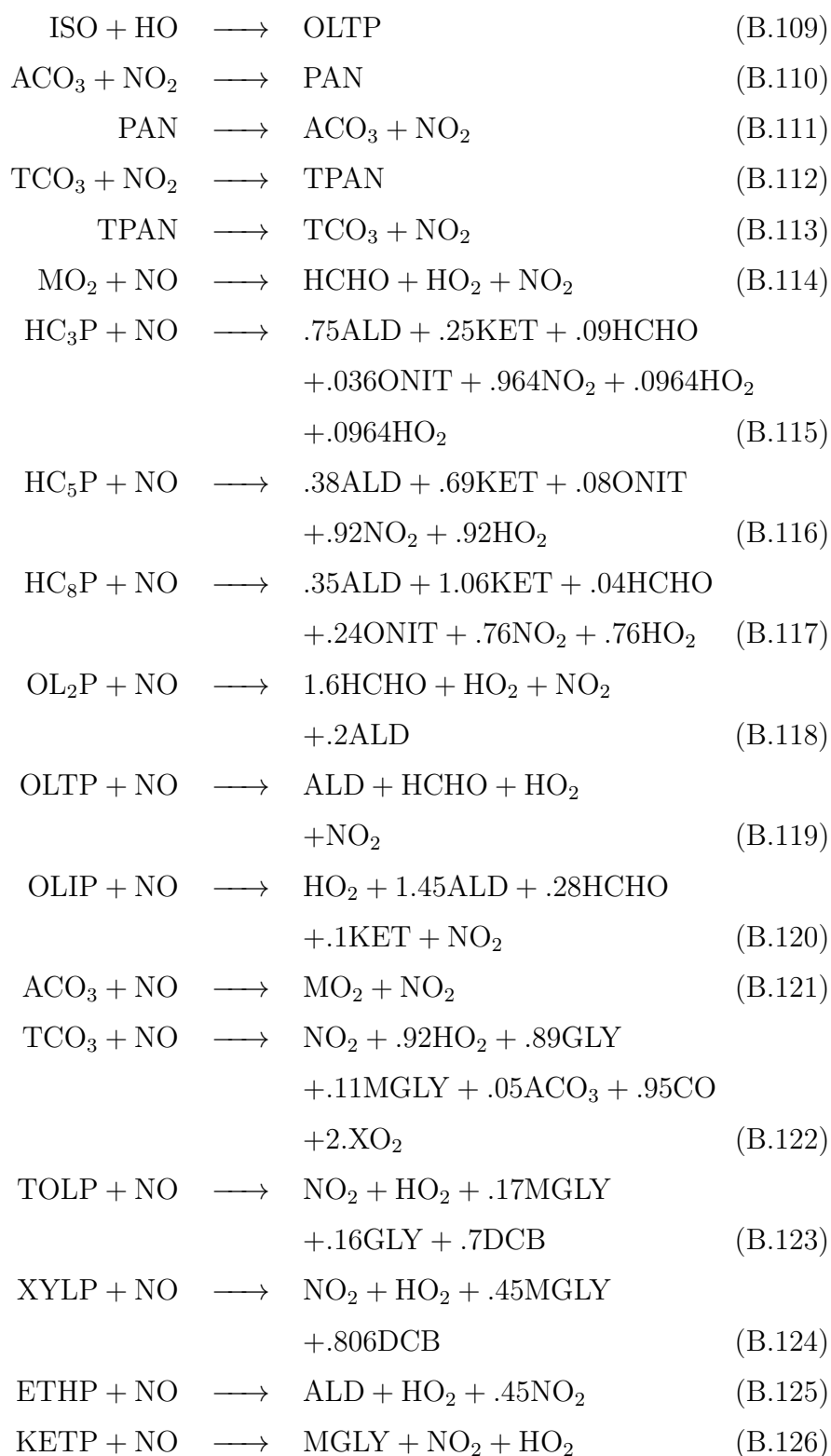
The second and higher order reactions employed in MICTM are reproduced here from Trukenmüller et al. (2004) and Stockwell et al. (1990).



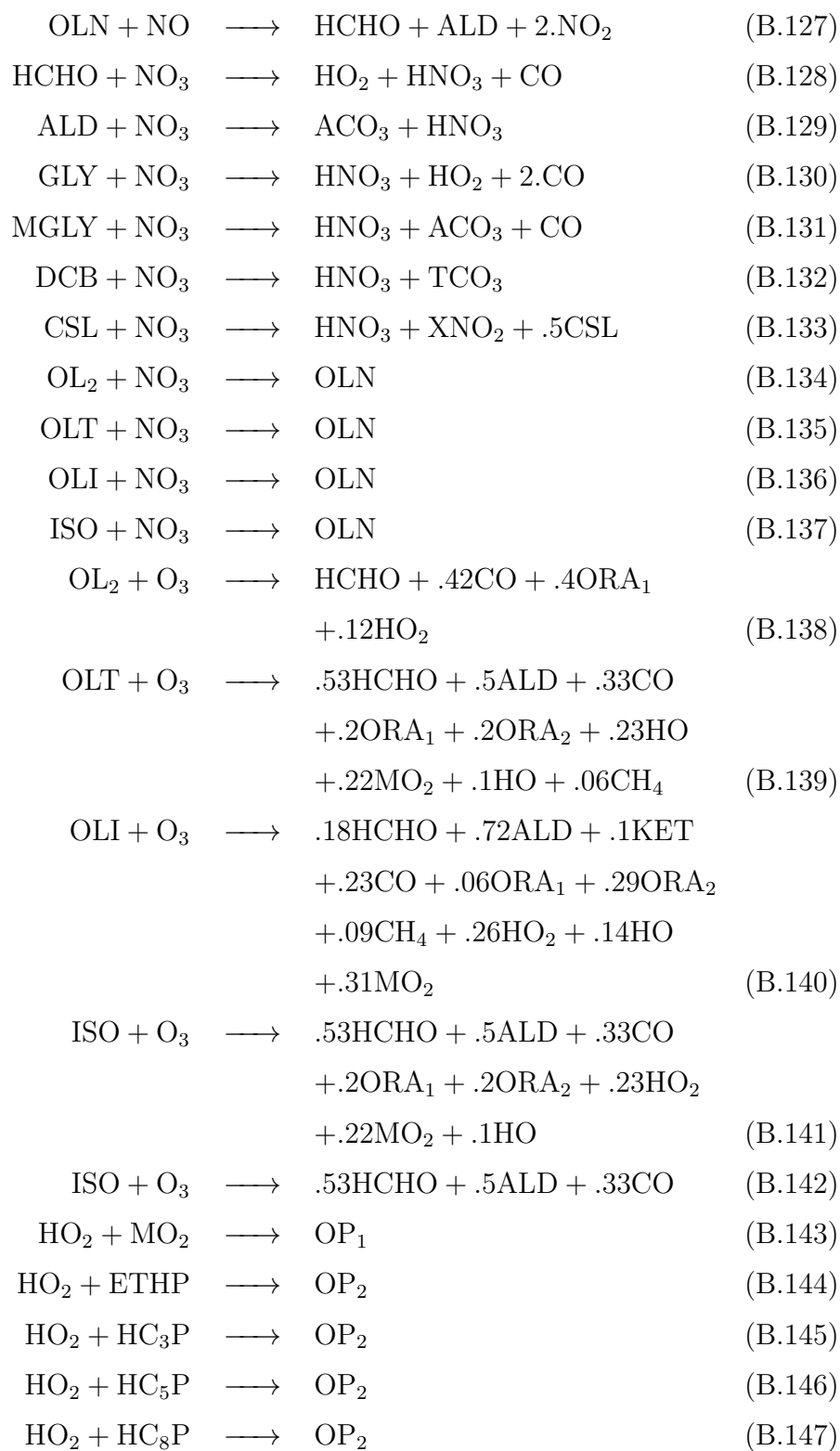
B. CHEMISTRY MECHANISM IN MICTM



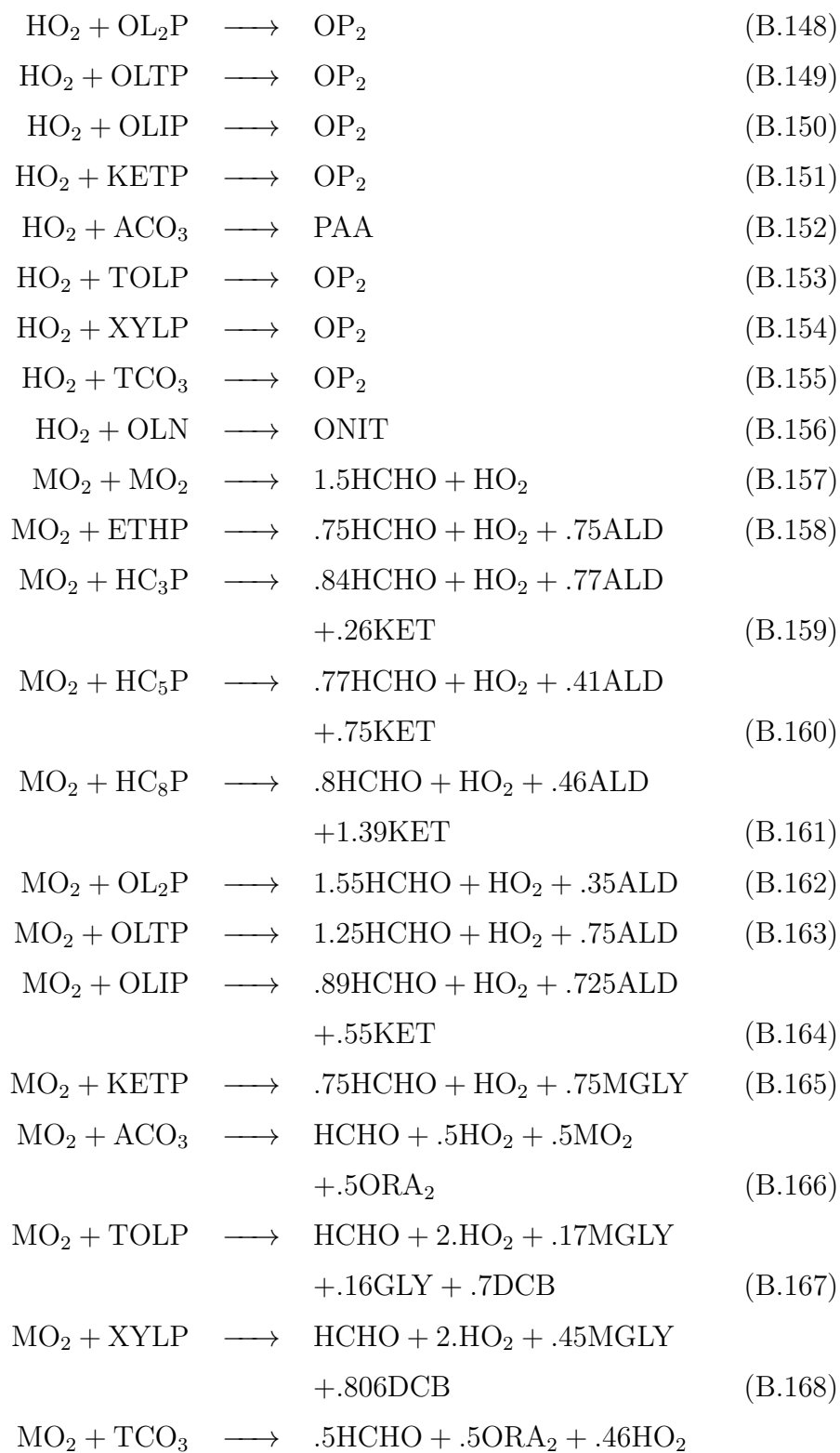
B. CHEMISTRY MECHANISM IN MICTM



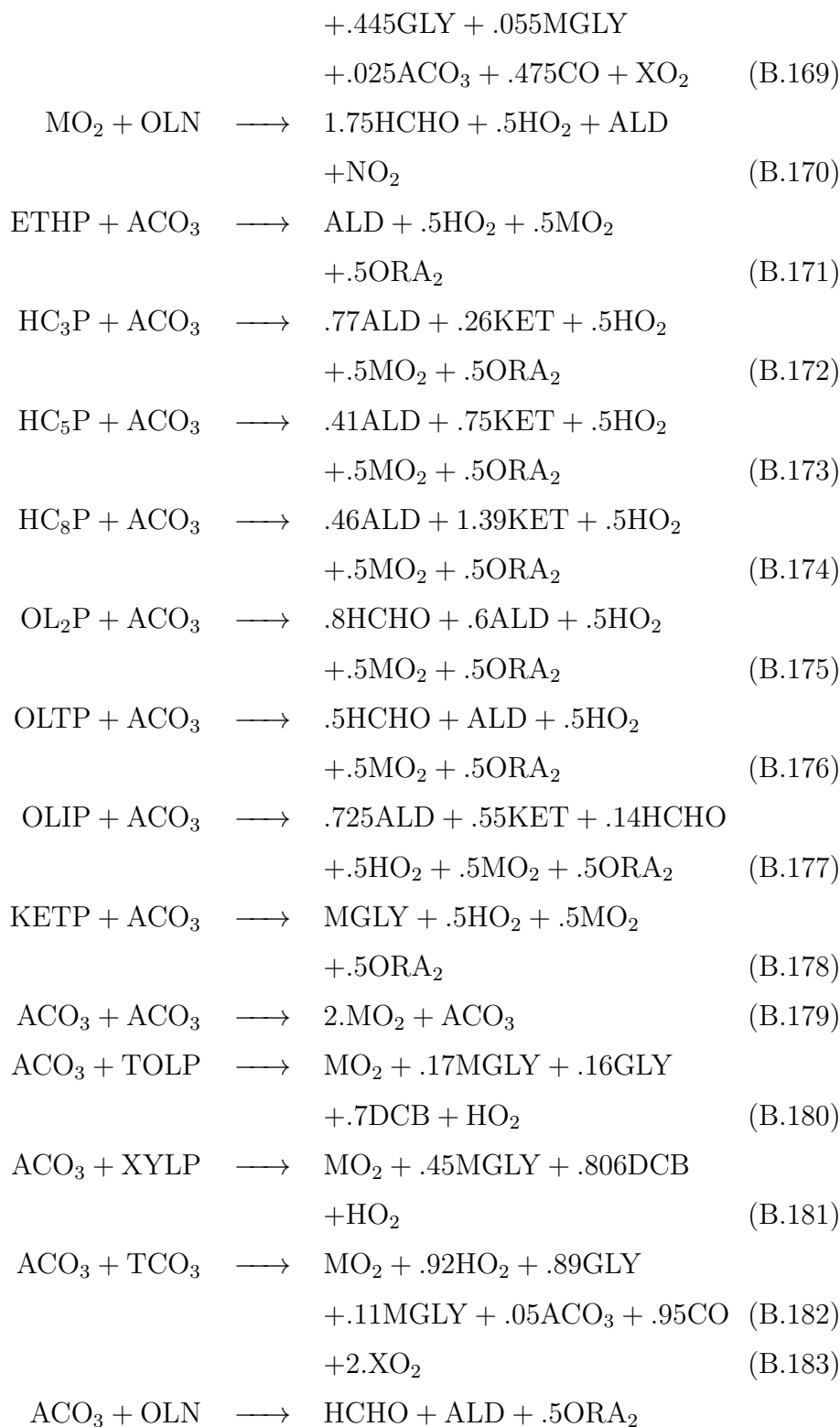
B. CHEMISTRY MECHANISM IN MICTM



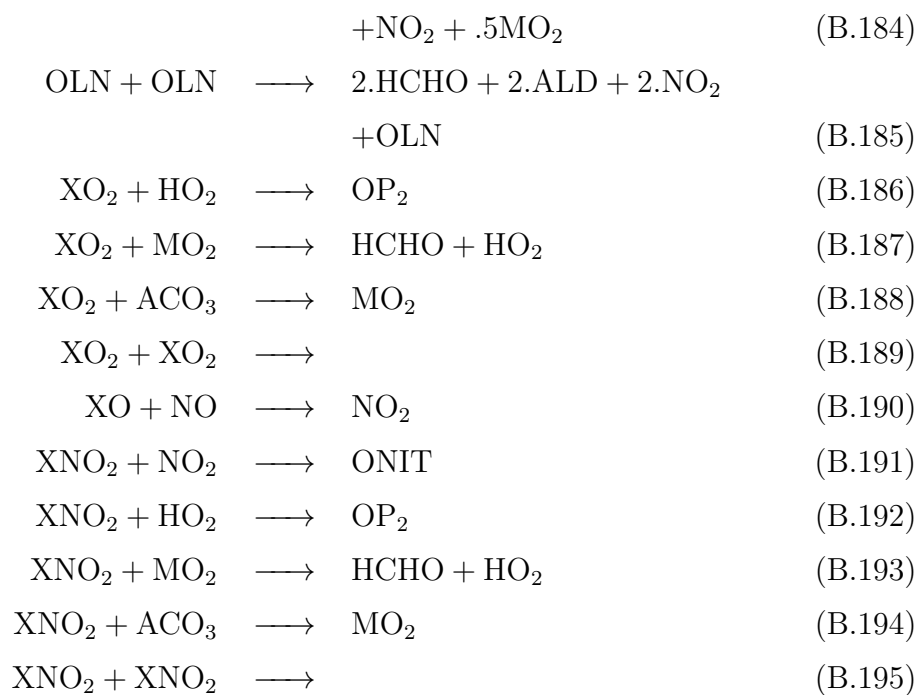
B. CHEMISTRY MECHANISM IN MICTM



B. CHEMISTRY MECHANISM IN MICTM



B. CHEMISTRY MECHANISM IN MICTM



C Split of VOC emissions

The emission data employed in this study included a list of VOC species lumped into one species. In order to be used with the chemistry mechanism RADM2 (Appendix B) these emissions need to be distributed into the respective VOC species of RADM2. The fractions of this split are:

RADM2 species	Emission fraction by mass* [%]
Methane	26.17
Ethane	1.67
Propane	0.17
Alkane1	1.40
Alkane2	10.23
Alkane3	2.02
Ethene	12.46
Propene	3.93
1-Alkene	2.36
x-Alkene ($x > 1$)	1.17
Benzene	3.38
Aromatics1	3.14
Aromatics2	3.18
Phenol, Cresol	4.06
Styrol	0.33
Formaldehyde	12.18
Aldehyde $> C1$	7.68
Acetone	1.13
Ethine	3.34
Total	100.00

*Data provided by Kühlwein (2003)

D Peer reviewed publications

1. Salim, M. H., Schlünzen, K. H., Grawe, D., Boettcher, M., Gierisch, A. M. U., Fock, B. H., 2018. The microscale obstacle-resolving meteorological model mitras v2.0: model theory. *Geosci. Model Dev.* 11, 3427–3445.
doi: 10.5194/gmd-11-3427-2018
2. Kolusu, S. R., Schlünzen, K. H., Grawe, D., Seifert, R., 2018. Determination of chloromethane and dichloromethane in a tropical terrestrial mangrove forest in brazil by measurements and modelling. *Atmospheric Environment* 173, 185–197.
doi: 10.1016/j.atmosenv.2017.10.057
3. von Szombathely, M., Albrecht, M., Antanaskovic, D., Augustin, J., Augustin, M., Bechtel, B., Bürk, T., Fischereit, J., Grawe, D., Hoffmann, P., Kaveckis, G., Krefis, A. C., Oßenbrügge, J., Scheffran, J., Schlünzen, K. H., 2017. A conceptual modeling approach to health-related urban well-being. *Urban Science* 1 (2).
doi: 10.3390/urbansci1020017
4. Kolusu, S. R., Schlünzen, K. H., Grawe, D., Seifert, R., 2017. Chloromethane and dichloromethane in the tropical atlantic ocean. *Atmospheric Environment* 150, 417–424.
doi: 10.1016/j.atmosenv.2016.11.037
5. Meroney, R., Ohba, R., Leitl, B., Kondo, H., Grawe, D., Tominaga, Y., 2016. Review of CFD guidelines for dispersion modeling. *Fluids* 1 (2),

D. PEER REVIEWED PUBLICATIONS

14.
doi: 10.3390/fluids1020014
6. Fischereit, J., Schlünzen, K. H., Gierisch, A. M. U., Grawe, D., Petrik, R., 2016. Modelling tidal influence on sea breezes with models of different complexity. *Meteorologische Zeitschrift* 25 (4), 343–355.
doi: 10.1127/metz/2016/0703
7. Hefny Salim, M., Heinke Schlünzen, K., Grawe, D., 2015. Including trees in the numerical simulations of the wind flow in urban areas: Should we care? *Journal of Wind Engineering and Industrial Aerodynamics* 144, 84–95.
doi: 10.1016/j.jweia.2015.05.004
8. Grawe, D., Thompson, H. L., Salmond, J. A., Cai, X.-M., Schlünzen, K. H., 2013b. Modelling the impact of urbanisation on regional climate in the greater london area. *International Journal of Climatology* 33 (10), 2388–2401.
doi: 10.1002/joc.3589
9. Schoetter, R., Grawe, D., Hoffmann, P., Kirschner, P., Grätz, A., Schlünzen, K. H., 2013. Impact of local adaptation measures and regional climate change on perceived temperature. *Meteorologische Zeitschrift* 22 (2), 117–130.
doi: 10.1127/0941-2948/2013/0381
10. Grawe, D., Schlünzen, K. H., Pascheke, F., 2013a. Comparison of results of an obstacle resolving microscale model with wind tunnel data. *Atmospheric Environment* 79, 495–509.
doi: 10.1016/j.atmosenv.2013.06.039
11. Eden, J. M., Widmann, M., Grawe, D., Rast, S., 2012. Skill, correction, and downscaling of gcm-simulated precipitation. *Journal of Climate* 25 (11), 3970–3984.
doi: 10.1175/JCLI-D-11-00254.1
12. Schlünzen, K. H., Grawe, D., Bohnenstengel, S. I., Schlüter, I., Koppmann, R., 2011. Joint modelling of obstacle induced and mesoscale

changes - current limits and challenges. *Journal of Wind Engineering and Industrial Aerodynamics*, 217–225.

doi: 10.1016/j.jweia.2011.01.009

13. Grawe, D., Cai, X.-M., Harrison, R. M., 2007. Large eddy simulation of shading effects on NO₂ and O₃ concentrations within an idealised street canyon. *Atmospheric Environment* 41 (34), 7304–7314.

doi: 10.1016/j.atmosenv.2007.05.015

14. Trukenmüller, A., Grawe, D., Schünzen, K. H., 2004. A model system for the assessment of ambient air quality conforming to EC directives. *Met. Zeitschr.* 13 (5), 387–394.

doi: 10.1127/0941-2948/2004/0013-0387

15. Bohnenstengel, S., Schünzen, K. H., Grawe, D., 2004. Influence of thermal effects on street canyon circulations. *Met. Zeitschr.* 13 (5), 381–386.

doi: 10.1127/0941-2948/2004/0013-0381

D. PEER REVIEWED PUBLICATIONS

References

- Air Quality Expert Group, 2004. Nitrogen dioxide in the United Kingdom. Report prepared by the Air Quality Expert Group for the Department of Environment, Food and Rural Affairs; Scottish; Welch Assembly Government; and Department of the Environment in Northern Ireland.
- Baik, J.-J., Kang, Y.-S., Kim, J.-J., 2007. Modeling reactive pollutant dispersion in an urban street canyon. *Atmospheric Environment* 41 (5), 934–949. doi: 10.1016/j.atmosenv.2006.09.018
- Baker, J., Walker, H. L., Cai, X.-M., 2004. A study of dispersion of reactive pollutants in and above street canyons - A Large Eddy Simulation. *Atmospheric Environment* 38, 6883–6892.
- Barlow, J. F., Belcher, S. E., 2002. A wind tunnel model for quantifying fluxes in the urban boundary layer. *Boundary Layer Met.* 104, 131–150.
- Blocken, B., 2018. Les over rans in building simulation for outdoor and indoor applications: A foregone conclusion? *Building Simulation* 11 (5), 821–870. doi: 10.1007/s12273-018-0459-3
- Bohnenstengel, S., Schlünzen, K. H., Grawe, D., 2004. Influence of thermal effects on street canyon circulations. *Met. Zeitschr.* 13 (5), 381–386. doi: 10.1127/0941-2948/2004/0013-0381
- Britter, R., Schatzmann, M. (Eds.), 2007a. Background and justification document to support the model evaluation guidance and protocol. COST Of-

office, distributed by: University of Hamburg, Meteorological Institute, Centre for Marine and Atmospheric Sciences, Bundesstraße 55, 20146 Hamburg, Germany.

Britter, R., Schatzmann, M. (Eds.), 2007b. Model evaluation guidance and protocol document. COST Office, distributed by: University of Hamburg, Meteorological Institute, Centre for Marine and Atmospheric Sciences, Bundesstraße 55, 20146 Hamburg, Germany.

Cai, X.-M., Cui, Z., Baker, C., Barlow, J., Belcher, S., 2005. Dispersion and transfer of passive scalars in street canyons with different aspect ratios. In: Royal Meteorological Society (Ed.), Royal Meteorological Society Conference, 12–16 September 2005. University of Exeter.

Carslaw, D. C., 2005. Evidence of an increasing NO₂/NO_x emissions ratio from road traffic emissions. *Atmospheric Environment* 39, 4793–4802.

CEDVAL, 2013. Wind tunnel data sets. <http://www.mi.uni-hamburg.de/cedval/>.

CERC, 2018. <http://www.cerc.co.uk/environmental-software/ADMS-Urban-model.html>, last accessed October 2018.

Cui, Z.-Q., Cai, X.-M., Baker, C., 2004. Large eddy simulation of turbulent flow inside a street canyon. *Quart. J. Royal Meteorol. Soc.* 130, 1373–1394.

DEFRA, 2005. Report: Conversion factors between ppb and g m⁻³ and ppm and mgm⁻³. https://uk-air.defra.gov.uk/assets/documents/reports/cat06/0502160851_Conversion_Factors_Between_ppb_and.pdf, last accessed October 2018.

Diegmann, V., Breitenbach, Y., Neunhäuserer, L., Lutz, M., Rauterberg-Wulff, A., Reichenbacher, W., 2014. Spatial representativeness of air quality samples at hot spots. In: VDI-KRdL: Atmospheric Chemistry - NMVOCs, NO_x, O₃, and the EU Thematic Strategy on Air Pollution. Poster Session. 1st VDI-Expert Forum on Atmospheric Chemistry. VDI.

Eden, J. M., Widmann, M., Grawe, D., Rast, S., 2012. Skill, correction, and downscaling of gcm-simulated precipitation. *Journal of Climate* 25 (11), 3970–3984.

doi: 10.1175/JCLI-D-11-00254.1

Eichhorn, J., Kniffka, A., 2010. The numerical flow model MISKAM: State of development and evaluation of basic version. *Met. Zeitschr.* 19 (1), 81–90.

doi: 10.1127/0941-2948/2010/0425

European Communities, 1996. Council directive 96/62/EC of 27 September 1996 on ambient air quality assessment and management. *Official Journal of the European Communities* L (296), 55–63, <https://eur-lex.europa.eu/legal-content/EN/TXT/PDF/?uri=CELEX:31996L0062>, last accessed April 2019.

European Communities, 1999. Council directive 1999/30/EC of 22 April 1999 relating to limit values for sulphur dioxide, nitrogen dioxide and oxides of nitrogen, particulate matter and lead in ambient air. *Official Journal of the European Communities* L (163), 41–60, <http://eur-lex.europa.eu/LexUriServ/LexUriServ.do?uri=OJ:L:1999:163:0041:0060:EN:PDF>, last accessed April 2019.

European Communities, 2000. Directive 2000/69/EC for the European Parliament and of the Council of 16 November 2000 relating to limit values for benzene and carbon monoxide in ambient air. *Official Journal of the European Communities* L (313), 12–21, <https://eur-lex.europa.eu/legal-content/EN/TXT/PDF/?uri=CELEX:32000L0069&from=EN>, last accessed April 2019.

European Communities, 2001. Directive 2001/81/EC of the European Parliament and of the Council on national emission ceilings for certain atmospheric pollutants. *Official Journal of the European Communities* L (309), 22–30, https://eur-lex.europa.eu/legal-content/EN/TXT/PDF/?uri=uriserv:OJ.L_.2001.309.01.0022.01.ENG, last accessed April 2019.

-
- European Environment Agency, 2016. EMEP/EEA air pollutant emission inventory guidebook. No. 21/2016 in EEA Report, ISSN 1977-8449. European Environment Agency, <https://www.eea.europa.eu/publications/emep-eea-guidebook-2016>, last accessed April 2019.
- European Environment Agency, 2015. Air quality in Europe – 2015 report. No. 5/2015 in EEA Report, ISSN 1977-8449. European Environment Agency, <https://www.eea.europa.eu/publications/air-quality-in-europe-2015>, last accessed April 2019.
- European Environment Agency, 2016. National Emission Ceilings Directive. European Environment Agency, <https://www.eea.europa.eu/themes/air/national-emission-ceilings/national-emission-ceilings-directive>, last accessed April 2019.
- European Environment Agency, 2018. Air quality in Europe – 2018 report. No. 12/2018 in EEA Report, ISSN 1977-8449. European Environment Agency, <https://www.eea.europa.eu/publications/air-quality-in-europe-2018>, last accessed April 2019.
- European Environmental Agency, 2019. National Emission Ceilings Directive reporting status 2018. <https://www.eea.europa.eu/themes/air/national-emission-ceilings/national-emission-ceilings-directive>, last accessed April 2019.
- European Union, 2008. Directive 2008/50/EC of the European Parliament and of the Council of 21 May 2008 on ambient air quality and cleaner air for Europe. Official Journal of the European Union L (152), 1–44, <https://eur-lex.europa.eu/legal-content/EN/TXT/PDF/?uri=CELEX:32008L0050>, last accessed: April 2019.
- European Union, 2015. Commission directive (EU) 2015/1480 of 28 August 2015. Official Journal of the European Union L (226), 4–11, <https://eur-lex.europa.eu/legal-content/EN/TXT/PDF/?uri=CELEX:32015L1480>, last accessed April 2019.
- FHH–BUE, 2017. Luftreinhalteplan für Hamburg (2. Fortschreibung). Freie und Hansestadt Hamburg, Behörde für Umwelt und Energie, <https://>

-
- www.hamburg.de/luftreinhalteplanung/9017668/luftreinhalteplan/, last accessed April 2019.
- Finlayson-Pitts, B. J., Pitts, J. N., 2000. Chemistry of the upper and lower atmosphere: Theory, experiments, and applications. Academic Press, San Diego; London.
- Fischereit, J., Schlünzen, K. H., Gierisch, A. M. U., Grawe, D., Petrik, R., 2016. Modelling tidal influence on sea breezes with models of different complexity. *Meteorologische Zeitschrift* 25 (4), 343–355.
doi: 10.1127/metz/2016/0703
- Franke, J., Hellsten, A., Schlünzen, H., Carissimo, B. (Eds.), 2007. Model evaluation guidance and protocol document. COST Office, distributed by: University of Hamburg, Meteorological Institute, Centre for Marine and Atmospheric Sciences, Bundesstraße 55, 20146 Hamburg, Germany.
- Franke, J., Hellsten, A., Schlünzen, K., Carissimo, B., 2011. The COST 732 best practice guideline for CFD simulation of flows in the urban environment - A summary. *Int. Journ. of Env. and Poll* 44, 419–427.
- Franke, J., Sturm, M., Kalmbach, C., 2012. Validation of OpenFOAM 1.6.x with the German VDI guideline for obstacle resolving micro-scale models. *Journal of Wind Engineering and Industrial Aerodynamics* 104-106, 350–359.
doi: 10.1016/j.jweia.2012.02.021
- Grawe, D., Cai, X.-M., Harrison, R. M., 2007. Large eddy simulation of shading effects on NO₂ and O₃ concentrations within an idealised street canyon. *Atmospheric Environment* 41 (34), 7304–7314.
doi: 10.1016/j.atmosenv.2007.05.015
- Grawe, D., Schlünzen, K. H., 2019. Numerical modeling of pollutant dispersion in a complex urban area, in preparation for Atmospheric Environment.
- Grawe, D., Schlünzen, K. H., Pascheke, F., 2013a. Comparison of results of an obstacle resolving microscale model with wind tunnel data. *Atmospheric*

Environment 79, 495–509.

doi: 10.1016/j.atmosenv.2013.06.039

Grawe, D., Thompson, H. L., Salmond, J. A., Cai, X.-M., Schlünzen, K. H., 2013b. Modelling the impact of urbanisation on regional climate in the greater london area. *International Journal of Climatology* 33 (10), 2388–2401.

doi: 10.1002/joc.3589

Grell, G. A., Peckham, S. E., Schmitz, R., McKeen, S. A., Frost, G., Skamarock, W. C., Eder, B., 2005. Fully coupled "online" chemistry in the wrf model. *Atmos. Environ.* 39, 6957–6976.

doi: 10.1016/j.atmosenv.2005.04.027

Gross, A., Stockwell, W. R., 2003. Comparison of the EMEP, RADM2 and RACM Mechanisms. *Journal of Atmospheric Chemistry* 44, 151–170.

doi: 10.1023/A:1022483412112

Hefny Salim, M., Heinke Schlünzen, K., Grawe, D., 2015. Including trees in the numerical simulations of the wind flow in urban areas: Should we care? *Journal of Wind Engineering and Industrial Aerodynamics* 144, 84–95.

doi: 10.1016/j.jweia.2015.05.004

Hertwig, D., Patnaik, G., Leitl, B., 2017. Les validation of urban flow, part i: flow statistics and frequency distributions. *Environmental Fluid Mechanics* 17 (3), 521–550.

doi: 10.1007/s10652-016-9507-7

Hurley, P. J., Physick, W. L., Luhar, A. K., 2005. Tapm: a practical approach to prognostic meteorological and air pollution modelling. *Environmental Modelling and Software* 20 (6), 737–752.

doi: 10.1016/j.envsoft.2004.04.006

Jacobson, M. Z., 2005. *Fundamentals of Atmospheric Modeling*. Cambridge University Press, ISBN 0-521-54865-9.

doi: 10.1017/CB09781139165389

-
- Jenkin, M. E., Saunders, S. M., Pilling, M. J., 1997. The tropospheric degradation of volatile organic compounds: a protocol for mechanism development. *Atmospheric Environment* 31 (1), 81–104.
doi: 10.1016/S1352-2310(96)00105-7
- Jenkin, M. E., Saunders, S. M., Wagner, V., Pilling, M. J., 2003. Protocol for the development of the master chemical mechanism, mcm v3 (part b): tropospheric degradation of aromatic volatile organic compounds. *Atmospheric Chemistry and Physics* 3 (1), 181–193.
doi: 10.5194/acp-3-181-2003
- Karl, M., 2018. Development of the city-scale chemistry transport model citychem-episode and its application to the city of hamburg. *Geoscientific Model Development Discussions*, 1–60.
doi: 10.5194/gmd-2018-8
- Kolusu, S. R., Schlünzen, K. H., Grawe, D., Seifert, R., 2017. Chloromethane and dichloromethane in the tropical atlantic ocean. *Atmospheric Environment* 150, 417–424.
doi: 10.1016/j.atmosenv.2016.11.037
- Kolusu, S. R., Schlünzen, K. H., Grawe, D., Seifert, R., 2018. Determination of chloromethane and dichloromethane in a tropical terrestrial mangrove forest in brazil by measurements and modelling. *Atmospheric Environment* 173, 185–197.
doi: 10.1016/j.atmosenv.2017.10.057
- Kühlwein, J., 2003. Dataset of microscale traffic emissions, personal communication.
- Kühlwein, J., Friedrich, R., 2004. Berechnung hochauflösender Emissionsdaten für einen Ballungsraum und Straßenschluchten (BEBAS). Ph.D. thesis, https://www.umwelt.niedersachsen.de/download/7268/Berechnung_hoch_aufgeloester_Emissionsdaten_fuer_einen_Ballungsraum_und_Strassenschluchten_Aug._2004.pdf, last accessed April 2004.

-
- Lenschow, P., Abraham, H.-J., Kutzner, K., Lutz, M., Preuß, J.-D., Reichenbächer, W., 2001. Some ideas about the sources of PM10. *Atmospheric Environment* 35, Supplement 1, pp. S23–S33.
doi: 10.1016/S1352-2310(01)00122-4
- Lenz, C.-J., Müller, F., Schlünzen, K. H., 2000. The sensitivity of mesoscale chemistry transport model results to boundary values. *Environmental Monitoring and Assessment* 65, 287–298.
- Lopez, S. D., Lüpkes, C., Schlünzen, K. H., 2005. The effects of different k – ε –closures on the results of a micro–scale model for the flow in the obstacle layer. *Met. Zeitschr.* 14, 781–792.
- Maronga, B., Gross, G., Raasch, S., Banzhaf, S., Forkel, R., Heldens, W., Kanani-Sühring, F., Matzarakis, A., Mauder, M., Pavlik, D., Pfafferoth, J., Schubert, S., Seckmeyer, G., Sieker, H., Winderlich, K., 2019. Development of a new urban climate model based on the model PALM? Project overview, planned work, and first achievements. *Meteorologische Zeitschrift*.
doi: 10.1127/metz/2019/0909
- MCM, 2018. <http://mcm.leeds.ac.uk/>, last accessed October 2018.
- Meroney, R., Ohba, R., Leitl, B., Kondo, H., Grawe, D., Tominaga, Y., 2016. Review of CFD guidelines for dispersion modeling. *Fluids* 1 (2), 14.
doi: 10.3390/fluids1020014
- Meroney, R. N., Pavageau, M., Rafailidis, S., Schatzmann, M., 1996. Study of line source characteristics for 2-d physical modelling of pollutant dispersion in street canyons. *Journal of Wind Engineering and Industrial Aerodynamics* 62 (1), 37–56.
doi: 10.1016/S0167-6105(96)00057-8
- Meyer, E. M. I., 2006. Die Bedeutung atmosphärischer Prozesse für den Stickstoffeintrag in Küstengewässer. Ph.D. thesis, <http://ediss.sub.uni-hamburg.de/volltexte/2006/2939/>, last accessed April 2019.

-
- Meyer, E. M. I., Schlünzen, K. H., 2011. The influence of emission changes on ozone concentrations and nitrogen deposition into the southern north sea. *Meteorol. Zeitschr.* 20 (1), 75–84.
doi: 10.1127/0941-2948/2011/0489
- Minkos, A., Dauert, U., Feigenspan, S., Kessinger, S., Nordmann, S., Himpel, T., 2018. Air Quality 2017. Umweltbundesamt, Dessau-Roßlau, <https://www.umweltbundesamt.de/en/publikationen/luftqualitaet-2017>, last accessed April 2019.
- Müller, F., Schlünzen, K. H., Schatzmann, M., 2000. Test of two numerical solvers for chemical reaction mechanisms in a 3D-air quality model. *Environmental Modelling and Software* 15, 639–646.
- Müller, W. J., Heits, B., Schatzmann, M., 2002. A Prototype Station for the Collection of Urban Meteorological Data.
- NLÖ, FZK, July 2004. ValiData. CD-ROM database, Niedersächsisches Landesamt für Ökologie and Forschungszentrum Karlsruhe.
- Oberdörster, G., Sharp, Z., Atudorei, V., Elder, A., Gelein, R., Kreyling, W., Cox, C., 2004. Translocation of Inhaled Ultrafine Particles to the Brain. *Inhalation Toxicology* 16 (6–7), 437–445.
doi: 10.1080/08958370490439597
- Oke, T. R., Mills, G., Christen, A., Voogt, J. A., 2017. *Urban Climates*. Cambridge University Press.
doi: 10.1017/9781139016476
- Panskus, H., 2000. Konzept zur Evaluation hindernisauflösender mikroskaliger Modelle und seine Anwendung auf das Modell MITRAS. Vol. 389 of *Fortschritt-Berichte VDI*. Düsseldorf: VDI-Verlag.
- Pascheke, F., 2013. Systematische Untersuchung von mikroskaligen Strömungs- und Transportprozessen in städtischer Bebauung, personal communication.

-
- Pavageau, M., Schatzmann, M., 1999. Wind tunnel measurements of concentration fluctuations in an urban street canyon. *Atmospheric Environment* 33 (24), 3961–3971.
doi: 10.1016/S1352-2310(99)00138-7
- Pielke, R. A., 2002. *Mesoscale Meteorological Modeling*, 2nd Edition. Academic Press, ISBN 0-12-554766-8.
- Pielke, R. A., Cotton, W. R., Walko, R. L., Tremback, C. J., Lyons, W. A., Grasso, L. D., Nicholls, M. E., Moran, M. D., Wesley, D. A., Lee, T. J., Copeland, J. H., 1992. A comprehensive meteorological model system RAMS. *Meteorol. Atmos. Phys.* 49, 69–91.
- Reich, T., Peschke, J., 2013. Stickstoffdioxidkonzentrationen an belasteten Straßenabschnitten — Vergleich Screeningrechnung mit Passivsammlermessung. Freie und Hansestadt Hamburg, Institut für Hygiene und Umwelt, Berichtsnummer: HU43/800.56-10/02.13, <http://luft.hamburg.de/datenarchiv-und-stationsinfos/6294548/sonderberichte-luftverschmutzung/>, last accessed April 2019.
- Ruggaber, A., July 1994. Modellierung photolytischer prozesse in der troposphäre. Wissenschaftliche Mitteilung 68, Universität München – Meteorologisches Institut, Theresienstr. 37, D-80333 München, Dissertation der Fakultät für Physik der Ludwig-Maximilians-Universität München.
- Ruggaber, A., Dlugi, R., 1994. Modelling radiation quantities and photolysis frequencies in the troposphere. *J. Atmos. Chem.* 18 (2), 171–210.
doi: 10.1007/BF00696813
- Salim, M. H., Schlünzen, K. H., Grawe, D., Boettcher, M., Gierisch, A. M. U., Fock, B. H., 2018. The microscale obstacle-resolving meteorological model mitras v2.0: model theory. *Geosci. Model Dev.* 11, 3427–3445.
doi: 10.5194/gmd-11-3427-2018
- Schatzmann, M., Bächlin, W., Emeis, S., Kühlwein, J., Leitl, B., Müller, W. J., Schäfer, K., Schlünzen, K. H., 2005. Development and validation of tools for the implementation of European air quality policy in Germany (Project VALIUM). *Atmosph. Chem. Phys. Discuss.* 5, 9621–9639.

-
- Schlünzen, K. H., 1990. Numerical studies in the inland penetration of sea breeze fronts at a coastline with tidally flooded mudflats. *Beitr. Phys. Atmosph.* 63, 243–256.
- Schlünzen, K. H., 1996. Validierung hochauflösender Regionalmodelle. Berichte aus dem Zentrum für Meeres- und Klimaforschung, A23, Meteorologisches Institut, Universität Hamburg, 184 pp. http://bis-erdsystem.de/fileadmin/user_upload/bise/Reports/ZMK-A23.pdf.
- Schlünzen, K. H., Grawe, D., Bohnenstengel, S. I., Schlüter, I., Koppmann, R., 2011. Joint modelling of obstacle induced and mesoscale changes - current limits and challenges. *Journal of Wind Engineering and Industrial Aerodynamics*, 217–225.
doi: 10.1016/j.jweia.2011.01.009
- Schlünzen, K. H., Hinneburg, D., Knoth, O., Lambrecht, M., Leitl, B., Lopez, S., Lüpkes, C., Panskus, H., Renner, E., Schatzmann, M., Schoenemeyer, T., Trepte, S., Wolke, R., 2003a. Flow and transport in the obstacle layer — First results of the microscale model MITRAS. *J. Atmos. Chem.* 44, 113–130.
- Schlünzen, K. H., Hinneburg, D., Knoth, O., Lambrecht, M., Leitl, B., López, S., Lüpkes, C., Panskus, H., Renner, E., Schatzmann, M., Schoenemeyer, T., Trepte, S., Wolke, R., 2003b. Flow and Transport in the Obstacle Layer: First Results of the Micro-Scale Model MITRAS. *Journal of Atmospheric Chemistry* 44, 113–130.
doi: 10.1023/A:1022420130032
- Schlünzen, K. H., Meyer, E. M. I., 2007. Impacts of meteorological situations and chemical reactions on daily dry deposition of nitrogen into the southern North Sea. *Atmospheric Environment* 41-2, 289–302.
- Schlüter, I., 2006. Simulation des Transports biogener Emissionen in und über einem Waldbestand mit einem mikroskaligen Modellsystem. Ph.D. thesis, Dept. Geowissenschaften, Univ. Hamburg.

-
- Schoetter, R., Grawe, D., Hoffmann, P., Kirschner, P., Grätz, A., Schlünzen, K. H., 2013. Impact of local adaptation measures and regional climate change on perceived temperature. *Meteorologische Zeitschrift* 22 (2), 117–130.
doi: 10.1127/0941-2948/2013/0381
- Seinfeld, J. H., 1986. *Atmospheric Chemistry and Physics of Air Pollution*. John Wiley and Sons, ISBN 0-471-82857-2.
- Simpson, D., Olendrzynski, K., Semb, A., Stren, E., Unger, S., 1997. Photochemical Oxidant Modelling in Europe: Multi-Annual Modelling and Source-Receptor Relationships. No. 3/97 in EMEP MSCW Report. Norwegian Meteorological Institute, Oslo, Norway, https://emep.int/publ/reports/1997/EMEP_1997_R3.pdf, last accessed April 2019.
- Sini, J.-F., Anquetin, S., Mestayer, P. G., 1996. Pollutant dispersion and thermal effects in urban street canyons. *Atmospheric Environment* 30 (15).
- Stockwell, W. R., Middleton, P., Chang, J. S., Tang, X., 1990. The second generation regional acid deposition model chemical mechanism for regional air quality modeling. *JGR* 95 (D10), 16,343–16,367.
doi: 10.1029/JD095iD10p16343
- Stull, R. B., 1988. *An Introduction to Boundary Layer Meteorology*. Kluwer Academic Publishers, ISBN 978-90-277-2769-5.
doi: 10.1007/978-94-009-3027-8
- Timmers, V. R. J. H., Achten, P. A. J., 2016. Non-exhaust PM emissions from electric vehicles. *Atmospheric Environment* 134, 10–17.
doi: 10.1016/j.atmosenv.2016.03.017
- Tomlin, A. S., Smalley, R. J., Tate, J. E., Barlow, J. F., Belcher, S. E., Arnold, S. J., Dobre, A., Robins, A., 2009. A field study of factors influencing the concentrations of a traffic-related pollutant in the vicinity of a complex urban junction. *Atmospheric Environment* 43 (32), 5027–5037.
doi: 10.1016/j.atmosenv.2009.06.047

-
- Trukenmüller, A., Grawe, D., Schünzen, K. H., 2004. A model system for the assessment of ambient air quality conforming to EC directives. *Met. Zeitschr.* 13 (5), 387–394.
doi: 10.1127/0941-2948/2004/0013-0387
- Umweltbundesamt, 2018a. <https://www.umweltbundesamt.de/daten/luft/stickstoffdioxid-belastung>, https://www.umweltbundesamt.de/sites/default/files/medien/384/bilder/dateien/4_tab_grenzwerte-nox.pdf, last accessed April 2019.
- Umweltbundesamt, 2018b. Emissionshöchstmengen der NEC-Richtlinie; Reduktionsverpflichtungen der neuen NEC-Richtlinie; Emissionen im Jahr 2016. https://www.umweltbundesamt.de/sites/default/files/medien/384/bilder/dateien/3_tab_emissionshoechstmengen_2018-08-15.pdf, last accessed April 2019.
- Umweltbundesamt, 2019. National Trend Tables for the German Atmospheric Emission Reporting. <https://www.umweltbundesamt.de/themen/luft/emissionen-von-luftschadstoffen>, last accessed April 2019.
- Vardoulakis, S., Fisher, B. E. A., Pericleous, K., Gonzales-Flesca, N., 2003. Modelling air quality in street canyons: a review. *Atmospheric Environment* 37, 155–182.
- Vardoulakis, S., Gonzalez-Flesca, N., Fisher, B. E., Pericleous, K., 2005. Spatial variability of air pollution in the vicinity of a permanent monitoring station in central paris. *Atmospheric Environment* 39 (15), 2725–2736, fourth International Conference on Urban Air Quality: Measurement, Modelling and Management, 25–28 March 2003.
doi: 10.1016/j.atmosenv.2004.05.067
- Vardoulakis, S., Valiantis, M., Milner, J., ApSimon, H., 2007. Operational air pollution modelling in the ukstreet canyon applications and challenges. *Atmospheric Environment* 41 (22), 4622–4637.
doi: 10.1016/j.atmosenv.2007.03.039

-
- VDI, 2000. VDI-Richtlinie 3783, Blatt 12, Environmental meteorology — Physikalische Modellierung von Strömungs- und Ausbreitungsvorgängen in der atmosphärischen Grenzschicht. Beuth Verlag.
- VDI, 2005. VDI-Richtlinie 3783, Blatt 9, Environmental meteorology — Prognostic microscale windfield models — Evaluation for flow around buildings and obstacles. Beuth Verlag.
- VDI, 2017a. VDI-Richtlinie 3783, Blatt 19, Environmental meteorology — Reaction mechanism for the determination of the nitrogen dioxide concentration. Beuth Verlag.
- VDI, 2017b. VDI-Richtlinie 3783, Blatt 9, Environmental meteorology — Prognostic microscale windfield models — Evaluation for flow around buildings and obstacles. Beuth Verlag.
- Vogel, B., Vogel, H., Wilms, W., 1996. Program to determine biogenic emission factors depending on land use., personal communication by F. Fiedler, Institut für Meteorologie und Klimaforschung, Universität Karlsruhe, Kernforschungszentrum Karlsruhe.
- von Szombathely, M., Albrecht, M., Antanaskovic, D., Augustin, J., Augustin, M., Bechtel, B., Bürk, T., Fischereit, J., Grawe, D., Hoffmann, P., Kaveckis, G., Krefis, A. C., Oßenbrügge, J., Scheffran, J., Schlünzen, K. H., 2017. A conceptual modeling approach to health-related urban well-being. *Urban Science* 1 (2).
doi: 10.3390/urbansci1020017
- World Air Quality Index, 2018. <http://aqicn.org>, last accessed October 2018.
- World Health Organisation, 2006. WHO Air quality guidelines for particulate matter, ozone, nitrogen dioxide and sulfur dioxide. Global update 2005. Summary of risk assessment. https://apps.who.int/iris/bitstream/handle/10665/69477/WHO_SDE_PHE_OEH_06.02_eng.pdf, last accessed April 2019.

Young, T. R., Boris, J. B., 1977. A numerical technique for solving stiff ordinary differential equations associated with the chemical kinetics of reactive-flow problems. *The Journal of Physical Chemistry* 81 (25), 2424–2427.

doi: 10.1021/j100540a018

Hiermit versichere ich an Eides statt, dass ich die vorliegende Dissertation mit dem Titel: „*High resolution assessment of concentrations in the urban canopy layer*“ selbstständig verfasst und keine anderen als die angegebenen Hilfsmittel — insbesondere keine im Quellenverzeichnis nicht benannten Internet-Quellen — benutzt habe. Alle Stellen, die wörtlich oder sinngemäß aus Veröffentlichungen entnommen wurden, sind als solche kenntlich gemacht. Ich versichere weiterhin, dass ich die Dissertation oder Teile davon vorher weder im In- noch im Ausland in einem anderen Prüfungsverfahren eingereicht habe und die eingereichte schriftliche Fassung der auf dem elektronischen Speichermedium entspricht.

Hamburg, 30. April 2019 _____